



Delineation of Extreme Ridges in High Resolution Satellite-Based Radar Imagery

**Report
R-12-028-941**

**Prepared for:
Beaufort Regional Environmental Assessment**

**Revision 1.0
March, 2012**

Captain Robert A. Bartlett Building
Morrissey Road
St. John's, NL
Canada A1B 3X5

T: (709) 864-8354
F: (709) 864-4706

Info@c-core.ca
www.c-core.ca

Registered to ISO 9001:2008

This page is intentionally left blank

Delineation of Extreme Ridges in High Resolution Satellite- Based Radar Imagery

Prepared for:

Beaufort Regional Environmental
Assessment

Prepared by:

C-CORE

C-CORE Report Number:

R-12-028-941
Revision 1.0
March, 2012



Captain Robert A. Bartlett Building
Morrissey Road
St. John's, NL
Canada A1B 3X5

T: (709) 864-8354
F: (709) 864-4706

Info@c-core.ca
www.c-core.ca

Registered to ISO 9001:2008

The correct citation for this report is:

C-CORE. (2012). *Delineation of Extreme Ridges in High Resolution Satellite-Based Radar Imagery*, C-CORE Report R-12-028-941, Revision 1.0.

Project Team

Tony King
Ryan Phillips
Daryl Burry
Carl Howell
Mark Howell
Pradeep Bobby
Mike Lynch
Des Power
Sue Carter

REVISION HISTORY

VERSION	SVN	NAME	COMPANY	DATE OF CHANGES	COMMENTS
1.0		Tony King Daryl Burry Pradeep Bobby Carl Howell	C-CORE	03/31/12	Draft Submitted for Review

DISTRIBUTION LIST

COMPANY	NAME	NUMBER OF COPIES
Beaufort Regional Environmental Assessment	Dr. Geneviève Carr	1 (pdf)

EXECUTIVE SUMMARY

One of the major engineering challenges in undertaking production developments in northern shallow water offshore regions is the frequent presence of extreme ice features such as ridges which, in addition to posing a hazard to shipping and surface facilities, often have deep keels which can pose a hazard to subsea facilities such as pipelines. The purpose of this project was to correlate the ice regime, as measured by satellite Synthetic Aperture Radar (SAR), with extreme deep-keeled ice features identified using keel draft data collected by DFO's Upward Looking Sonar (ULS) in the Canadian Beaufort.

ULS data collected between 2003 and 2008 were analyzed and 117 ice ridge keels with drafts in excess of 20 m were identified. No data were available for 2009 due to a malfunctioning ADCP unit, and no processed keel data were available for 2010 or later. Envisat and Landsat 5 and Landsat 7 archives were searched for imagery that corresponded with extreme keel events over the ULS. Imagery was identified for 29 of the 117 keel events.

Unfortunately, correlation of keel and satellite data had limited success. This was attributed to several factors. Availability of suitable imagery held in the various archives corresponding both spatially and temporally with ULS data collection provided limited options. The degree of confidence in ULS data correlation decreased with increased distance from ULS locations, especially in imagery acquired in late spring and early summer when break-up is underway. Attempting to correlate data with surface features in mixtures of loose floes and open water leads was difficult to perform with any degree of confidence. While surface features were evident in SAR imagery, they were not clearly identifiable compared to features in optical imagery.

The availability of high-resolution satellite data has increased significantly in the past few years, therefore a comparison when the more recent ULS data (2010 and later) when it becomes available could yield more favorable results. Ideally, high resolution satellite data should be ordered in advance to ensure that data is collected at regular intervals over the ULS site, rather than assuming that high-resolution imagery will be collected at the appropriate place and time. In the ULS data reviewed for this study, 70% of all keels with drafts over 20 m were detected in the period of May to July, therefore a data acquisition program could be implemented in 2012. Combining high-resolution satellite imagery, ULS (or several ULS installations) and a Lidar survey (or surveys) might give a more reasonable basis for comparison. Simultaneous acquisition of satellite based SAR and high resolution imagery would increase confidence in SAR feature identification.

TABLE OF CONTENTS

EXECUTIVE SUMMARY	i
1 INTRODUCTION.....	1
1.1 Background.....	1
1.2 Objectives.....	1
2 LITERATURE REVIEW	2
3 REVIEW OF ULS DATA	6
3.1 Background.....	6
3.2 ULS Data Used for Analysis.....	7
3.3 Keels Identified for Analysis	8
3.4 Sea Ice Drift Correlation	13
4 ANALYSIS OF SATELLITE IMAGERY	19
4.1 Overview.....	19
4.2 Imagery Analysis.....	21
4.2.1 Image Legend.....	22
4.2.2 Keel 9 in Landsat 5	23
4.2.3 Keel 22 and 23 in Landsat 7	26
4.2.4 Keel 30, 31 and 32 in Envisat APP	31
4.2.5 Keel 33 in Envisat APP	41
4.2.6 Keel 42, 43, 44 and 45 in Landsat 7	44
4.2.7 Keel 50 in Landsat 7	50
4.2.8 Keel 59 to 70 in Landsat 7	55
4.2.9 Keel 74 in Envisat	68
4.2.10 Keel 85 in Envisat	72
4.2.11 Keel 88 in Envisat	74
4.2.12 Keel 92 in Envisat APP.....	79
4.2.13 Keel 117 in Envisat	82
4.3 Summary of Analysis	84
5 ADDITIONAL DATA SOURCES CONSIDERED	85
5.1 Satellite Platform Comparison Parameters.....	85
5.1.1 SAR/Electro-Optical (EO).....	85
5.1.2 Tasking	85
5.1.3 Resolution	85
5.1.4 Coverage	86
5.1.5 Revisit.....	86
5.1.6 Bands.....	86

5.1.7	Archive	87
5.1.8	Cost	87
5.2	Comparison between EO and SAR Sensors	92
5.2.1	Imaging Extended Features	93
5.3	Cryosat-2/Landsat Comparison	94
5.4	COSMO-Skymed Comparison	98
5.5	Quickbird	99
6	SEA ICE RIDGE DETECTION USING OPTICAL SATELLITE IMAGERY	101
6.1	Introduction.....	101
6.2	Procedure	101
6.3	Results	105
6.3.1	Ice Ridge Detection Under Ideal Conditions.....	105
6.3.2	Ice Ridge Detection with SLC Error	106
6.3.3	Ice Ridge Detection with Cloud or Cloud Shadow	108
6.3.4	Ice Ridge Detection During Break-Up	110
6.3.5	Results Summary.....	111
7	CONCLUSIONS AND RECOMMENDATIONS.....	113
7.1	Conclusions.....	113
7.2	Recommendations.....	113
8	REFERENCES	114

LIST OF TABLES

Table 1. Summary of ULS data analyzed.....	7
Table 2. Keels > 20 m identified in ULS data.....	9
Table 3. Summary table of imagery used for drift correlations.....	14
Table 4. Ridge keel and imagery summary table.....	19
Table 5. Overview of ENVISAT.....	87
Table 6. Overview of RADARSAT-1.....	88
Table 7. Overview of RADARSAT-2.....	88
Table 8. Overview of TerraSAR-X.....	89
Table 9. Overview of COSMO SkyMed.....	89
Table 10. Overview of MODIS.....	90
Table 11. Overview of Landsat 5 & 7.....	90
Table 12. Overview of SPOT 4 & 5.....	91
Table 13. Overview of WorldView-1/2.....	91
Table 14. Overview of RapidEye.....	92
Table 15. Overview of GeoEye.....	92

LIST OF FIGURES

Figure 1. Idealized first-year ice ridge geometry (Timco et. al, 2000).....	3
Figure 2. Mooring for IPS, left, and ADCP, right (Melling and Riedel, 2004).....	6
Figure 3. ULS data collection sites (inset show location of sites relative to North America).....	8
Figure 4. ULS data sample.....	9
Figure 5. Unique floes detected, outlined and date stamped from subsequent images.....	15
Figure 6. Satellite-derived drift direction (left) and ULS drift direction (right) for June, 2004.....	16
Figure 7. Satellite-derived drift direction (bottom) and ULS drift direction (top) for July, 2004.....	17
Figure 8. Satellite-derived drift direction (bottom) and ULS drift direction (top) for March, 2005.....	18
Figure 9. Typical sea ice chart from the Canadian Ice Service Western Arctic Regional archive.....	21
Figure 10. Legend layout format.....	22
Figure 11. Sea ice draft profile (top), projected drift trajectory (bottom left) and imagery keel location (bottom right) for Keel 9.....	23
Figure 12. Landsat 5 image (acquisition time 20040426_20:28:29) for Keel 9 showing ULS location, projected keel location and open water leads (ice draft < 0.1 m) in blue.....	24
Figure 13. Possible hit for Keel 9.....	25
Figure 14. Possible hit for ULS draft reading > 20 m (shown in red).....	26

Figure 15. Sea ice draft profile (top), projected drift trajectory (bottom left) and imagery keel location (bottom right) for Keel 22 27

Figure 16. Sea ice draft profile (top), projected drift trajectory (bottom left) and imagery keel location (bottom right) for Keel 23 28

Figure 17. Landsat 7 image (acquisition time 20040529_20:29:16) for Keel 22 and Keel 23 29

Figure 18. Possible hit for Keel 23..... 30

Figure 19. Sea ice draft profile (top), projected drift trajectory (bottom left) and imagery keel location (bottom right) for Envisat APP image (acquisition time 20040605_19:11:08) for Keel 30 32

Figure 20. Sea ice draft profile (top), projected drift trajectory (bottom left) and imagery keel location (bottom right) for Envisat APP image (acquisition time 20040605_19:11:08) for Keel 31 33

Figure 21. Sea ice draft profile (top), projected drift trajectory (bottom left) and imagery keel location (bottom right) for Envisat APP image (acquisition time 20040605_19:11:08) for Keel 32 34

Figure 22. Envisat APP image (acquisition time 20040605_19:11:08) for Keel 30, Keel 31 and Keel 32..... 35

Figure 23. Possible hits for keel 30 and 32 36

Figure 24. Sea ice draft profile (top), projected drift trajectory (bottom left) and imagery keel location (bottom right) for Envisat APP image (acquisition time 20040608_19:16:53) for Keel 30 37

Figure 25. Sea ice draft profile (top), projected drift trajectory (bottom left) and imagery keel location (bottom right) for Envisat APP image (acquisition time 20040608_19:16:53) for Keel 31 38

Figure 26. Sea ice draft profile (top), projected drift trajectory (bottom left) and imagery keel location (bottom right) for Envisat APP image (acquisition time 20040608_19:16:53) for Keel 32 39

Figure 27. Envisat APP image (acquisition time 20040608_19:16:53) for Keel 30, Keel 31 and Keel 32..... 40

Figure 28. Proximity of keels 30 – 32 with inferred rubble field 41

Figure 29. Sea ice draft profile (top), projected drift trajectory (bottom left) and imagery keel location (bottom right) for Keel 33 42

Figure 30. Envisat APP image (acquisition time 20040608_19:16:53) for Keel 33..... 43

Figure 31. Possible hit for Keel 33..... 44

Figure 32. Sea ice draft profile (top), projected drift trajectory (bottom left) and imagery keel location (bottom right) for Keel 42 45

Figure 33. Sea ice draft profile (top), projected drift trajectory (bottom left) and imagery keel location (bottom right) for Keel 43 46

Figure 34. Sea ice draft profile (top), projected drift trajectory (bottom left) and imagery keel location (bottom right) for Keel 44 47

Figure 35. Sea ice draft profile (top), projected drift trajectory (bottom left) and imagery keel location (bottom right) for Keel 45 48

Figure 36. Landsat 7 image (acquisition time 20040623_20:22:16) for Keel 42, Keel 43, Keel 44 and Keel 45..... 49

Figure 37. Sea ice draft profile (top), projected drift trajectory (bottom left) and imagery keel location (bottom right) for Keel 50 Landsat 7 image (acquisition time 20040630_20:28:28)..... 50

Figure 38. Landsat 7 image (acquisition time 20040630_20:28:28) for Keel 50..... 51

Figure 39. Sea ice draft profile (top), projected drift trajectory (bottom left) and imagery keel location (bottom right) for Keel 50 Landsat 5 image (acquisition time 20040701_20:15:28)..... 52

Figure 40. Landsat 7 image (acquisition time 20040701_20:15:28) for Keel 50..... 53

Figure 41. Possible hit for keel 50..... 54

Figure 42. Sea ice draft profile (top), projected drift trajectory (bottom left) and imagery keel location (bottom right) for Keel 59 55

Figure 43. Sea ice draft profile (top), projected drift trajectory (bottom left) and imagery keel location (bottom right) for Keel 60 56

Figure 44. Sea ice draft profile (top), projected drift trajectory (bottom left) and imagery keel location (bottom right) for Keel 61 57

Figure 45. Sea ice draft profile (top), projected drift trajectory (bottom left) and imagery keel location (bottom right) for Keel 62 58

Figure 46. Sea ice draft profile (top), projected drift trajectory (bottom left) and imagery keel location (bottom right) for Keel 63 59

Figure 47. Sea ice draft profile (top), projected drift trajectory (bottom left) and imagery keel location (bottom right) for Keel 64 60

Figure 48. Sea ice draft profile (top), projected drift trajectory (bottom left) and imagery keel location (bottom right) for Keel 65 61

Figure 49. Sea ice draft profile (top), projected drift trajectory (bottom left) and imagery keel location (bottom right) for Keel 66 62

Figure 50. Sea ice draft profile (top), projected drift trajectory (bottom left) and imagery keel location (bottom right) for Keel 67 63

Figure 51. Sea ice draft profile (top), projected drift trajectory (bottom left) and imagery keel location (bottom right) for Keel 68 64

Figure 52. Sea ice draft profile (top), projected drift trajectory (bottom left) and imagery keel location (bottom right) for Keel 69 65

Figure 53. Sea ice draft profile (top), projected drift trajectory (bottom left) and imagery keel location (bottom right) for Keel 70 66

Figure 54. Landsat 7 image (acquisition time 20040718_20:16:05) for Keels 59 through 70..... 67

Figure 55. Sea ice draft profile (top), projected drift trajectory (bottom left) and imagery keel location (bottom right) for Keel 74 for Envisat WS image acquisition 20040728_19:44:43 68

Figure 56. Envisat WS image (acquisition time 20040728_19:44:43) for Keel 74..... 69

Figure 57. Sea ice draft profile (top), projected drift trajectory (bottom left) and imagery keel location (bottom right) for Keel 74 for Envisat WS image acquisition 20040729_19:13:57 70

Figure 58. Envisat WS image (acquisition time 20040729_19:13:57) for Keel 74..... 71

Figure 59. Sea ice draft profile (top), projected drift trajectory (bottom left) and imagery keel location (bottom right) for Keel 85 72

Figure 60. Envisat WS image (acquisition time 20050213_06:24:45) for Keel 85..... 73

Figure 61. Possible hit for keel 85 and drafts > 20 m near ULS location 74

Figure 62. Sea ice draft profile (top), projected drift trajectory (bottom left) and imagery keel location (bottom right) for Keel 88 Envisat WS image acquisition 75

Figure 63. Envisat WS image (acquisition time 20050314_19:48:27) for Keel 88..... 76

Figure 64. Sea ice draft profile (top), projected drift trajectory (bottom left) and imagery keel location (bottom right) for Keel 88 Envisat APP image acquisition 20050315_05:42:02 77

Figure 65. Envisat APP image (acquisition time 20050315_05:42:02) for Keel 88..... 78

Figure 66. Sea ice draft profile (top), projected drift trajectory (bottom left) and imagery keel location (bottom right) for Keel 92 79

Figure 67. Envisat APP image (acquisition time 20050511_19:26:17) for Keel 92..... 80

Figure 68. Possible hit for keel 92 81

Figure 69. Sea ice draft profile (top), projected drift trajectory (bottom left) and imagery keel location (bottom right) for Keel 117 82

Figure 70. Envisat WS image (acquisition time 20080420_06:04:16) for Keel 117..... 83

Figure 71. Envisat WS 20050314_19:48:27 (left) and Envisat APP 20050315_05:42:02 (right) illustrating mobility and dynamics of ice sheet 84

Figure 72. RADARSAT-2 U77 3m February 13, 2012 10:25:50 UTC 94

Figure 73. Location of Cryosat-2 data ground tracks..... 96

Figure 74. Cryosat-2 height of surface (HoS) vs Latitude for ground track 20110525T070716 97

Figure 75. Cryosat-2 height of surface (HoS) vs Latitude for ground track 20110523T070942 97

Figure 76. COSMO-Skymed ScanSAR Wide (image acquisition 20100501_14:34:55) showing ridge..... 98

Figure 77. COSMO-Skymed ScanSAR Wide HH (20100501_11:40:42) showing ridge feature, open water leads and rubble field 98

Figure 78. Sample of a Quickbird multispectral (MS) optical image acquisition date 20050525 99

Figure 79. Close-up of sample Quickbird image showing ridge features 100

Figure 80. Sample ridges taken from Landsat-7 20110401 (202147)..... 101

Figure 81. Sample ridge (left), Sobel (middle) and Canny (right) edge detection 102

Figure 82. Sea ice sample (top left) and progressive Canny edge detection results..... 102

Figure 83. Landsat-7 sample sea ice ridge with SLC error (left) and histogram of sea ice intensity 103

Figure 84. Landsat-7 sample sea ice ridge during seasonal sea ice break up (left) and histogram of sea ice and open water intensity	104
Figure 85. Sea ice sample (top left) and progressive percentage threshold detection results.....	105
Figure 86. Ridge detection under ideal conditions using Landsat-7.....	106
Figure 87. Ridge detection under SLC error conditions using Landsat-7.....	107
Figure 88. Sea ice features under cloud free (top right), cloud shadow (middle right) and cloud opacity (bottom right) conditions in Landsat-7 data	108
Figure 89. Ridge detection failure under cloud opacity, seasonal sea ice break up and SLC error conditions using Landsat-7	109
Figure 90. Stationary sea ice ridge in a flow adjacent to landfast sea ice in Landsat-7 2011, April 15 (top left), May 17 (top right), May 24 (bottom left) and May 26 (bottom right)	110
Figure 91. Ridge detection under sea ice break up conditions using Landsat-7	111

1 INTRODUCTION

1.1 BACKGROUND

Over 25% of the world's petroleum reserves are believed to be in arctic regions and other ice frequented environments, and as world energy demand increases the development of oil and gas resources in harsh ice environments is being increasingly considered by industry. The advancement of safe, cost-effective and reliable engineering solutions for exploration and production infrastructure in ice environments is a key requirement for such field developments. One of the major engineering challenges in undertaking production developments in northern shallow water offshore regions is the frequent presence of extreme ice features such as ridges. Ridges are a significant hazard to transportation and the occurrence of such ridges must be accounted for in the design of offshore structures, including surface structures for exploration and production, as well as subsea structures for production and transportation (i.e. subsea wells and pipelines). Large ice ridges can have deep keels which may gouge the sea floor. Therefore, these features have an impact on pipeline design and burial depth due to the potentially deep gouges formed as a result of the keel/seabed interaction and the associated significant sub-gouge soil deformations. The design of open excavations or buried caissons for the protection of wells and associated subsea facilities is likewise affected.

During a PERD sponsored Ice Scour Workshop in February of 2011, a need was identified to correlate the ice regime, as measured by satellite Synthetic Aperture Radar (SAR), with extreme deep-keeled ice features identified using keel draft data collected by DFO's Ice Profiling Sonar (IPS) in the Canadian Beaufort. Satellite SAR is well known in its ability to characterize the ice regime, and in particular, its ability to extract geophysical characteristics of ice. National ice centers, such as the Canadian Ice Service (CIS), routinely use SAR for ice extent and typing to support the development of ice charts. Satellite imagery may be able to be used to map the spatio-temporal frequency of large ice ridges, providing valuable information on the risks associated with extreme ridge occurrence, including the risk to sub-sea assets.

1.2 OBJECTIVES

The objectives of this project were to:

- acquire high resolution Synthetic Aperture Radar (SAR) data from satellite archives, coincident in location with the Ice Profiling Sonar (IPS) maintained and operated in the Canadian Beaufort by the Institute of Ocean Sciences (OSC) DFO;
- analyze the high resolution SAR data for possible ridge like features;
- correlate ridge features to in-situ data on ice keels, as determined by the IPS; and
- from the correlation, develop a methodology to routinely analyze high resolution SAR data for the extraction of extreme ridge features.

2 LITERATURE REVIEW

Large ridges pose significant threats to navigation, subsea infrastructure and resource development in certain areas of the Arctic. Ridges are one type of deformation that is present. Other deformed ice includes rubble fields, rafting and refrozen leads. Rafting typically occurs with thinner ice types and occurs when one piece of ice rides on top of another due to environmental forces. Since rafting occurs early in the ice season and with thinner ice types it is not a major hazard. Leads, caused for example by an icebreaker, can refreeze and are the weakest form of deformed ice. Rubble fields are piles of broken ice that are caused by discontinuities in the sea bed or by ice motion against an immobile object. Underwater berms, land masses and even some infrastructure remain in the same place from year to year and rubble fields may consistently form in those areas each year (Barker et al., 2008).

Unlike rubble fields which do not have an underlying structure, ridges tend to have a triangular cross-sectional shape (Johansson, 1989), with slightly different shapes for first year (FY) and multi year (MY) ridges. Ridge width is typically greater than sail height. The ratio of these quantities has been measured as approximately 3.2 for MY ridges and 4.4 for FY ridges. Relationships have also been derived between keel depth and sail height and the ratios are 3.1 to 3.3 for MY ridges (but as high as 5.6) and 4.5 to 5.5 for FY ridges (see Figure 1). The ridge and keel heights are dependent on the ice and sea water relative densities, sail and keel widths and porosity. The largest ridge observed was in the Beaufort Sea with a height of 12.8m (Melling et al., 2003). Weathering may cause MY ridges to be shorter than FY ridges (Dierking and Dall, 2007). In some areas ridged and rubble ice can consist of up to 30% of the total ice surface and 50% of the total ice mass and ridges can be found at a frequency of 20 per km (Hudier and Larouche, 2005).

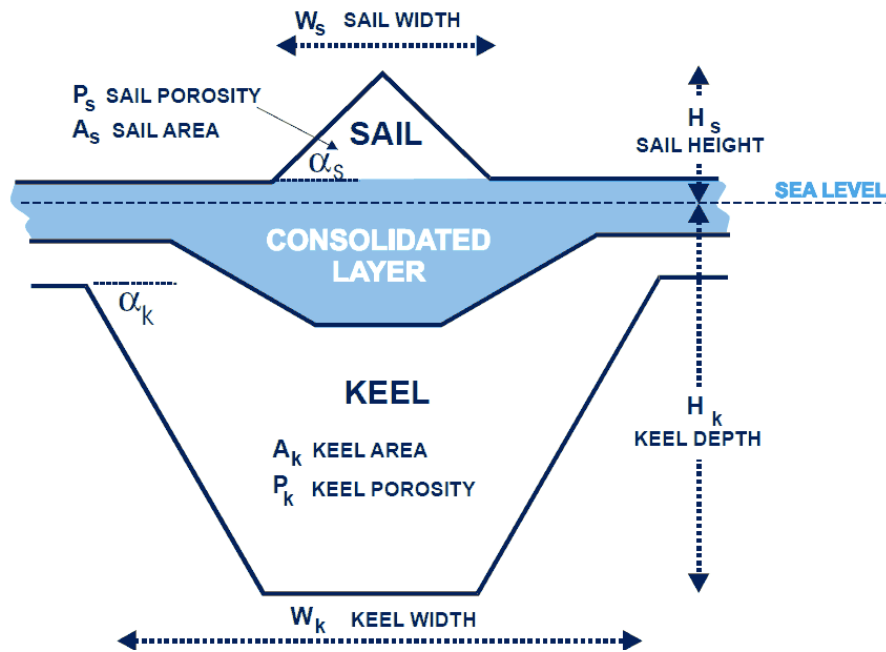


Figure 1. Idealized first-year ice ridge geometry (Timco et. al, 2000)

For decades upward looking sonar (ULS), or ice profiling sonar (IPS) have been used to monitor ice in the Beaufort Sea and for the last 20 years satellite imagery has been used to report on surface ice conditions. Many studies have focused on synthetic aperture radar (SAR) data because it can operate in all weather conditions, see through clouds and at night, but optical data is also used due to its ease of interpretation. SAR data is sensitive to roughness on the order of the radar wavelength, changes in local incidence angle on the order of the SAR wavelength, inhomogeneities in the ice volume (i.e., cracks and bubbles) and changes in the dielectric constant of ice (Dierking and Dall, 2007).

There is a great deal of flexibility in SAR imagery and the parameter selection can have a major impact on the detectability of features. Possibly the most important parameter is the resolution of the sensor. Ridges appear as bright regions or lines in SAR data. Studies have shown that the resolution must be no more than three to five times greater than the dimensions of the ridge within the resolution cell. For example, a 6 m ridge will completely fill a 25 m cell, but such high ridges are rare making it difficult to detect ridges in medium resolution data (Melling, 1998; Dierking and Dall, 2007). At lower resolutions the bright backscatter intensity from the ridge is averaged with the lower backscatter from the surrounding ice, resulting in a lower overall signature for ridge pixels. Research by Barker et al. (2008) indicated that RS1 Fine mode data with 8m resolution was good at characterizing, but not identifying, ice features of interest. Very high resolution (0.6m) Quickbird data (visual) was excellent, but limitations on cloud cover and daylight made it unreliable for operational use. ScanSAR imagery was useful for detecting rubble fields after land fast had broken up and (Johnston, 2001) confirmed that it was difficult to identify ridges within rubble.

Speckle noise is inherent when imaging incoherent regions such as sea ice and it manifests as a salt and pepper appearance in the image. Speckle makes it challenging to identify small targets, such as ridges, and can be reduced by multi-looking or averaging the image, which unfortunately also reduces the resolution. Speckle is not correlated across data channels and when multiple channels of data are available, target detection performance can be enhanced (Hudier and Larouche, 2005).

There are mixed results regarding the impact of incidence angle. Higher incidence angles are preferred for ridge detection as the freeboard of the ridge allows for good corner reflector scattering and the backscatter due to the surface roughness of the surrounding ice is reduced. Incidence angles in the range of 75° to 85° are preferred, but these shallow angles are only available from aerial platforms, and not satellites (Melling, 1998). Some authors report that detection performance is consistent within the range 0° to 60°, which is achievable with satellites (Reference from Dierking and Dall, 2007; Pearson et al., 1980). However, RS1 Extended High (EH) images with incidence angles in the range of 49° to 60° and 25 m resolution were found to be better than higher resolution, lower incidence angle data at identifying new features (Barker et al., 2008).

Studies have been carried out with multiple SAR acquisition frequencies, but other differences in imaging parameters makes it difficult to make definitive conclusions regarding preferred frequency band. Melling (1998) reported that aerial X-band showed more contrast between ridges and level fast ice than X-band satellite data, but there were differences in incidence angle as well. Comparisons between C- and L-band data (Dierking and Dall, 2007) indicated that L-band data had better contrast between deformed and level ice and tended to image the full extent of deformation, whereas only select parts of the deformation were visible in C-band. The L-band data also had greater contrast for FY ridges in the Baltic Sea (4-7dB) and MY ridges off Svalbard (1-4dB). The data used for this study were fully polarimetric data at 1.5 m resolution collected from aerial SAR and focused on deformation rather than ridges specifically.

Aerial and satellite SAR sensors are capable of collecting data with multiple polarizations. Radar is an electromagnetic wave in which the electric and magnetic fields are perpendicular to each other and the direction propagation. The polarization of a radar wave is the orientation of the electric field and signals can be transmitted and received with multiple polarizations. The typical polarizations are HH, VV, HV and VH, where the first letter refers to the transmit polarization, the second letter refers to the receive polarization (H refers to horizontal and V to vertical). The HV and VH channels occur as a result of depolarization. This process occurs when the target rotates some of the incident energy; thus different polarizations provide additional information on the nature of the target.

It has been noted that VV is brighter than HH for level ice, but there are no appreciable differences for ridges (Melling, 1998), implying that there is better contrast with HH. Once study indicated that cross polarization channels (i.e. HV and VH) have better contrast between

ridges and level ice (Dierking and Dall, 2007). This result can be expected since the HV and VH channels are less sensitive to surface roughness, however, this is not always the case (Dierking and Askne, 1998).

Apart from the imaging parameters, the ridge orientation can play a major role in detection. Ridges that have a rubble-like appearance have no real orientation, but triangular ridges are much easier to image broadside than end on. Ridges imaged broadside appear brighter and narrower and can be 2.5dB brighter. It may not be possible to detect FY ridges when imaged end on (Johansson, 1998).

One of the main ways of detecting ridges is simple thresholding. Since ridges appear as bright lines in SAR imagery, brightness contrast between the ridge and its surroundings is required. However, the brightness and contrast are not indicators of ridge height. One study found a correlation between the number of linear features observed and the average thickness of an area (Melling, 1998). Rather than just looking at the maximum brightness values, examining the brightness distribution can indicate regions in which large ridges and keels are present (Marko et al., 2003). Automated analysis of air photos to detect ridges has been conducted using the processes of image filtering, edge detection and edge linking (Lewis et al., 1994). The number, length and spatial pattern of ridges identified were sensitive to the minimum edge gradient parameter and the minimum ridge size (i.e. minimum number of connected pixels to form a ridge). The results were not good for identifying specific ridges, and a 1:1 correspondence could not be made with manual analysis, but the technique reliably characterized the distribution and direction of ridges in the area. For the Beaufort Sea study area ridges were mainly parallel to the coastline.

The ability to detect deformed ice varies with environmental conditions and time of year. Barker et al. (2008) examined rubble fields and noted that detection is very difficult using SAR in first year ice conditions. Detection was possible using high resolution optical data, but was a very time consuming process. Once the ice is landfast, detection remains challenging since rubble fields may be surrounded by rough ice. If the rubble field location is known from field data or historical knowledge, high resolution SAR or optical data can be used for analysis, but it may not be possible to separate ridges from rubble. It is easier to detect rubble during break up and the open water season, especially if it is grounded. It may be easier to detect ridges during the spring melt period (Hudier and Larouche, 2005) because surface meltwater will result in greater contrast between ridges and the surrounding ice. However, if the temperature drops overnight, ice may reform making detection more challenging. When this occurs, SAR images collected later in the afternoon are preferable to images early in the morning.

Overall it is very challenging to detect ridges and extreme ridges in satellite imagery as they do not have a unique signature (Melling, 1998). Further research with dedicated field validation and using high resolution and multi-polarized data would be expected to yield improved results.

3 REVIEW OF ULS DATA

3.1 BACKGROUND

Pack ice draft and motion is based on upward-looking sonar (UPS). Range to the ice-water interface is precisely measured using ice-profiling sonar (IPS), shown in Figure 2 (left), developed at the Institute of Ocean Sciences (Melling et al., 1992). Relying on the motion of the ice to bring new targets into view, the IPS records a range every 1-10 seconds, approximately 2000 km of transect each year, to an accuracy of ± 1 cm (Melling et al., 2005). The final draft of the overhead ice is calculated to within an accuracy of ± 10 cm as the difference between the echo range and the depth of submergence derived by pressure (Melling et al., 2005). Ice velocity is recorded using a bottom-tracking feature of an RD Instruments Acoustic Doppler Current Profiler (ADCP), shown in Figure 2 (right), to a nominal accuracy of ± 0.7 cm/s. Integration of these data over time yields an ice displacement curve that enables the draft data to be mapped to a pseudo-spatial coordinates (Melling and Riedel, 2004).

These instruments are deployed and retrieved the following year, typically in September when pack ice conditions are less severe. Data collection in the Canadian Beaufort Sea at the Site 1 (nominally 70°20'N, 133°44'W), where the majority of the data used in this project was derived, has been on-going since 1991.

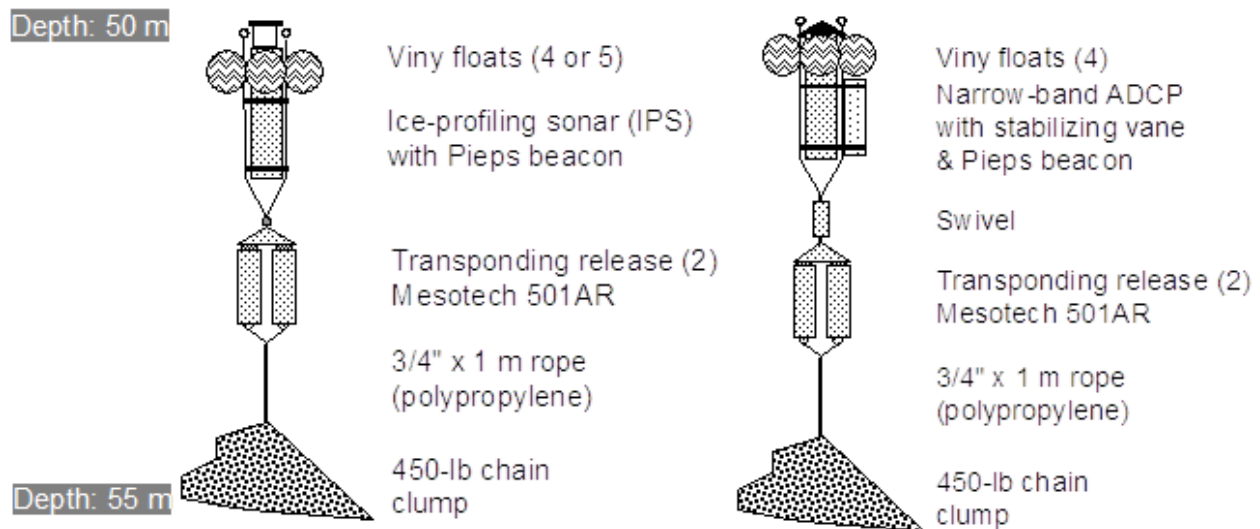


Figure 2. Mooring for IPS, left, and ADCP, right (Melling and Riedel, 2004)

3.2 ULS DATA USED FOR ANALYSIS

While ULS data are available in the Canadian Beaufort back to 1991, the availability of satellite data limited the time period over which the ULS/satellite comparison could be performed. Data were analyzed for two sites, as indicated in Figure 3. Table 1 summarizes the available data at the sites for each year, and the total kilometers of ULS data available (including ice and open water). No data were available for 2009 due to a malfunctioning ADCP and processed data were not available for 2010 or beyond.

Table 1. Summary of ULS data analyzed

Year	Sites	Latitude (°N)	Longitude (°W)	Deployment	Retrieval
2003 - 2004	3	71° 2.25'	133° 24.18'	Sept. 17, 2003	Sept. 30, 2004
		70° 19.94'	133° 44.27'	Sept. 16, 2003	October 1, 2004
		72° 34.68'	127° 27.17'	Sept. 3, 2003	Sept. 26, 2005*
2004 - 2005	1	70° 19.94'	133° 44.29'	Oct. 1, 2004	Sept. 27, 2005
2005 - 2007	2	70° 59.20'	133° 44.86'	Sept. 27, 2005	Sept. 25, 2007
		70° 19.98'	133° 44.48'	Sept. 28, 2005	Sept. 26, 2007
2007 - 2008	1	70° 19.98	133° 44.48'	Sept. 28, 2007	Oct. 4, 2008

*last data collected November 28, 2004

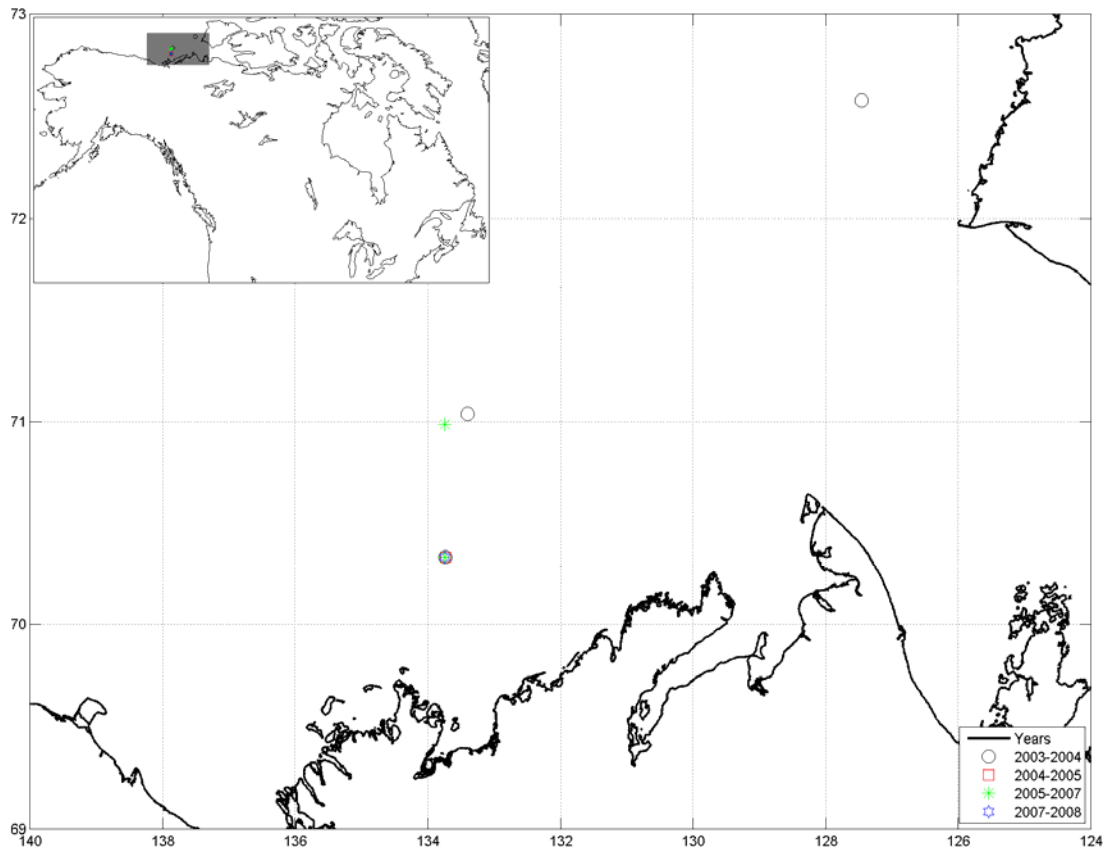


Figure 3. ULS data collection sites (inset show location of sites relative to North America)

3.3 KEELS IDENTIFIED FOR ANALYSIS

The ULS data was provided in a pseudo-spatial format, whereby the IPS and ADCP data were processed to give ice drafts spaced on one meter intervals along the ULS transect. The ULS is a point measurement and gives no indication of the orientation of the ridge relative to the ULS transect, whether the measurement point occurs under the deepest part of the keel, or the type of ice (i.e. first year or multiyear)

Inspection of the ULS data identified 117 keels with drafts in excess of 20 m. These are given in Table 2. Figure 4 shows a data sample from the northernmost site, and includes the deepest keel with a measured draft of 32.38 m, recorded on July 10, 2004. 70% of all keels with drafts over 20 m were detected in the period of May to July, but only 6% in the period of August to December. In cases where more than one deep keels occurred in close proximity, the Rayleigh criterion was applied, whereby two keels were considered entities only if the minimum ice draft between them was less than half the draft of the lesser keel (NSIDC, 2011).

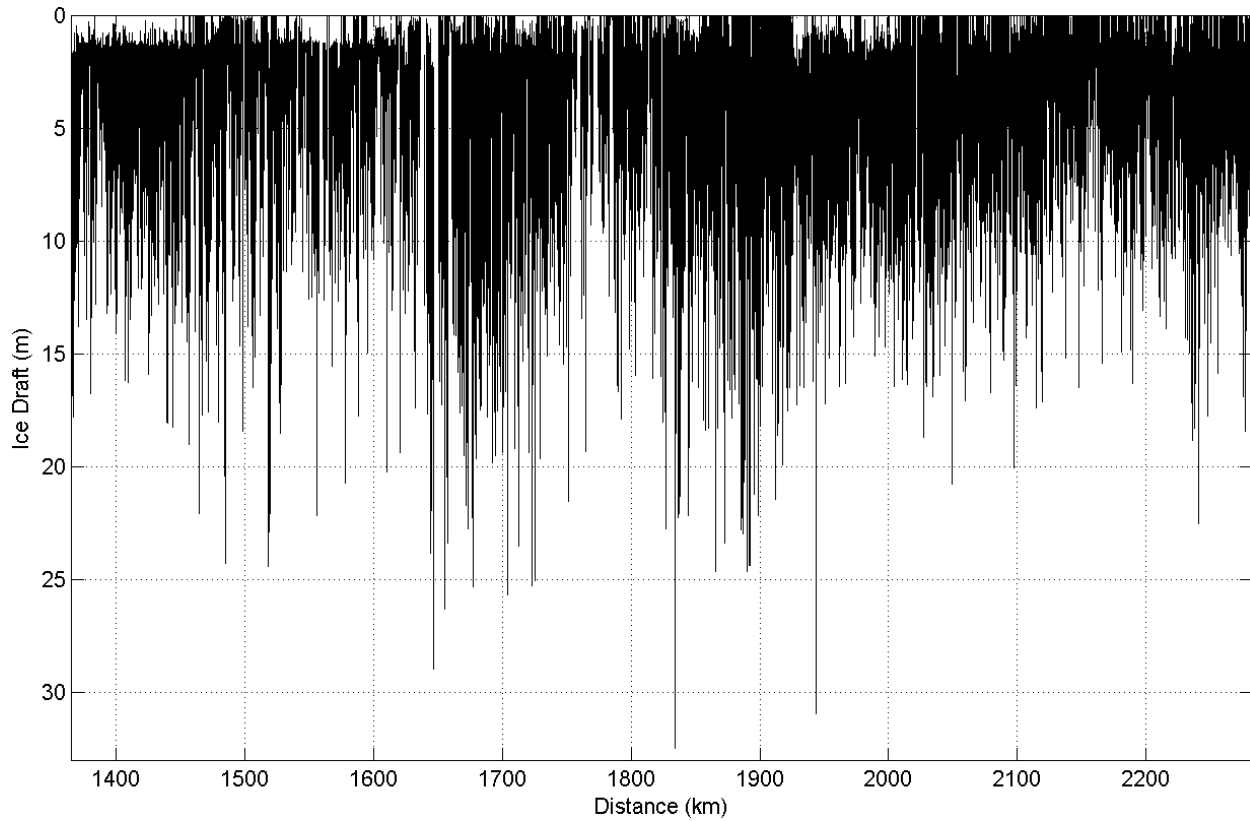


Figure 4. ULS data sample

Table 2. Keels > 20 m identified in ULS data

Keel No.	Draft (m)	ULS Latitude	ULS Longitude	Year	Month	Day	Hour	Minute
1	20.94	71.0375	-133.4030	2004	January	11	4:54	54
2	24.07	71.0375	-133.4030	2004	March	25	22:28	28
3	24.23	71.0375	-133.4030	2004	May	1	3:35	35
4	21.44	71.0375	-133.4030	2004	May	26	5:16	16
5	23.37	71.0375	-133.4030	2004	June	3	1:16	16
6	20.86	70.3323	-133.7379	2004	February	10	15:29	29
7	20.20	70.3323	-133.7379	2004	February	22	21:48	48
8	21.34	70.3323	-133.7379	2004	March	20	19:44	44
9	25.44	70.3323	-133.7379	2004	April	27	8:50	50
10	22.26	70.3323	-133.7379	2004	May	19	8:55	55
11	20.21	70.3323	-133.7379	2004	May	24	20:51	51
12	24.52	70.3323	-133.7379	2004	May	25	2:50	50

13	24.73	70.3323	-133.7379	2004	May	25	3:04	4
14	24.49	70.3323	-133.7379	2004	May	25	3:16	16
15	22.04	70.3323	-133.7379	2004	May	25	3:35	35
16	20.36	70.3323	-133.7379	2004	May	25	3:46	46
17	20.75	70.3323	-133.7379	2004	May	26	4:31	31
18	21.67	70.3323	-133.7379	2004	May	26	5:02	2
19	20.12	70.3323	-133.7379	2004	May	26	15:54	54
20	27.40	70.3323	-133.7379	2004	May	26	16:08	8
21	22.92	70.3323	-133.7379	2004	May	27	18:26	26
22	27.79	70.3323	-133.7379	2004	May	28	4:46	46
23	21.93	70.3323	-133.7379	2004	May	28	18:45	45
24	21.44	72.5780	-127.4529	2003	December	28	3:22	22
25	22.39	72.5780	-127.4529	2004	April	28	21:05	5
26	24.42	72.5780	-127.4529	2004	April	30	20:30	30
27	22.06	72.5780	-127.4529	2004	May	27	16:33	33
28	20.41	72.5780	-127.4529	2004	June	1	04:38	38
29	24.12	72.5780	-127.4529	2004	June	1	08:36	36
30	24.41	72.5780	-127.4529	2004	June	7	03:24	24
31	22.88	72.5780	-127.4529	2004	June	7	04:25	25
32	22.09	72.5780	-127.4529	2004	June	7	10:37	37
33	22.16	72.5780	-127.4529	2004	June	10	06:10	10
34	20.73	72.5780	-127.4529	2004	June	13	21:46	46
35	20.26	72.5780	-127.4529	2004	June	17	12:37	37

Keel No.	Draft (m)	ULS Latitude	ULS Longitude	Year	Month	Day	Hour	Minute
36	23.82	72.5780	-127.4529	2004	June	19	20:13	13
37	21.95	72.5780	-127.4529	2004	June	19	22:51	51
38	28.97	72.5780	-127.4529	2004	June	20	02:07	7
39	26.32	72.5780	-127.4529	2004	June	20	14:07	7
40	20.48	72.5780	-127.4529	2004	June	20	16:08	8
41	23.40	72.5780	-127.4529	2004	June	20	17:19	19

42	21.70	72.5780	-127.4529	2004	June	22	13:14	14
43	22.77	72.5780	-127.4529	2004	June	22	16:37	37
44	22.26	72.5780	-127.4529	2004	June	23	08:06	6
45	25.31	72.5780	-127.4529	2004	June	23	12:22	22
46	25.67	72.5780	-127.4529	2004	June	27	11:03	3
47	23.52	72.5780	-127.4529	2004	June	27	18:16	16
48	25.28	72.5780	-127.4529	2004	June	29	00:20	20
49	25.06	72.5780	-127.4529	2004	June	29	03:50	50
50	21.56	72.5780	-127.4529	2004	July	1	00:27	27
51	22.77	72.5780	-127.4529	2004	July	9	14:51	51
52	32.38	72.5780	-127.4529	2004	July	10	02:14	14
53	22.28	72.5780	-127.4529	2004	July	10	06:08	8
54	22.07	72.5780	-127.4529	2004	July	10	07:36	36
55	21.30	72.5780	-127.4529	2004	July	10	11:48	48
56	22.16	72.5780	-127.4529	2004	July	11	00:41	41
57	24.64	72.5780	-127.4529	2004	July	13	23:54	54
58	23.37	72.5780	-127.4529	2004	July	15	23:14	14
59	22.80	72.5780	-127.4529	2004	July	18	12:00	0
60	23.00	72.5780	-127.4529	2004	July	18	14:51	51
61	22.53	72.5780	-127.4529	2004	July	18	15:46	46
62	20.70	72.5780	-127.4529	2004	July	18	17:30	30
63	20.59	72.5780	-127.4529	2004	July	18	17:42	42
64	24.63	72.5780	-127.4529	2004	July	19	09:52	52
65	24.37	72.5780	-127.4529	2004	July	19	15:29	29
66	21.80	72.5780	-127.4529	2004	July	19	16:03	3
67	20.07	72.5780	-127.4529	2004	July	19	16:43	43
68	24.40	72.5780	-127.4529	2004	July	19	21:10	10
69	23.06	72.5780	-127.4529	2004	July	19	21:29	29
70	21.23	72.5780	-127.4529	2004	July	20	19:38	38
71	20.57	72.5780	-127.4529	2004	July	21	19:50	50

Keel No.	Draft (m)	ULS Latitude	ULS Longitude	Year	Month	Day	Hour	Minute
72	22.18	72.5780	-127.4529	2004	July	21	20:05	5
73	21.46	72.5780	-127.4529	2004	July	23	16:33	33
74	30.95	72.5780	-127.4529	2004	July	29	02:08	8
75	20.78	72.5780	-127.4529	2004	August	9	00:55	55
76	20.07	72.5780	-127.4529	2004	August	14	12:42	42
77	22.55	72.5780	-127.4529	2004	August	26	22:01	1
78	21.50	72.5780	-127.4529	2004	August	26	23:22	22
79	20.33	72.5780	-127.4529	2004	September	21	22:30	30
80	20.34	70.3323	-133.7381	2005	January	22	09:02	2
81	20.59	70.3323	-133.7381	2005	January	23	01:57	57
82	21.68	70.3323	-133.7381	2005	January	23	06:55	55
83	20.57	70.3323	-133.7381	2005	January	26	11:10	10
84	22.06	70.3323	-133.7381	2005	January	29	2:11	11
85	20.70	70.3323	-133.7381	2005	February	12	20:36	36
86	26.76	70.3323	-133.7381	2005	February	13	17:33	33
87	20.14	70.3323	-133.7381	2005	February	15	19:06	6
88	25.17	70.3323	-133.7381	2005	March	15	01:42	42
89	26.06	70.3323	-133.7381	2005	March	20	20:48	48
90	22.88	70.3323	-133.7381	2005	March	20	21:07	7
91	21.80	70.3323	-133.7381	2005	May	7	19:34	34
92	25.89	70.3323	-133.7381	2005	May	13	04:44	44
93	22.47	70.9867	-133.7477	2005	December	7	22:37	37
94	20.29	70.9867	-133.7477	2007	April	1	04:34	34
95	22.69	70.9867	-133.7477	2007	April	23	02:28	28
96	20.38	70.9867	-133.7477	2007	May	9	12:27	27
97	20.10	70.9867	-133.7477	2007	May	28	03:37	37
98	22.43	70.9867	-133.7477	2007	May	28	18:11	11
99	20.03	70.9867	-133.7477	2007	May	28	19:47	47
100	22.51	70.9867	-133.7477	2007	May	28	23:30	30
101	23.20	70.9867	-133.7477	2007	May	28	23:49	49

102	26.58	70.9867	-133.7477	2007	May	29	01:07	7
103	20.79	70.9867	-133.7477	2007	June	5	09:45	45
104	21.42	70.9867	-133.7477	2007	June	8	07:28	28
105	21.37	70.9867	-133.7477	2007	July	1	13:28	28
106	20.36	70.9867	-133.7477	2007	July	22	11:05	5
107	22.86	70.9867	-133.7477	2007	July	22	12:35	35

Keel No.	Draft (m)	ULS Latitude	ULS Longitude	Year	Month	Day	Hour	Minute
108	22.77	70.3329	-133.7414	2006	February	28	11:17	17
109	22.91	70.3329	-133.7414	2006	February	28	23:32	32
110	20.09	70.3329	-133.7414	2006	March	4	02:48	48
111	21.65	70.3329	-133.7414	2006	May	27	00:48	48
112	24.07	70.3329	-133.7414	2006	May	27	02:53	53
113	21.05	70.3329	-133.7414	2006	June	14	19:19	19
114	20.50	70.3329	-133.7414	2007	February	7	16:00	0
115	21.56	70.3329	-133.7414	2007	April	21	17:44	44
116	20.14	70.3329	-133.7414	2007	April	22	13:58	58
117	25.96	70.3329	-133.7414	2008	April	20	15:16	16

3.4 SEA ICE DRIFT CORRELATION

To verify sea ice drift trajectories calculated from the ULS data, a comparison of ice floes from spatially corresponding satellite images was performed. By detecting unique floes from subsequent images, an estimation of drift direction and speed can be determined. Extraction of drift information from overlapping imagery requires that clearly defined, relatively undistorted floes are visible between images. A suitable floe does not need to have unique characteristics, but it must have a well defined boundary so it is identifiable in each image. After a floe was identified, an outline was drawn around it. To assist with ensuring the same floe is found in a subsequent image, the outline was copied and transferred to the second image where it was translated and rotated to fit the same floe. The locations of the two outlines were preserved and a simple script was used to determine the coordinates of the centre of each outline. Although significant rotation of the ice floes was not observed, using the centers of each ice piece ensured that the general current was recorded. This process of detecting and marking floes was continued for the overlapping portion of each image as shown in Figure 5. The imagery used for this exercise are summarized in Table 3. The appropriate segments of the ULS data which corresponded were compared with the floe detection results. Figure 7 through Figure 72 show good correlation for June and July, 2004, and March, 2005, respectively.

Table 3. Summary table of imagery used for drift correlations

Keel Number	Image Type	Image Acquisition Time
30	Envisat APP	20040605_19:11:08
	Envisat APP	20040608_19:16:53
74	Envisat WS	20040728_19:44:43
	Envisat WS	20040729_19:13:57
88	Landsat 7	20050313_20:30:03
	Envisat WS	20050314_19:48:27
	Envisat APP	20050315_05:42:02

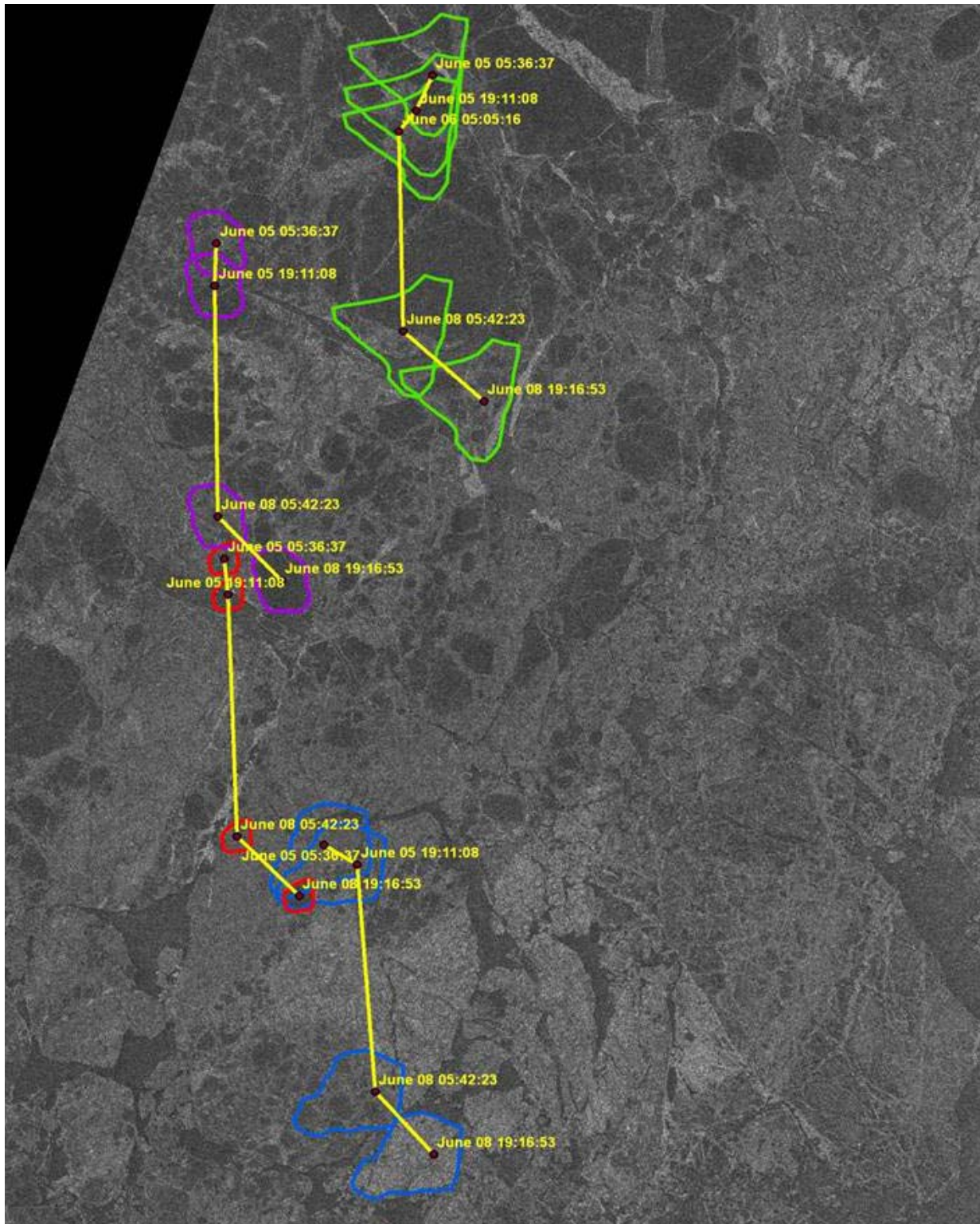


Figure 5. Unique floes detected, outlined and date stamped from subsequent images

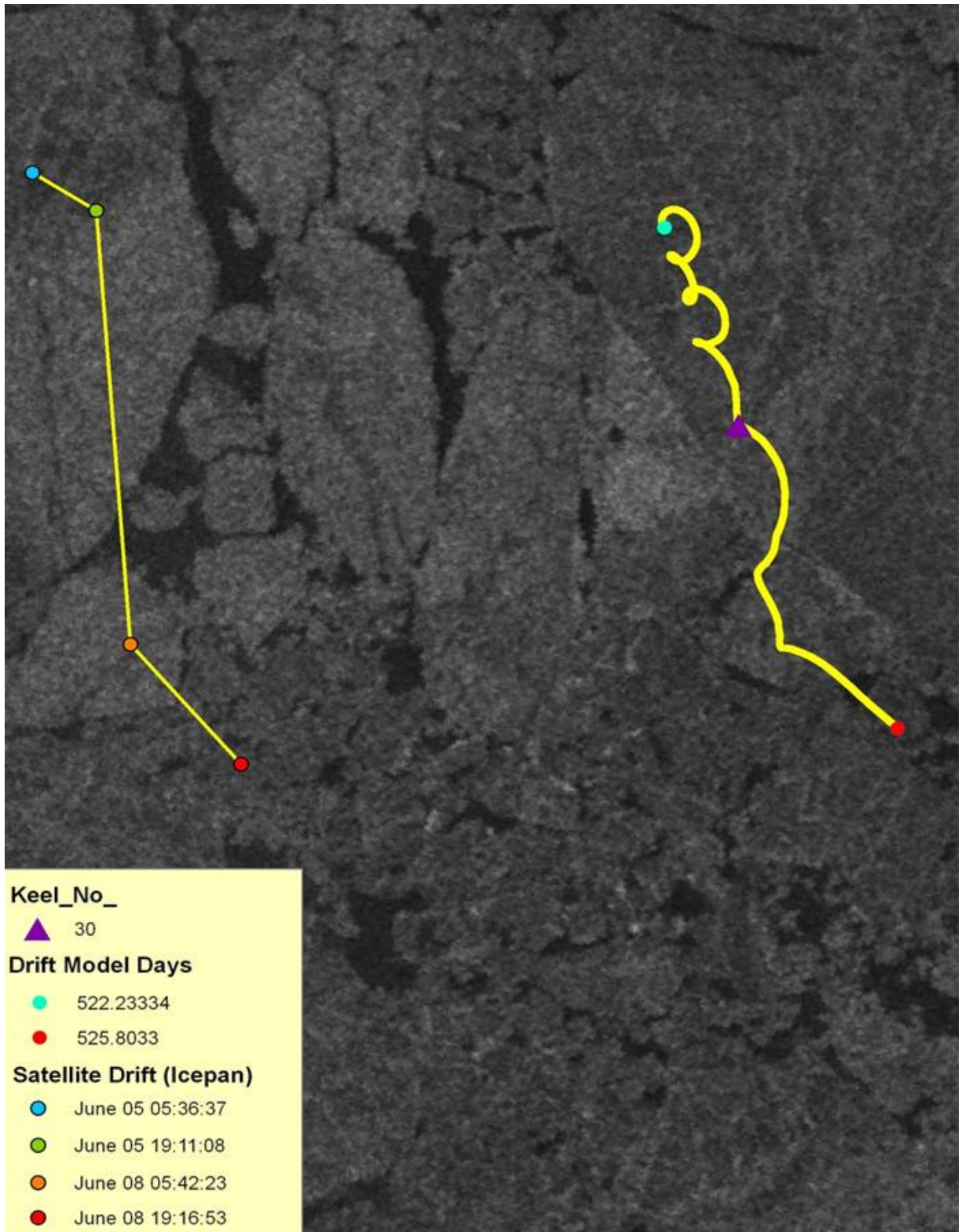


Figure 6. Satellite-derived drift direction (left) and ULS drift direction (right) for June, 2004

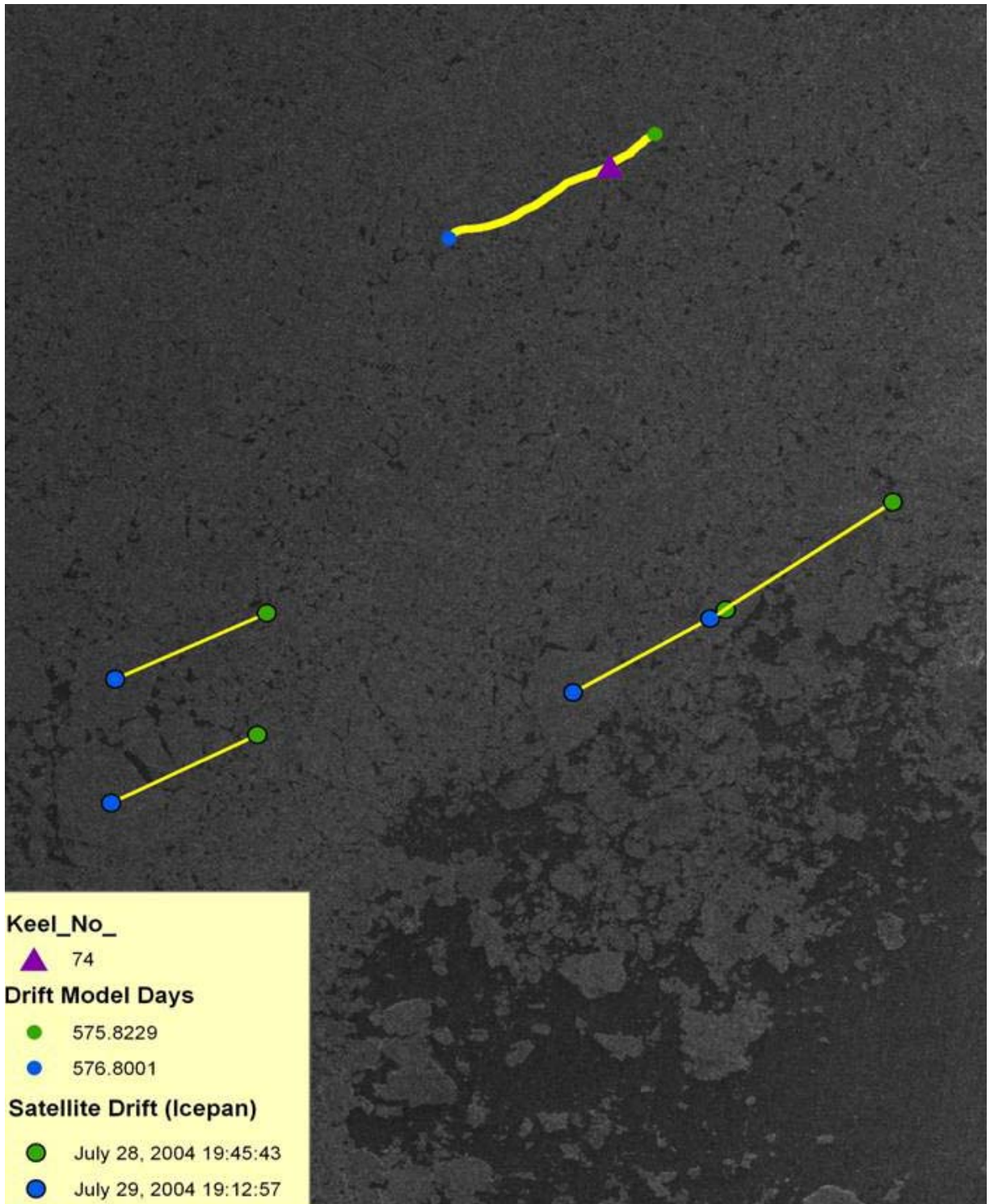


Figure 7. Satellite-derived drift direction (bottom) and ULS drift direction (top) for July, 2004

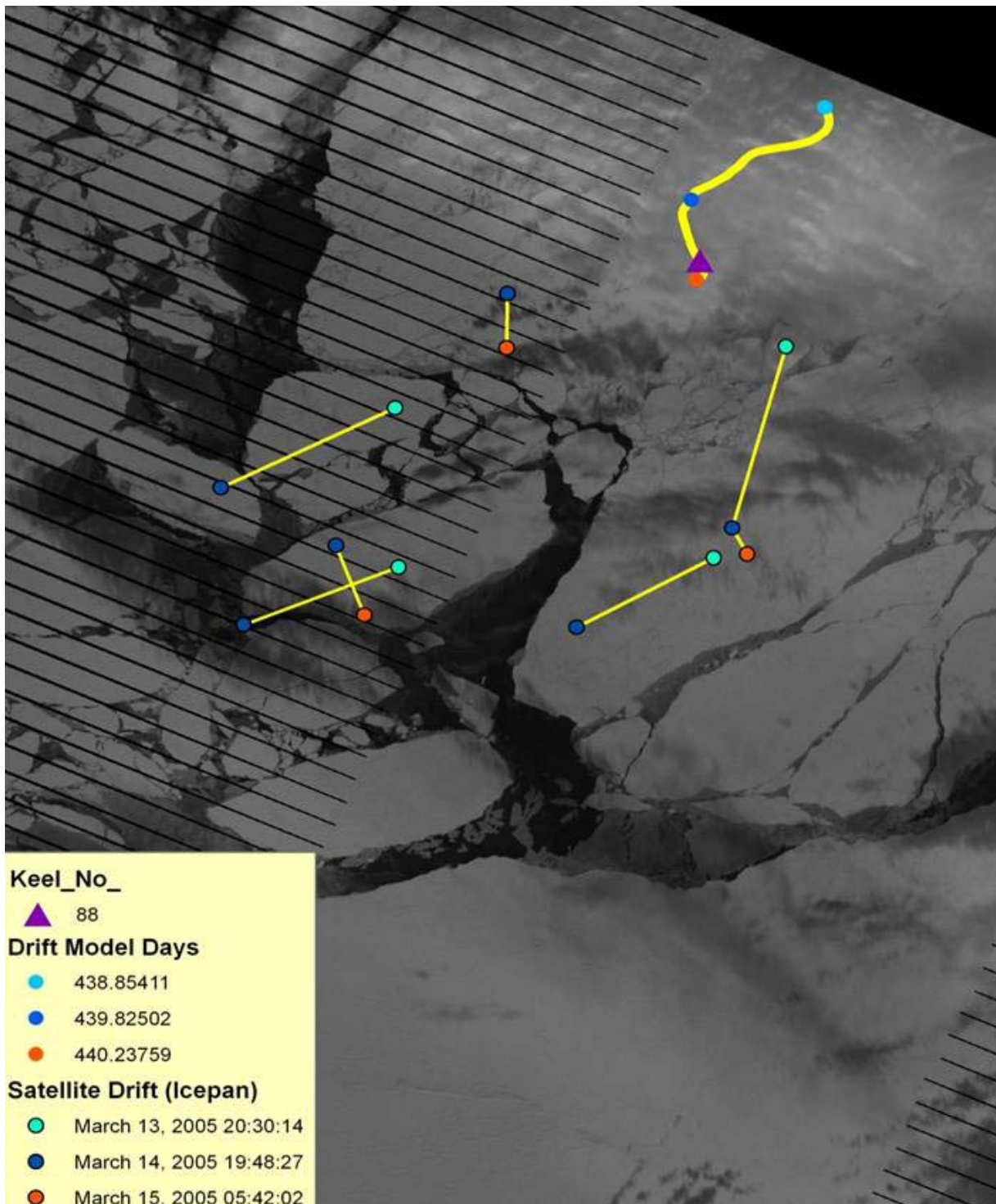


Figure 8. Satellite-derived drift direction (bottom) and ULS drift direction (top) for March, 2005

4 ANALYSIS OF SATELLITE IMAGERY

4.1 OVERVIEW

A total of 117 keels with drafts exceeding 20 m were identified in the ULS data files. Of these, only 29 had suitable satellite imagery corresponding both spatially and temporally with the ULS data. The four imagery platforms utilized in the ULS correlation analysis were Landsat 5 and Landsat 7 from the United States Geological Service (USGS) archive and Envisat Wide Swath (WS) and Envisat Alternative Polarization Precision (APP) from the European Space Agency (ESA) archive. Image type, data resolution and acquisition times are summarized in Table 4.

Other imagery platforms investigated were COSMO-SkyMed ScanSAR Wide (30 m resolution) and high resolution Quickbird (60 - 70 cm resolution). Although there were no ULS data available to attempt correlation of features for these images, a 'visual' assessment was performed to determine their practicality and usefulness in any future work. These data are described in Section 5.

Table 4. Ridge keel and imagery summary table

Keel Number	Keel Draft (m)	ULS Location	Image Type	Image Resolution (m)	Image Acquisition Time (yyyymmdd_hhmmss)
9	25.438	70.3323°N 133.7379°W	Landsat 5	30	20040426_20:28:29
22	27.794	70.3323°N 133.7379°W	Landsat 7	15	20040529_20:29:16
23	21.933	70.3323°N 133.7379°W	Landsat 7	15	20040529_20:29:16
30	24.408	72.5780°N 127.4529°W	Envisat APP Envisat APP	25 25	20040605_19:11:08 20040608_19:16:53
31	22.881	72.5780°N 127.4529°W	Envisat APP Envisat APP	25 25	20040605_19:11:08 20040608_19:16:53
32	22.085	72.5780°N 127.4529°W	Envisat APP Envisat APP	25 25	20040605_19:11:08 20040608_19:16:53
33	22.158	72.5780°N 127.4529°W	Envisat APP	25 25	20040608_19:16:53
42	21.701	72.5780°N 127.4529°W	Landsat 7	15	20040623_20:22:16
43	22.77	72.5780°N 127.4529°W	Landsat 7	15	20040623_20:22:16
44	22.257	72.5780°N 127.4529°W	Landsat 7	15	20040623_20:22:16
45	25.309	72.5780°N 127.4529°W	Landsat 7	15	20040623_20:22:16

Keel Number	Keel Draft (m)	ULS Location	Image Type	Image Resolution (m)	Image Acquisition Time (yyyymmdd_hhmmss)
50	21.558	72.5780°N 127.4529°W	Landsat 5 Landsat 7	30 15	20040701_20:15:28 20040630_20:28:28
59	22.796	72.5780°N 127.4529°W	Landsat 7	15	20040718_20:16:05
60	22.995	72.5780°N 127.4529°W	Landsat 7	15	20040718_20:16:05
61	22.532	72.5780°N 127.4529°W	Landsat 7	15	20040718_20:16:05
62	20.7	72.5780°N 127.4529°W	Landsat 7	15	20040718_20:16:05
63	20.593	72.5780°N 127.4529°W	Landsat 7	15	20040718_20:16:05
64	24.627	72.5780°N 127.4529°W	Landsat 7	15	20040718_20:16:05
65	24.37	72.5780°N 127.4529°W	Landsat 7	15	20040718_20:16:05
66	21.803	72.5780°N 127.4529°W	Landsat 7	15	20040718_20:16:05
67	20.065	72.5780°N 127.4529°W	Landsat 7	15	20040718_20:16:05
68	24.4	72.5780°N 127.4529°W	Landsat 7	15	20040718_20:16:05
69	23.061	72.5780°N 127.4529°W	Landsat 7	15	20040718_20:16:05
70	21.234	72.5780°N 127.4529°W	Landsat 7	15	20040718_20:16:05
74	30.954	72.5780°N 127.4529°W	Envisat WS Envisat WS	150 150	20040728_19:44:43 20040729_19:13:57
85	20.704	70.3323°N 133.7381°W	Envisat WS	150	20050213_06:24:45
88	25.174	70.3323°N 133.7381°W	Envisat WS Envisat APP	150 25	20050314_19:48:27 20050315_05:42:02
92	25.892	70.3323°N 133.7381°W	Envisat APP	25	20050511_19:26:17
117	25.955		Envisat WS	150	20080420_06:04:16

4.2 IMAGERY ANALYSIS

The Canadian Ice Service maintains an online digital archive of historical sea ice charts in gif and E00 format (CIS, 2012). E00 is essentially an interchange data format developed to enable users to move data into and out of ARC/INFO. These files were converted to ARCGIS shapefile format and were used as an aid to identify ice types in applicable imagery. The Western Arctic Regional archive typically produces a monthly chart during the winter months and a bi-weekly chart during the summer. A typical monthly chart is shown in Figure 9.

As illustrated in Figure 11, for each keel and corresponding image, the appropriate ULS header and text file were loaded into Matlab and the resulting sea ice draft profile, projected drift trajectory and location of keel on applicable imagery scene were generated. Figure 12 shows the drift trajectory superimposed on the corresponding satellite image, in this case, a Landsat 5 scene acquired on 20040426_20:28:29.

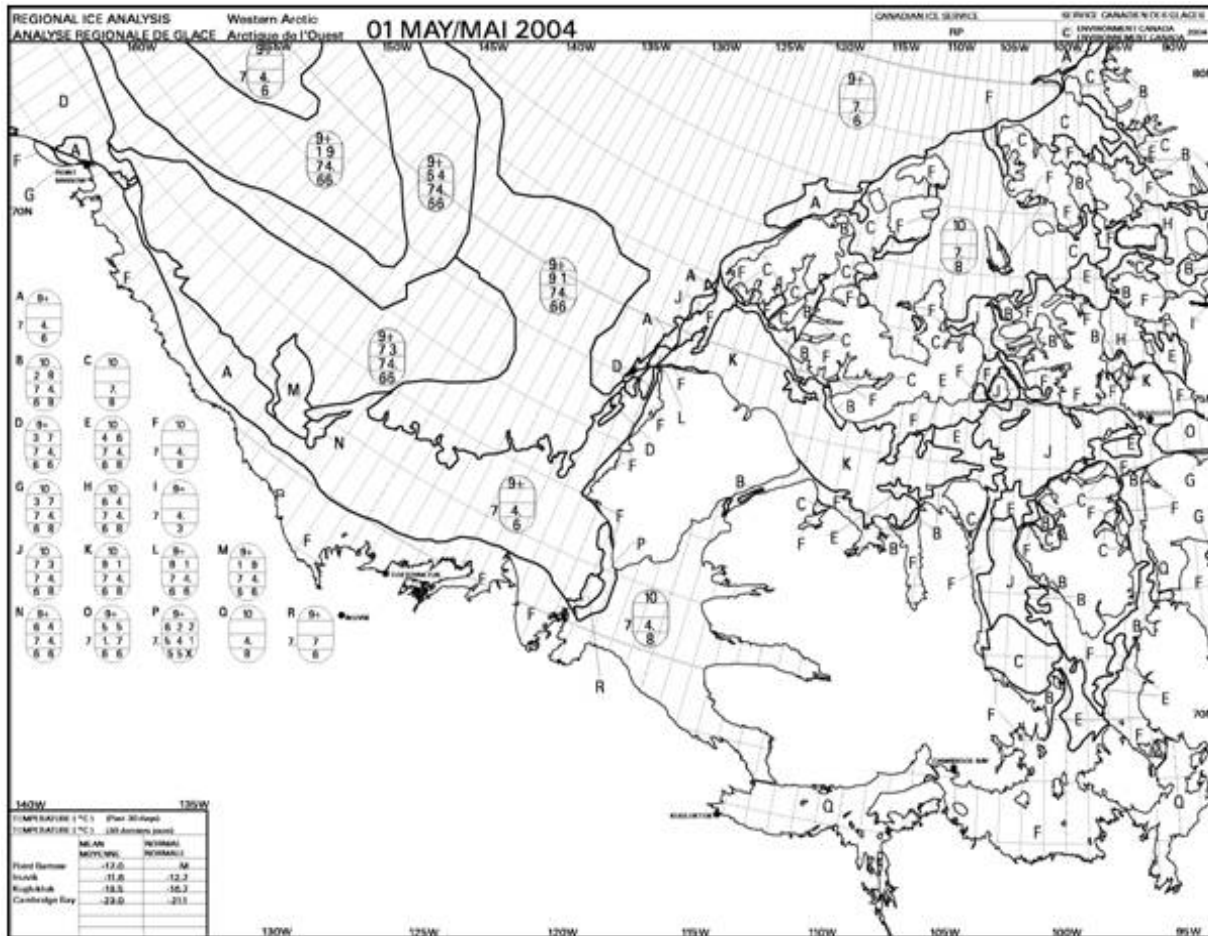


Figure 9. Typical sea ice chart from the Canadian Ice Service Western Arctic Regional archive

4.2.1 Image Legend

The legend, shown in Figure 10, and appearing on figures in this section, is laid out in a format that shows the image acquisition time, ULS location and projected keel position at the time of image acquisition, followed by the time (in brackets) in which the keel passed over the ULS. After the brackets is shown the time difference between image acquisition and when the keel was recorded by the ULS, a plus (+) indicating the keel position is after image acquisition and a minus (-) indicating the keel position is prior to image acquisition. To assist in feature correlation, the drift trajectory is colour coded according to ice draft in intervals of 0.0 to 0.1 m (open water leads), < 10 m, 10 - 15 m and > 20 m. Intermittent breaks in the drift trajectory indicate sections of null data.



Figure 10. Legend layout format

4.2.2 Keel 9 in Landsat 5

ULS data for keel 9 is shown in Figure 11, with draft data collected between keel detection and satellite image acquisition shown in green. Coverage for keel 9 is provided with a Landsat 5 image shown in Figure 13. The CIS classifies sea ice at the site of keel 9 as first-year thick with trace amounts of old ice. Several surface features are evident throughout the image, however, the 30 metre resolution does not allow distinguishing these features with a high degree of confidence. The section of the drift trajectory shown in dark blue (to the extreme right) exhibits a relatively good correlation with an open water lead. The fact that the two leads closer to the keel location were not detected by the ULS suggests that these leads may have recently opened previous to image acquisition. Zooming in on the predicted keel location in Figure 13, shows a feature crossing the drift trajectory just west of the location suggesting a 'possible' hit for keel 9. A loose correlation of surface features to ULS data is displayed throughout the image extent as shown in Figure 14, however, the further afield from the ULS location, the lower the confidence.

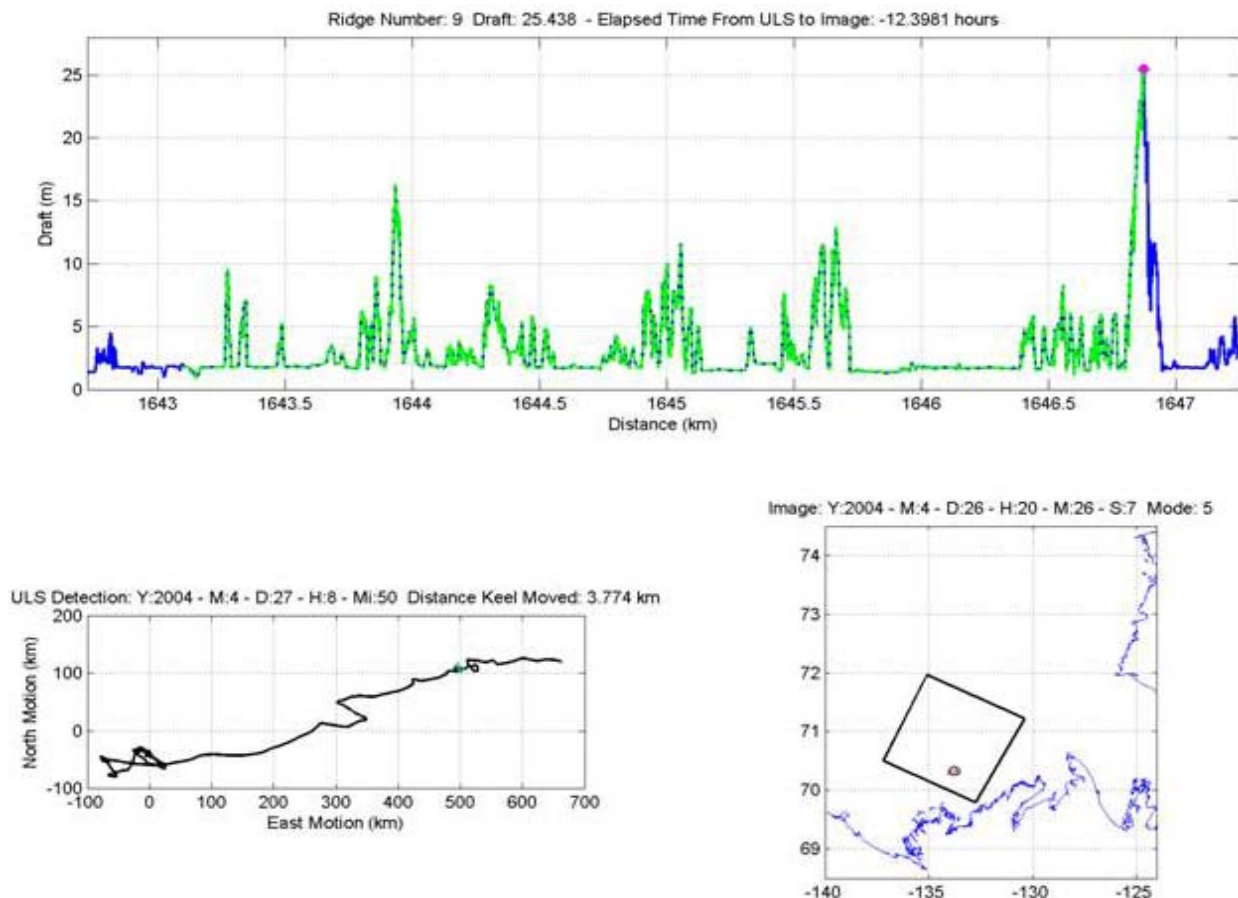


Figure 11. Sea ice draft profile (top), projected drift trajectory (bottom left) and imagery keel location (bottom right) for Keel 9

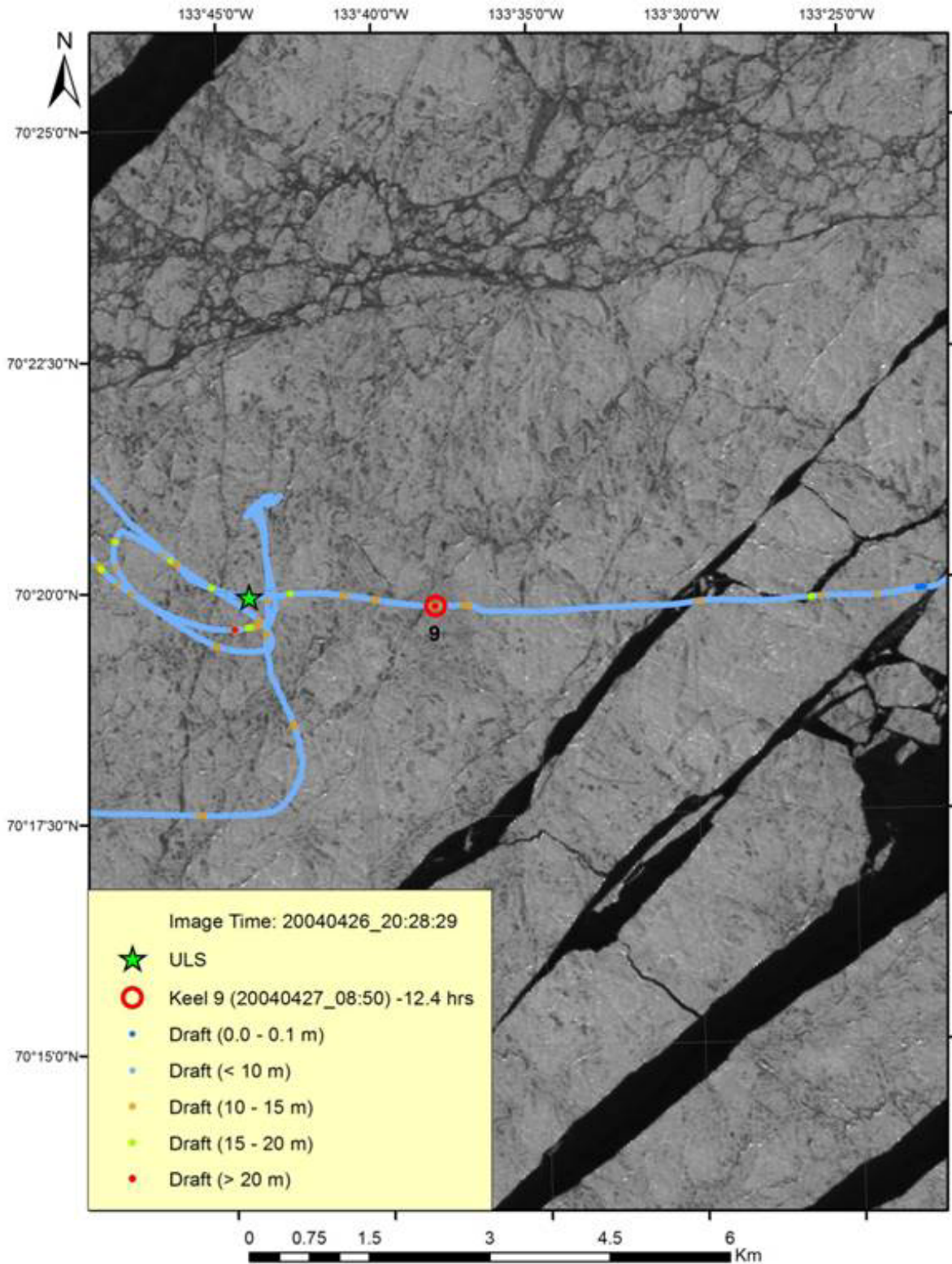


Figure 12. Landsat 5 image (acquisition time 20040426_20:28:29) for Keel 9 showing ULS location, projected keel location and open water leads (ice draft < 0.1 m) in blue

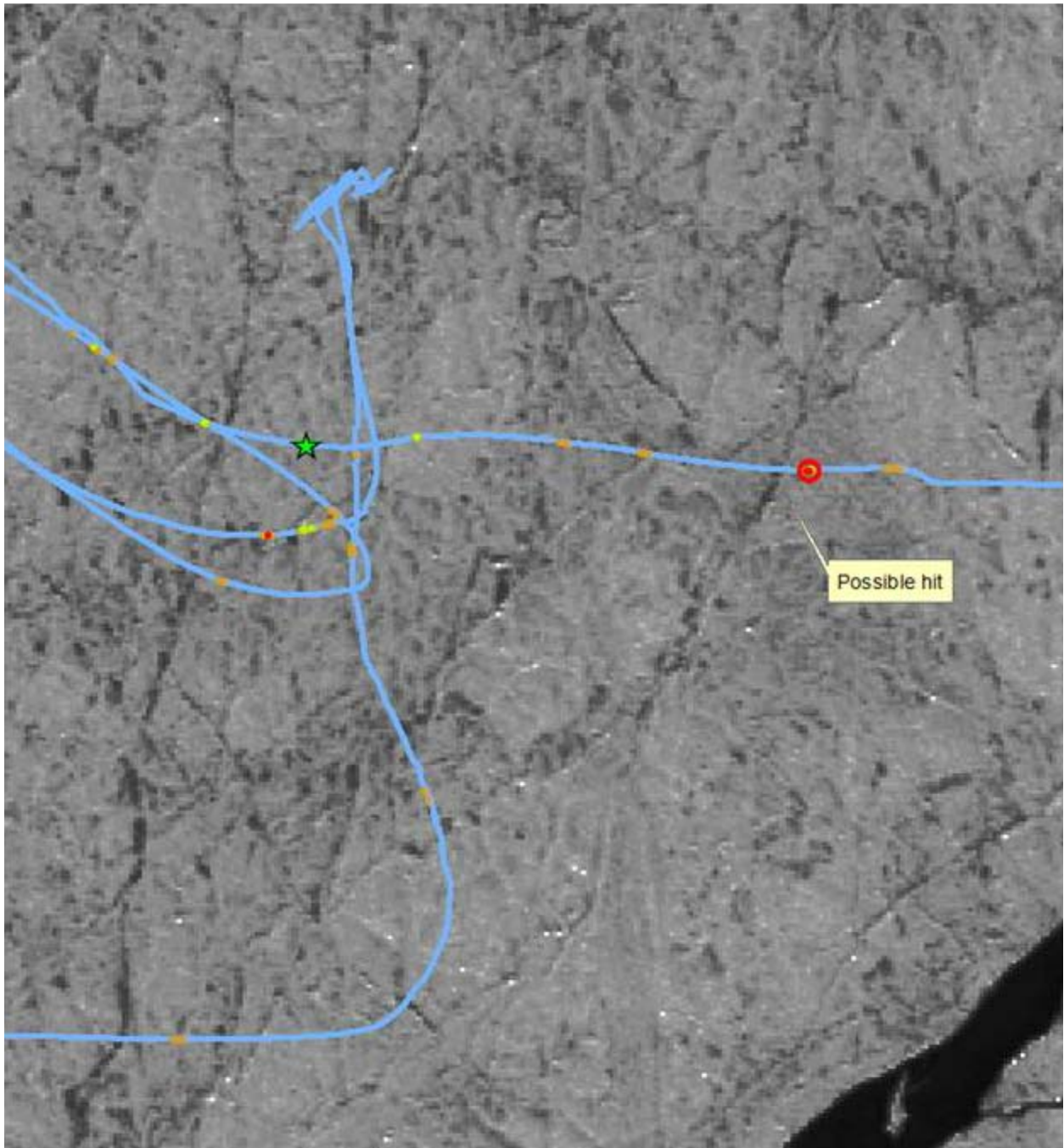


Figure 13. Possible hit for Keel 9

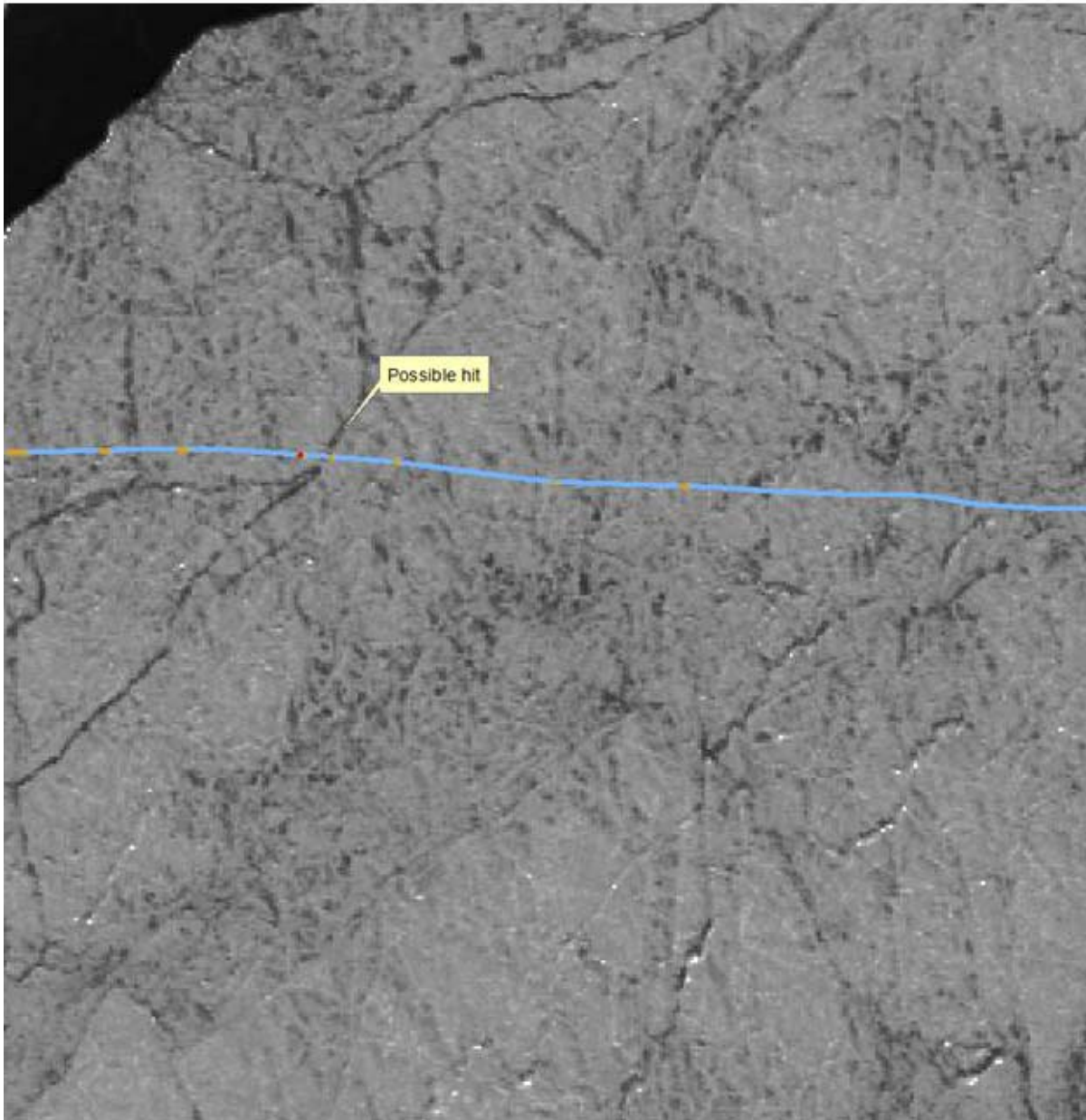


Figure 14. Possible hit for ULS draft reading > 20 m (shown in red)

4.2.3 Keel 22 and 23 in Landsat 7

ULS data for keel 22 and 23 are shown in Figure 15 and Figure 16, respectively. Coverage for keel 22 and 23 is provided with a Landsat 7 image shown in Figure 17. Note that Landsat 7 suffered a partial failure in 2003 when its Scan Line Corrector (SLC) unexpectedly stopped operating. The purpose of the SLC is to compensate for the forward motion (along-track) of the satellite so that the resulting scans are aligned parallel to each other. Without the effects of the SLC, the instrument images the earth in a "zig-zag" fashion, resulting in some areas that are

imaged twice and others that are not imaged at all. When it was working, the SLC corrected these gaps. The SLC failure has resulted in systematic gaps (black stripes) in every Landsat 7 image collected since that time. The net effect is that approximately one-fourth of the data in a Landsat 7 scene is missing when acquired without a functional SLC.

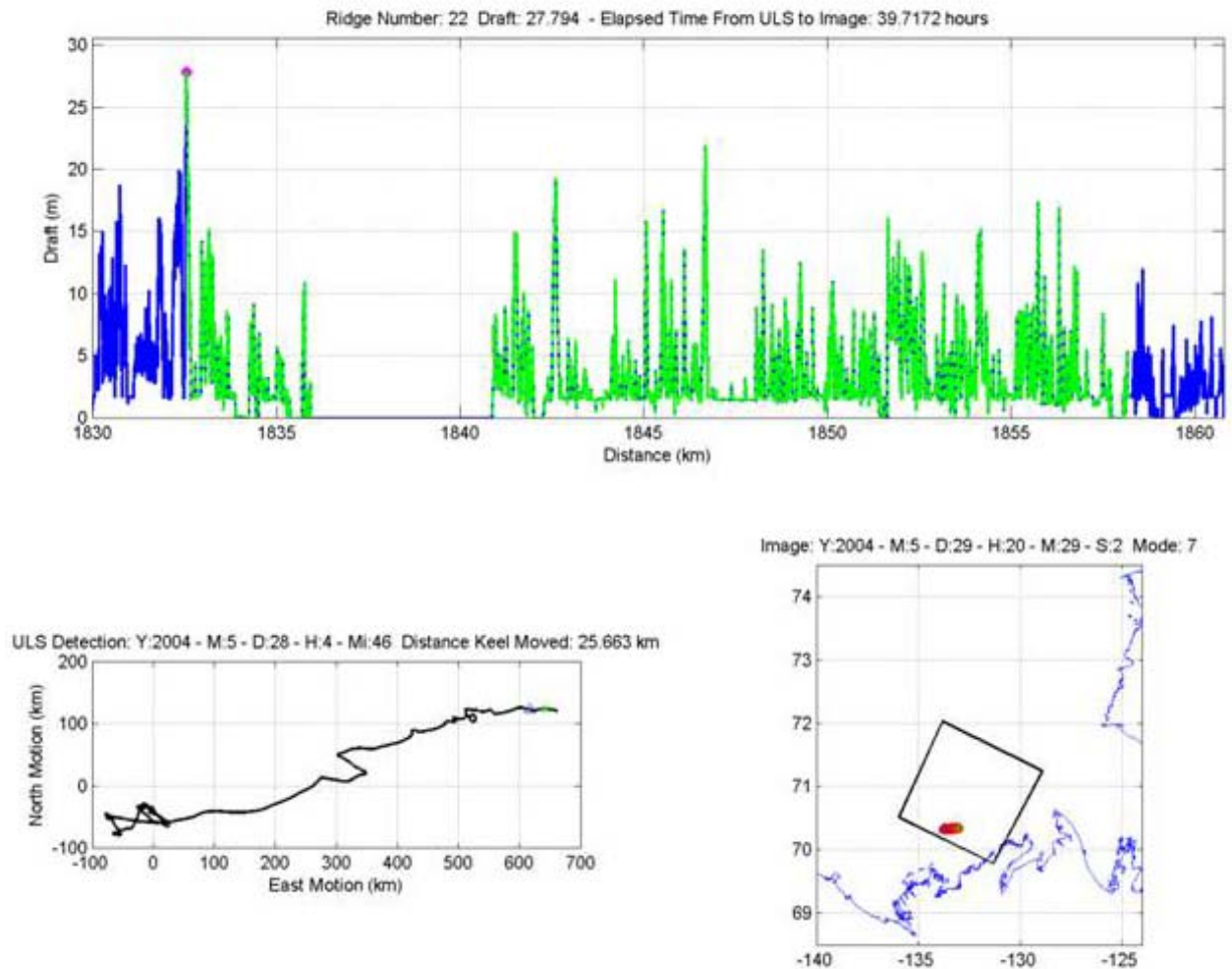


Figure 15. Sea ice draft profile (top), projected drift trajectory (bottom left) and imagery keel location (bottom right) for Keel 22

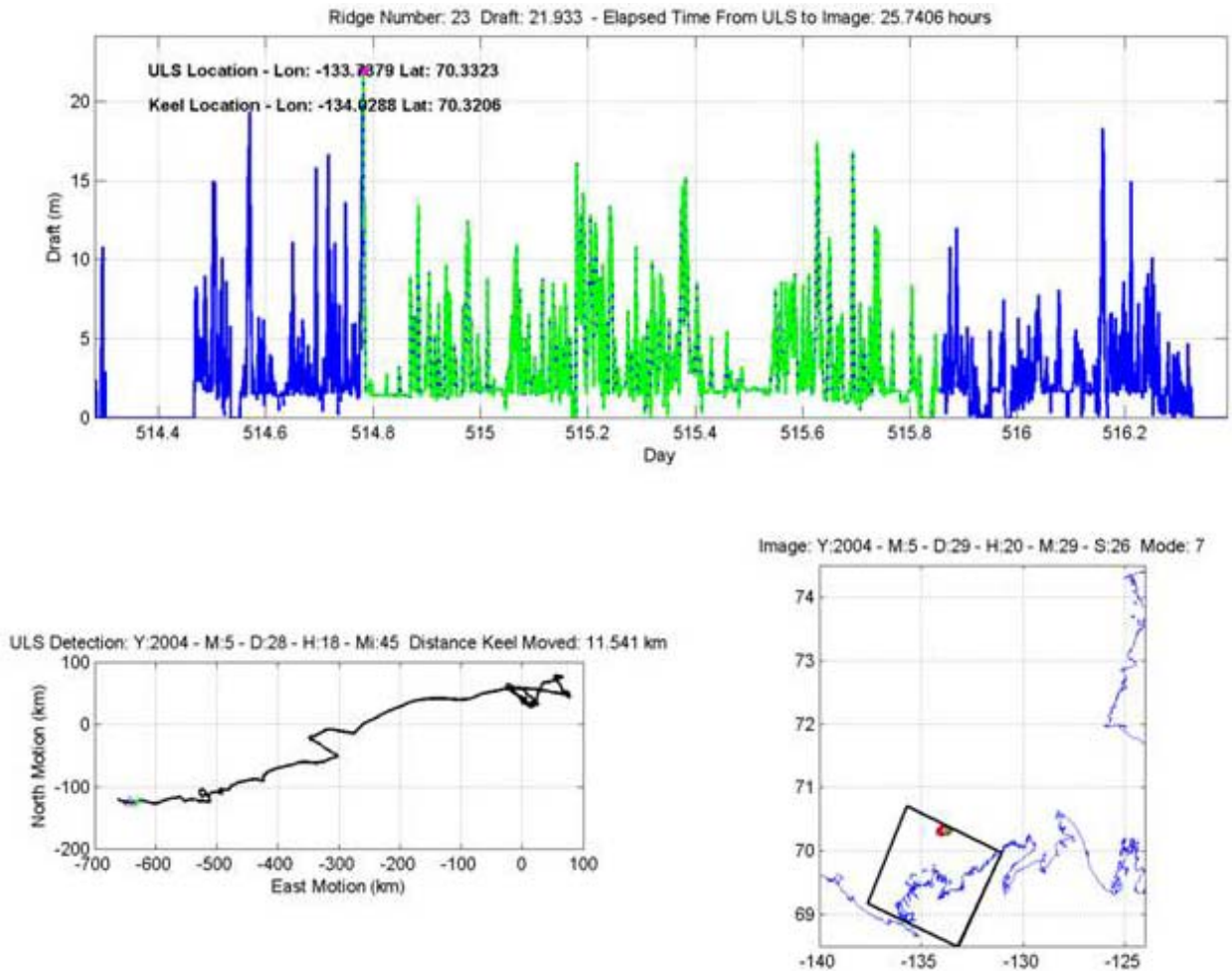


Figure 16. Sea ice draft profile (top), projected drift trajectory (bottom left) and imagery keel location (bottom right) for Keel 23

The CIS classifies sea ice at the site of keel 22 and 23 as first-year thick with trace amounts of old ice. Unfortunately, given the time of year, the sea ice is in an advanced stage of break-up. Not only are the ice floes undergoing translation, they are also rotating and correlation with the ULS data is somewhat suspect at best. As shown in Figure 17, although the dark blue sections along the drift trajectory show reasonable agreement with the open water on the image, the projected location for keel 22 falls in open water, a clear indicator of the ice's mobility. Figure 18 shows a close up of a feature crossing the projected drift trajectory close to the keel 23 location, indicating a possible hit.

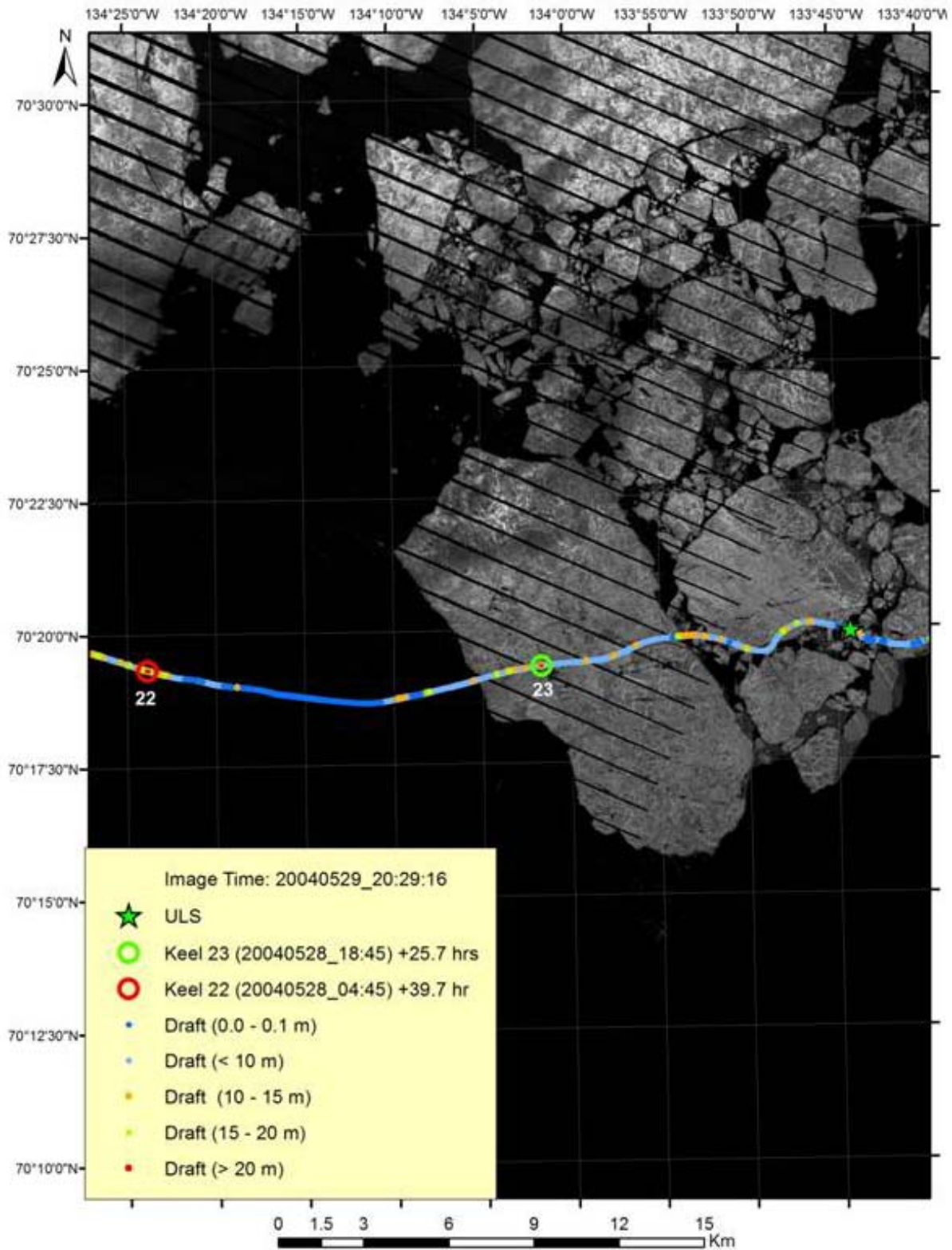


Figure 17. Landsat 7 image (acquisition time 20040529_20:29:16) for Keel 22 and Keel 23

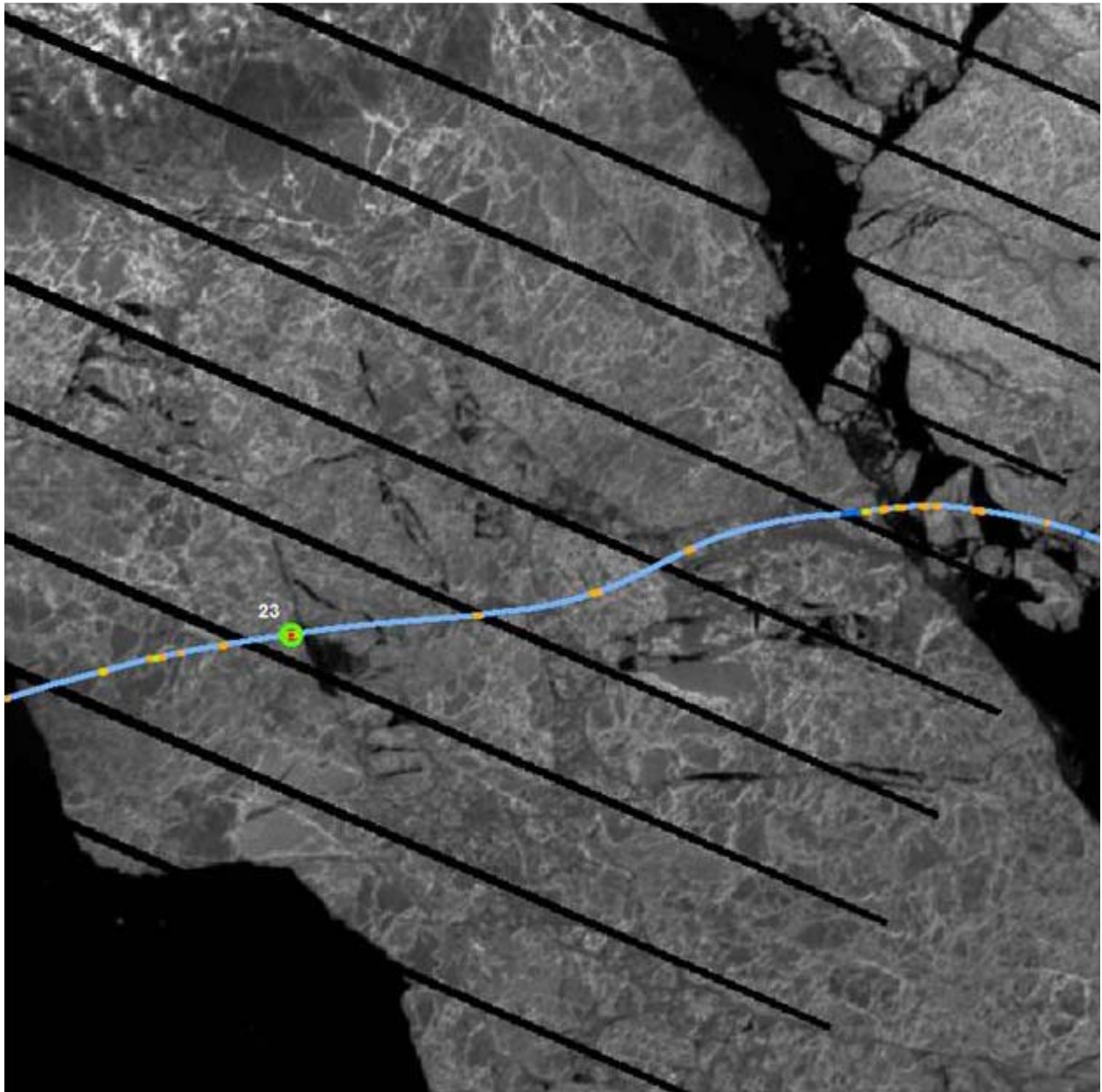


Figure 18. Possible hit for Keel 23

4.2.4 Keel 30, 31 and 32 in Envisat APP

Coverage for keels 30, 31 and 32 is provided with two Envisat APP images, acquired on 20040605 and 20040608. The CIS classifies sea ice at the site of keel 30, 31 and 32 as first-year thick with trace amounts of old ice.

ULS data for keels 30 to 32 between detection and the first Envisat image are shown in Figure 19 through Figure 21, respectively. In Figure 22, keel locations are shown on an Envisat APP image (image swath IS6, incidence angle 39.1° - 42.8°) acquired on 20040605. Several open water leads and surface features are evident throughout the image extent. The CIS classifies sea ice as first-year thick with trace amounts of old ice. A loose correlation of surface features and ULS data is evident. The acquisition date of the image is during the first week in June and the ice is likely beginning break-up and is fairly mobile, open water leads are likely opening and closing on a regular basis. As shown in Figure 23, two features crossing the projected drift trajectory suggest possible hits for keel 30 and keel 32. Given that the predicted keel locations shown in the image are approximately 35 hours prior to passing over the ULS, this is a low confidence observation.

ULS data for keels 30 to 32 between detection and the second Envisat image are shown in Figure 24 through Figure 26, respectively. Keels 30 to 32 are shown on an Envisat APP image (image swath IS5, incidence angle 35.8° - 39.4°) acquired on 20040608 (Figure 27). Several open water leads and surface features are evident throughout the image extent. The CIS classifies sea ice as first-year thick with trace amounts of old ice. A loose correlation of surface features and ULS data is evident. The acquisition date of the image is during the first week in June and the ice is likely beginning break-up and is fairly mobile, open water leads are likely opening and closing on a regular basis. As shown in Figure 28, the only notable observation is the fact that all three keels appear to fall in a section of rough ice, possibly a rubble field or multi-year floe.

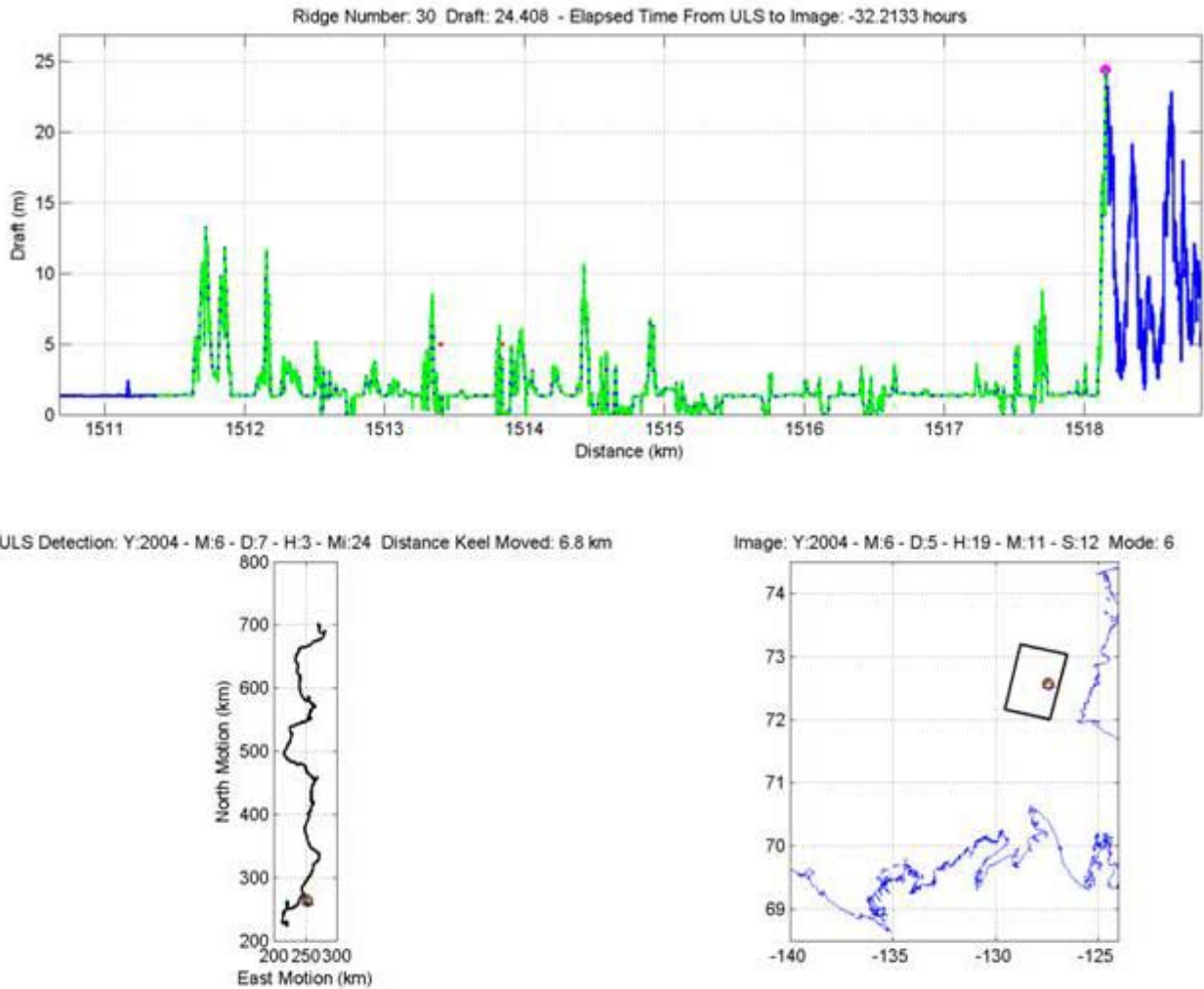
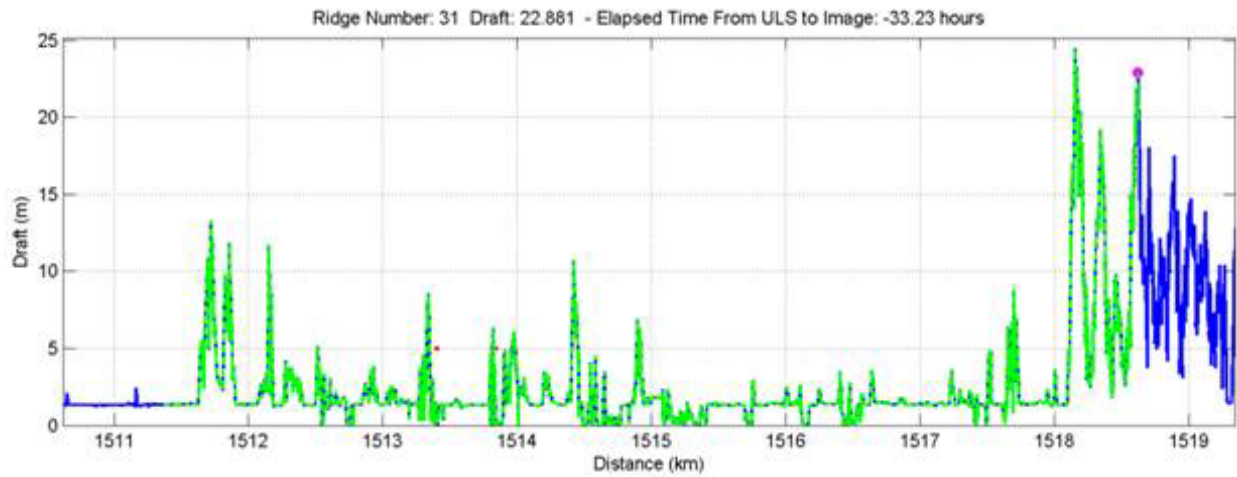


Figure 19. Sea ice draft profile (top), projected drift trajectory (bottom left) and imagery keel location (bottom right) for Envisat APP image (acquisition time 20040605_19:11:08) for Keel 30



ULS Detection: Y:2004 - M:6 - D:7 - H:4 - Mi:25 Distance Keel Moved: 7.271 km

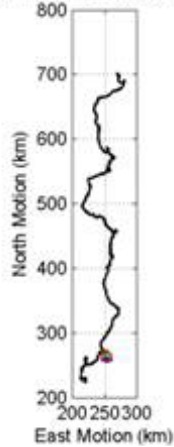


Image: Y:2004 - M:6 - D:5 - H:19 - M:11 - S:12 Mode: 6

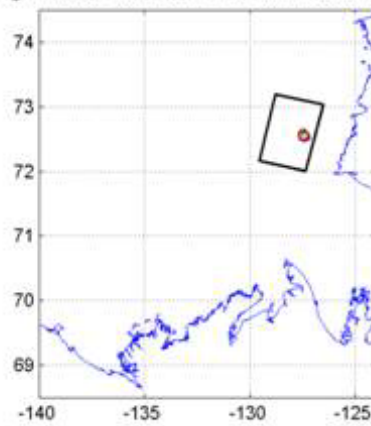
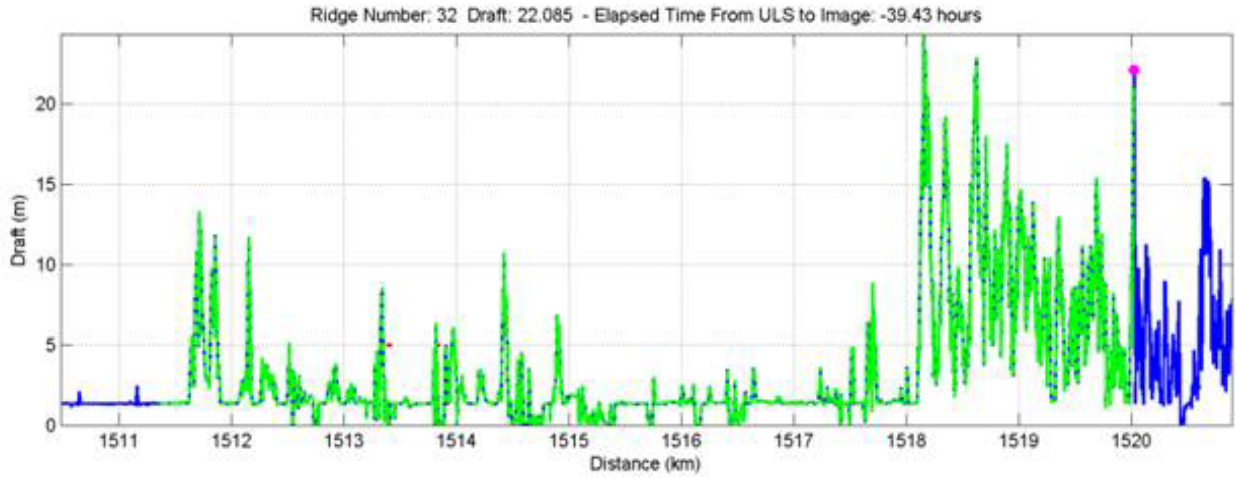


Figure 20. Sea ice draft profile (top), projected drift trajectory (bottom left) and imagery keel location (bottom right) for Envisat APP image (acquisition time 20040605_19:11:08) for Keel 31



ULS Detection: Y:2004 - M:6 - D:7 - H:10 - Mi:37 Distance Keel Moved: 8.671 km

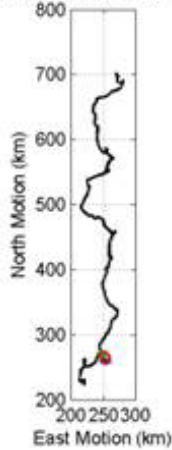


Image: Y:2004 - M:6 - D:5 - H:19 - M:11 - S:12 Mode: 6

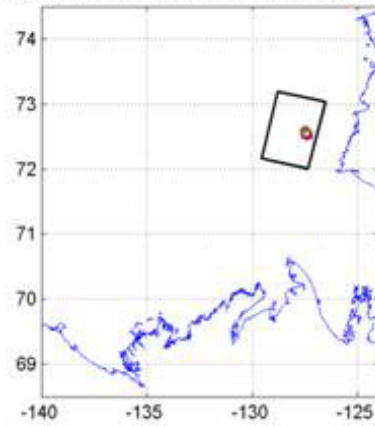


Figure 21. Sea ice draft profile (top), projected drift trajectory (bottom left) and imagery keel location (bottom right) for Envisat APP image (acquisition time 20040605_19:11:08) for Keel 32

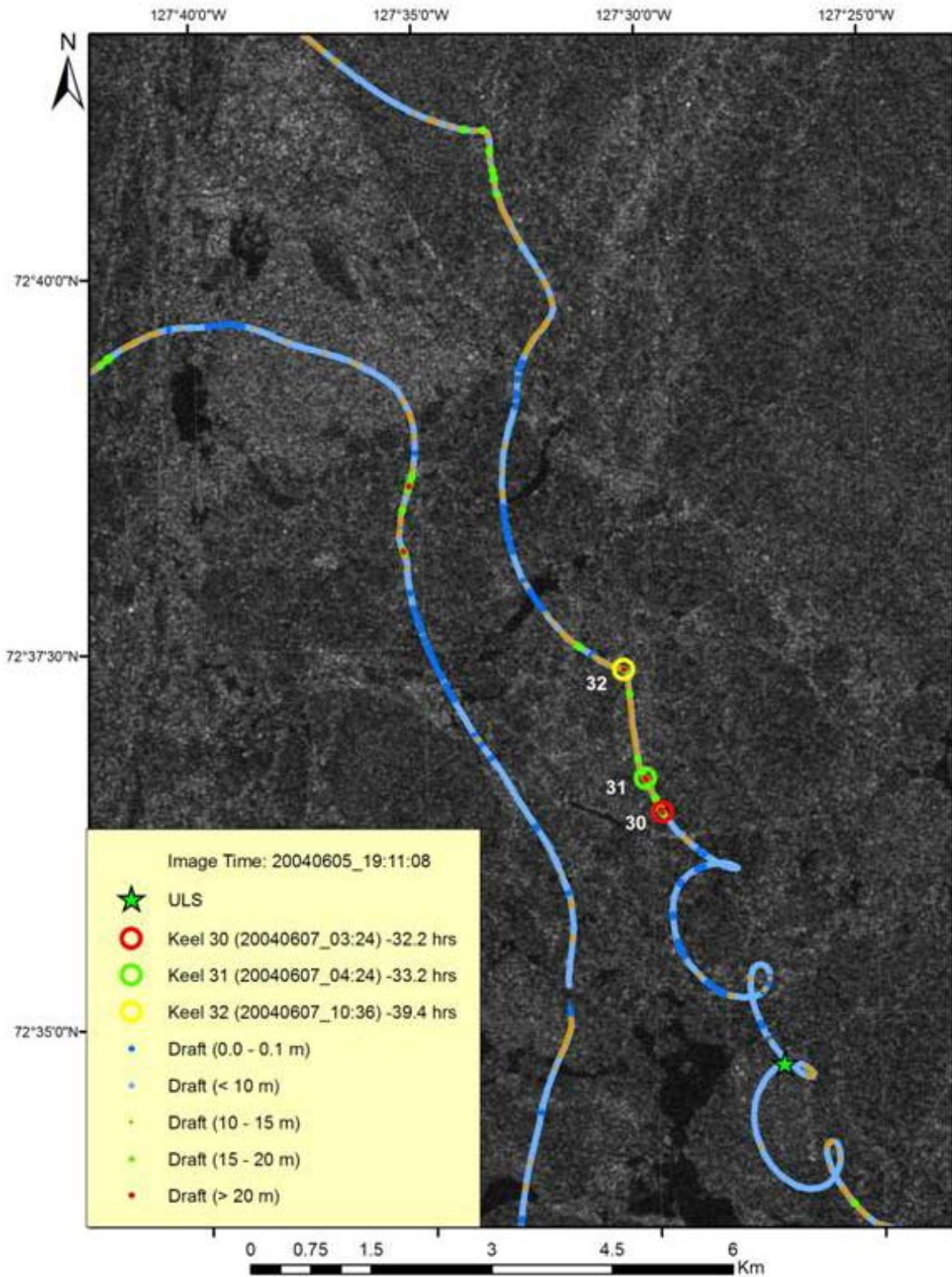


Figure 22. Envisat APP image (acquisition time 20040605_19:11:08) for Keel 30, Keel 31 and Keel 32

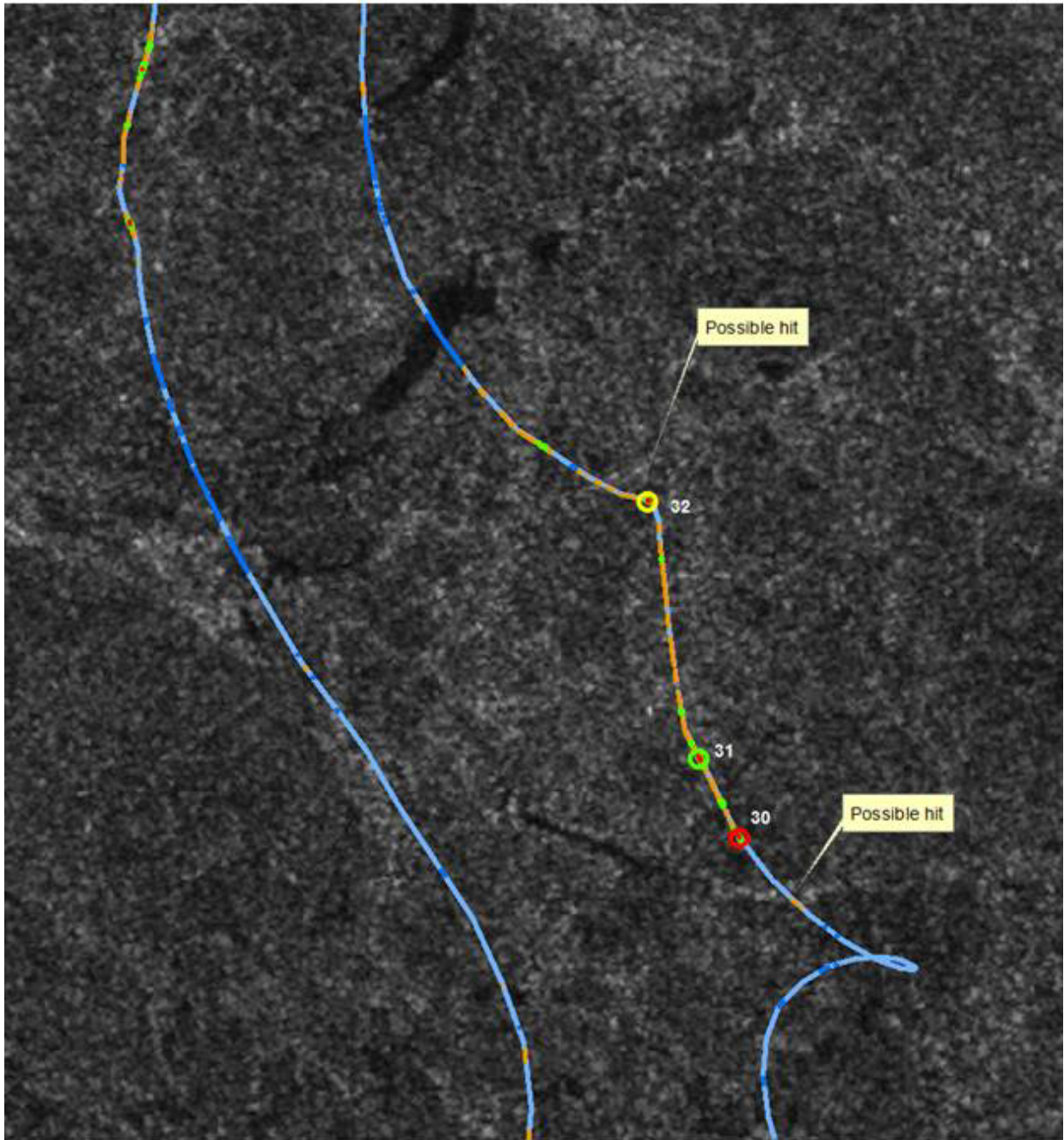


Figure 23. Possible hits for keel 30 and 32

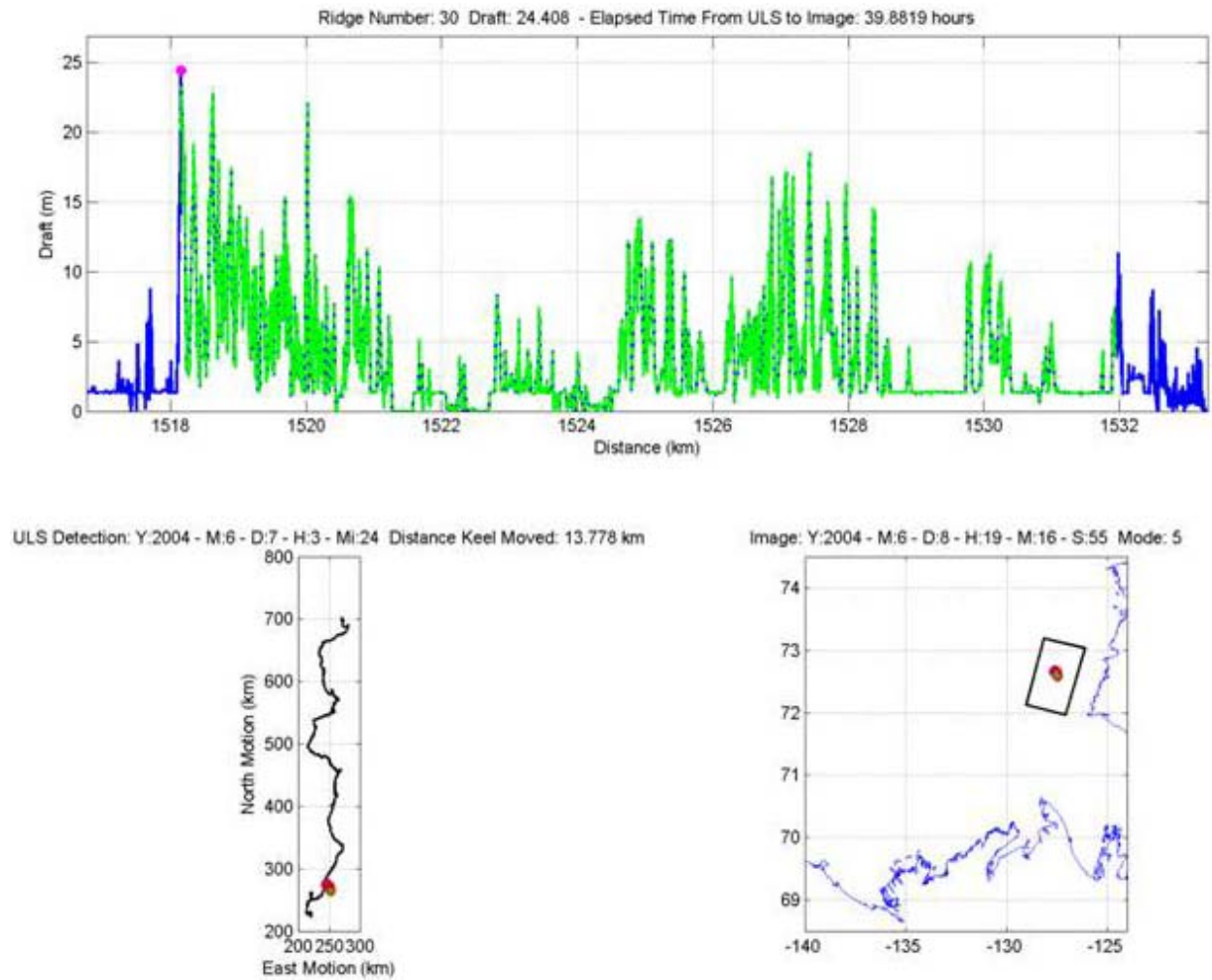


Figure 24. Sea ice draft profile (top), projected drift trajectory (bottom left) and imagery keel location (bottom right) for Envisat APP image (acquisition time 20040608_19:16:53) for Keel 30

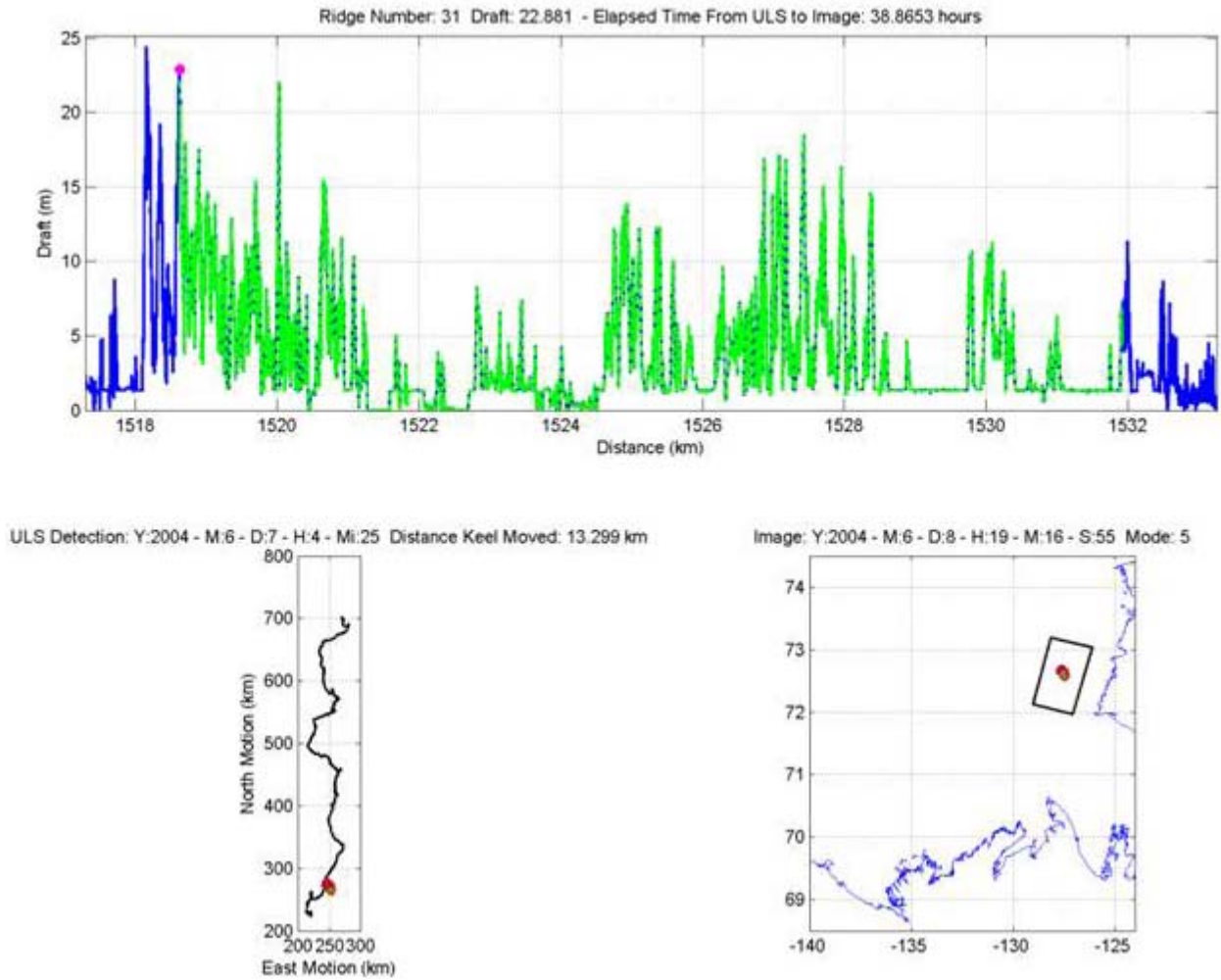


Figure 25. Sea ice draft profile (top), projected drift trajectory (bottom left) and imagery keel location (bottom right) for Envisat APP image (acquisition time 20040608_19:16:53) for Keel 31

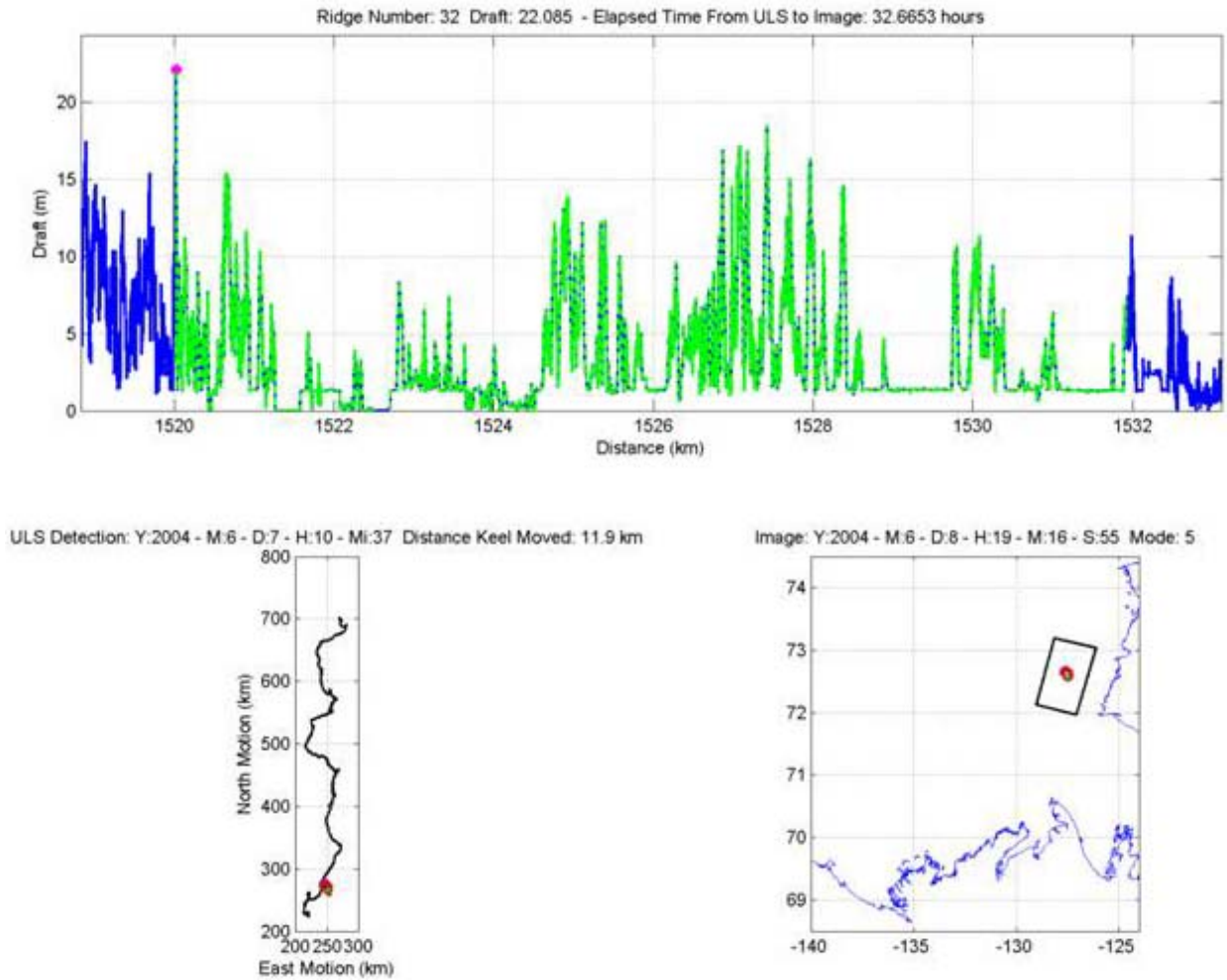


Figure 26. Sea ice draft profile (top), projected drift trajectory (bottom left) and imagery keel location (bottom right) for Envisat APP image (acquisition time 20040608_19:16:53) for Keel 32

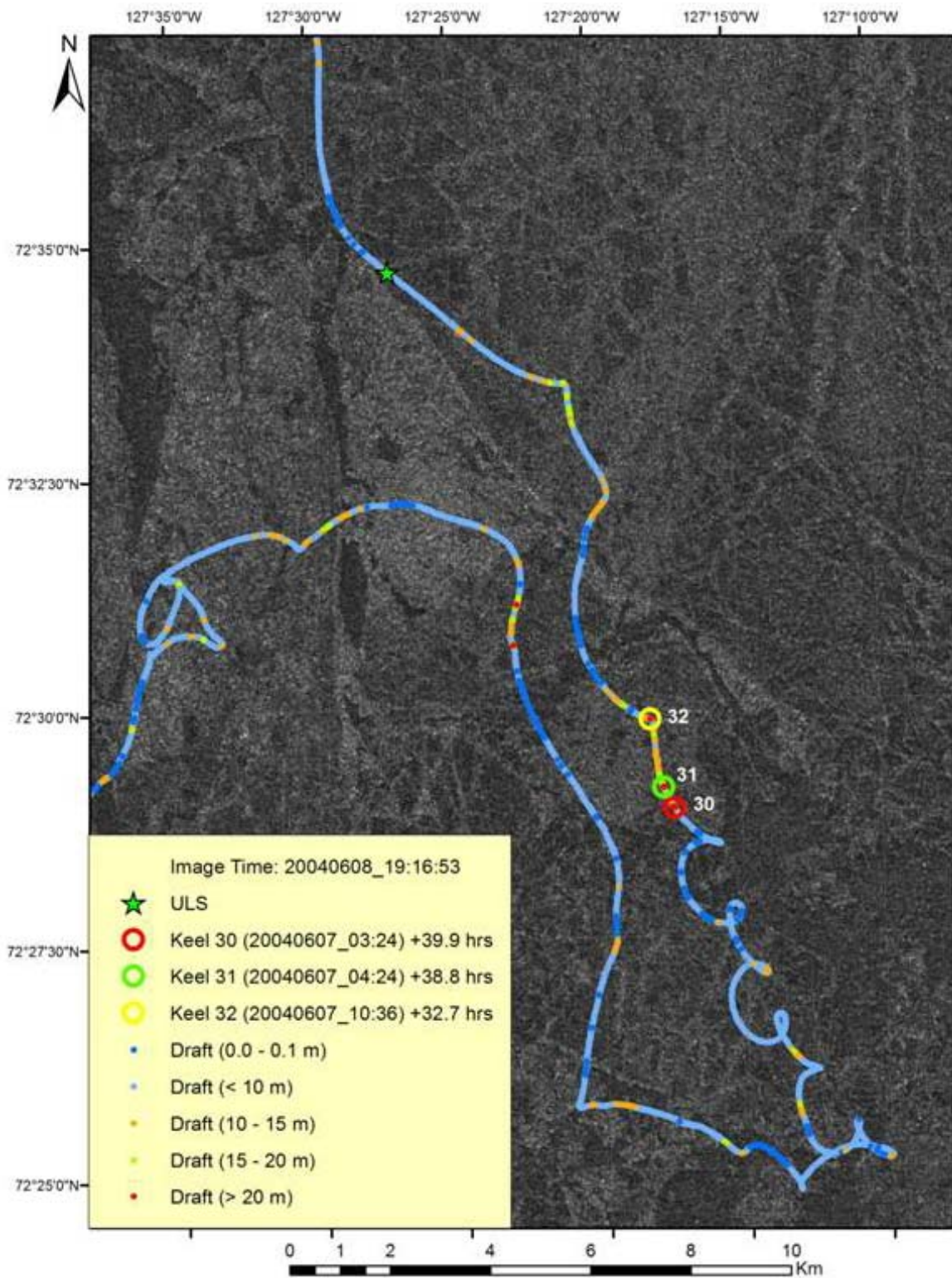


Figure 27. Envisat APP image (acquisition time 20040608_19:16:53) for Keel 30, Keel 31 and Keel 32

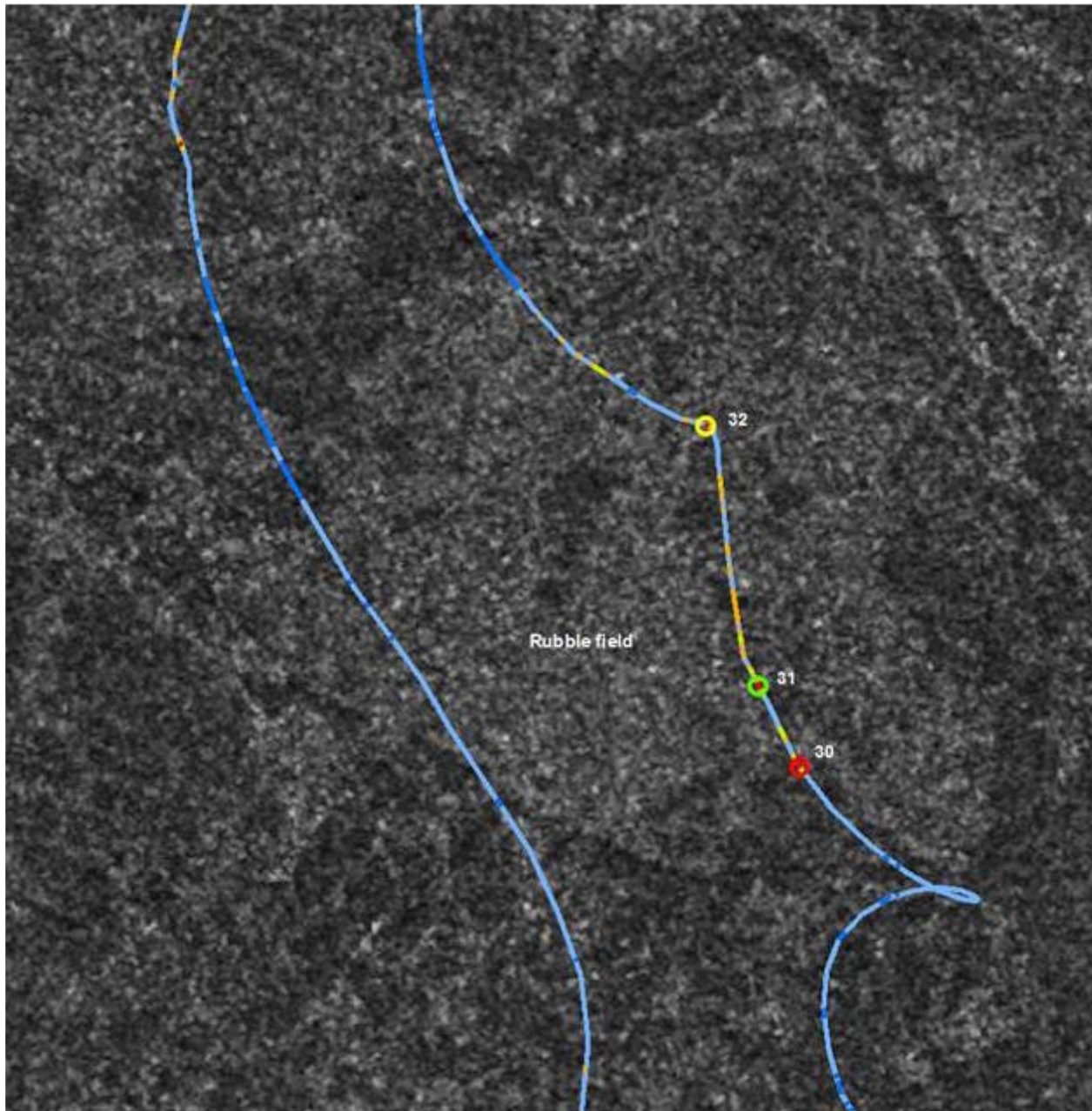


Figure 28. Proximity of keels 30 – 32 with inferred rubble field

4.2.5 Keel 33 in Envisat APP

ULS data for keel 33 collected between the time of detection and image acquisition are shown in Figure 29. Keel 33 location is shown in Figure 30, an Envisat APP image (image swath IS5, incidence angle 35.8° - 39.4°). Several open water leads and surface features are evident throughout the image extent. The CIS classifies sea ice at the site of keel 33 as first-year thick with trace amounts of old ice. ULS data indicates ice drafts predominantly less than 10 m in depth suggesting level ice throughout most of the drift trajectory. Poor correlation of surface

features and ULS data is evident. The acquisition date of the image is a week into June and the ice is likely beginning break-up and is fairly mobile, open water leads are likely opening and closing on a regular basis. At the keel location, as shown in Figure 31, a feature is noted crossing the drift trajectory just to the north indicating a 'possible' hit. Given that the predicted keel location shown in the image is approximately 35 hours prior to passing over the ULS, this is a low confidence observation.

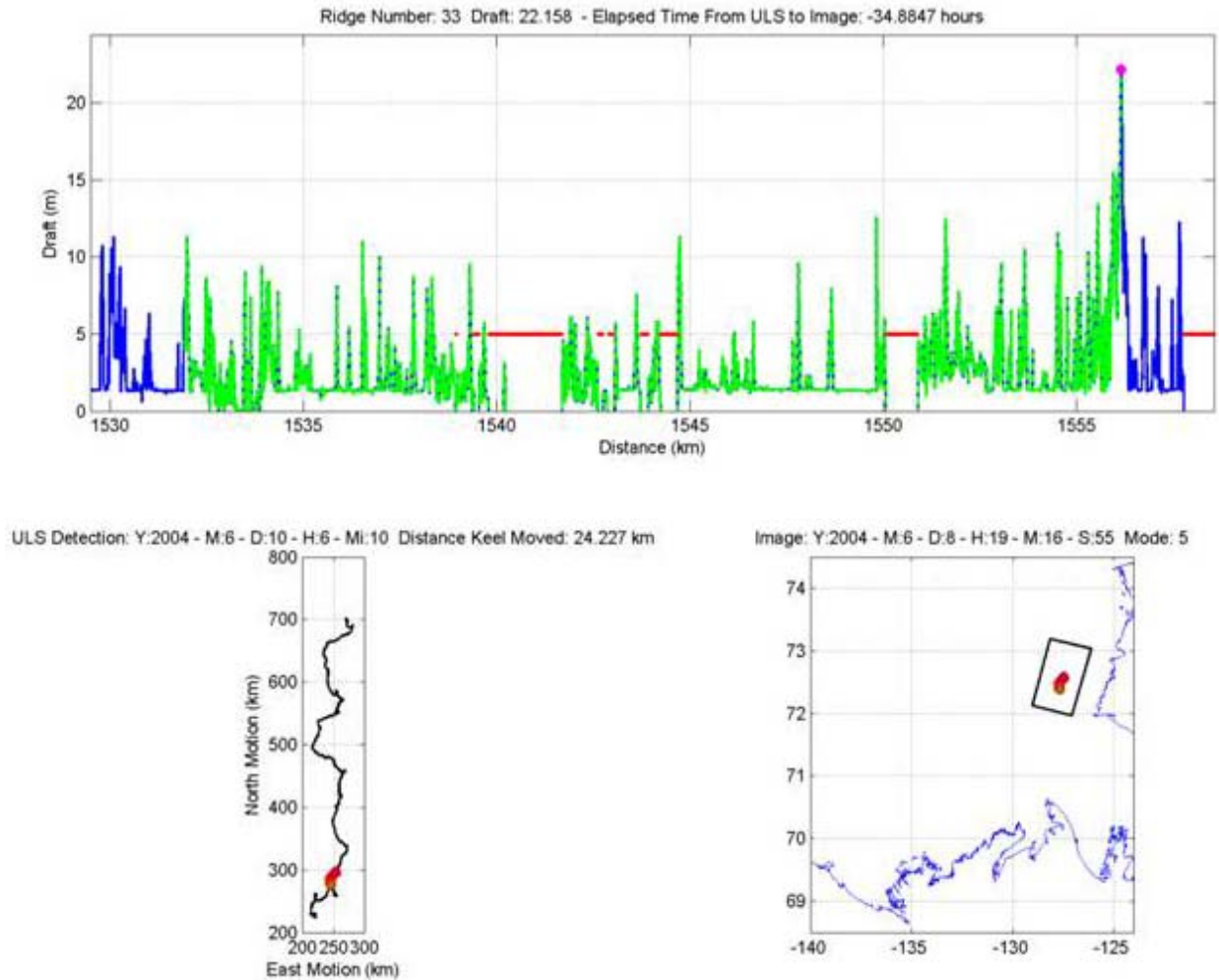


Figure 29. Sea ice draft profile (top), projected drift trajectory (bottom left) and imagery keel location (bottom right) for Keel 33

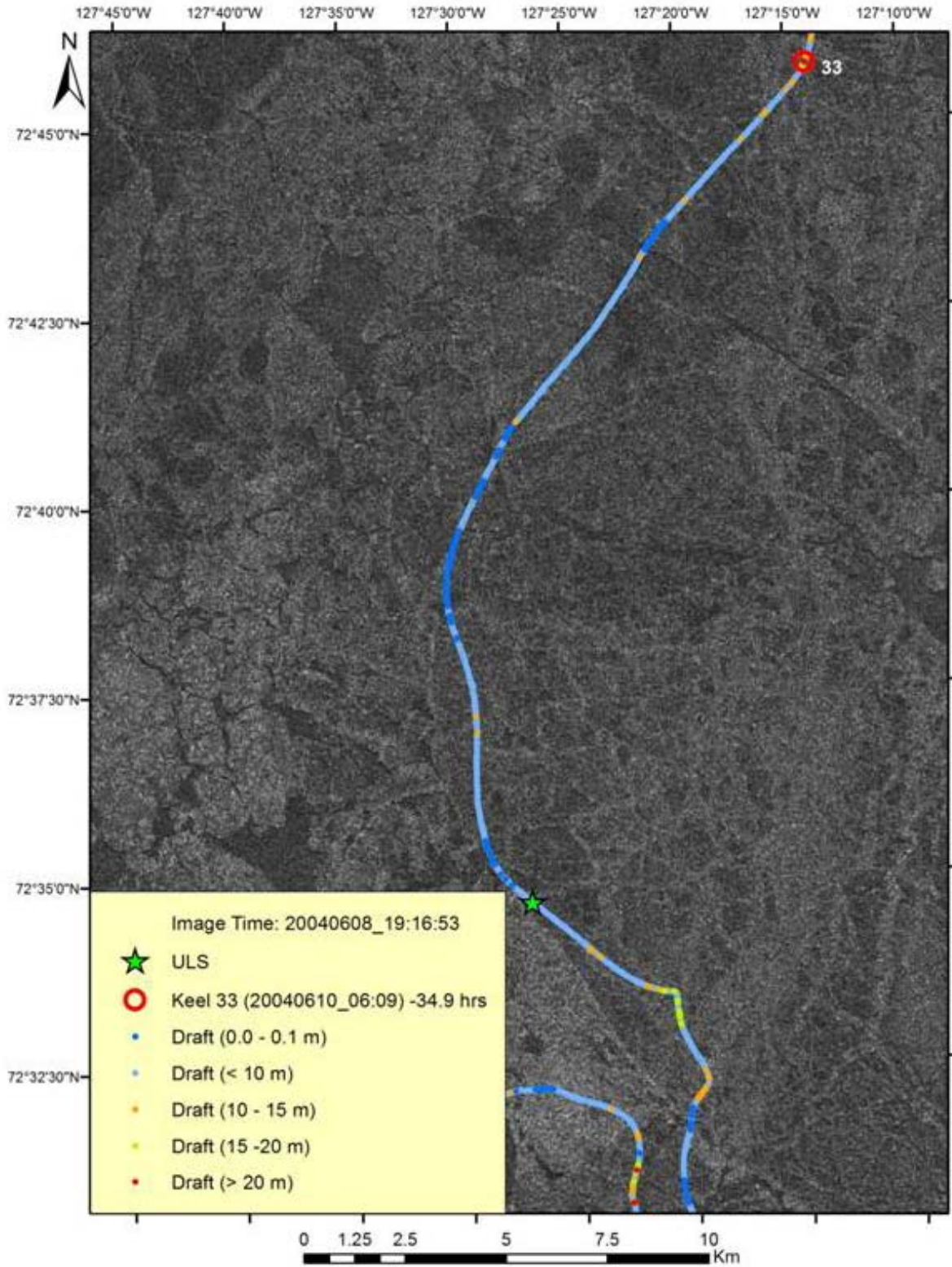


Figure 30. Envisat APP image (acquisition time 20040608_19:16:53) for Keel 33

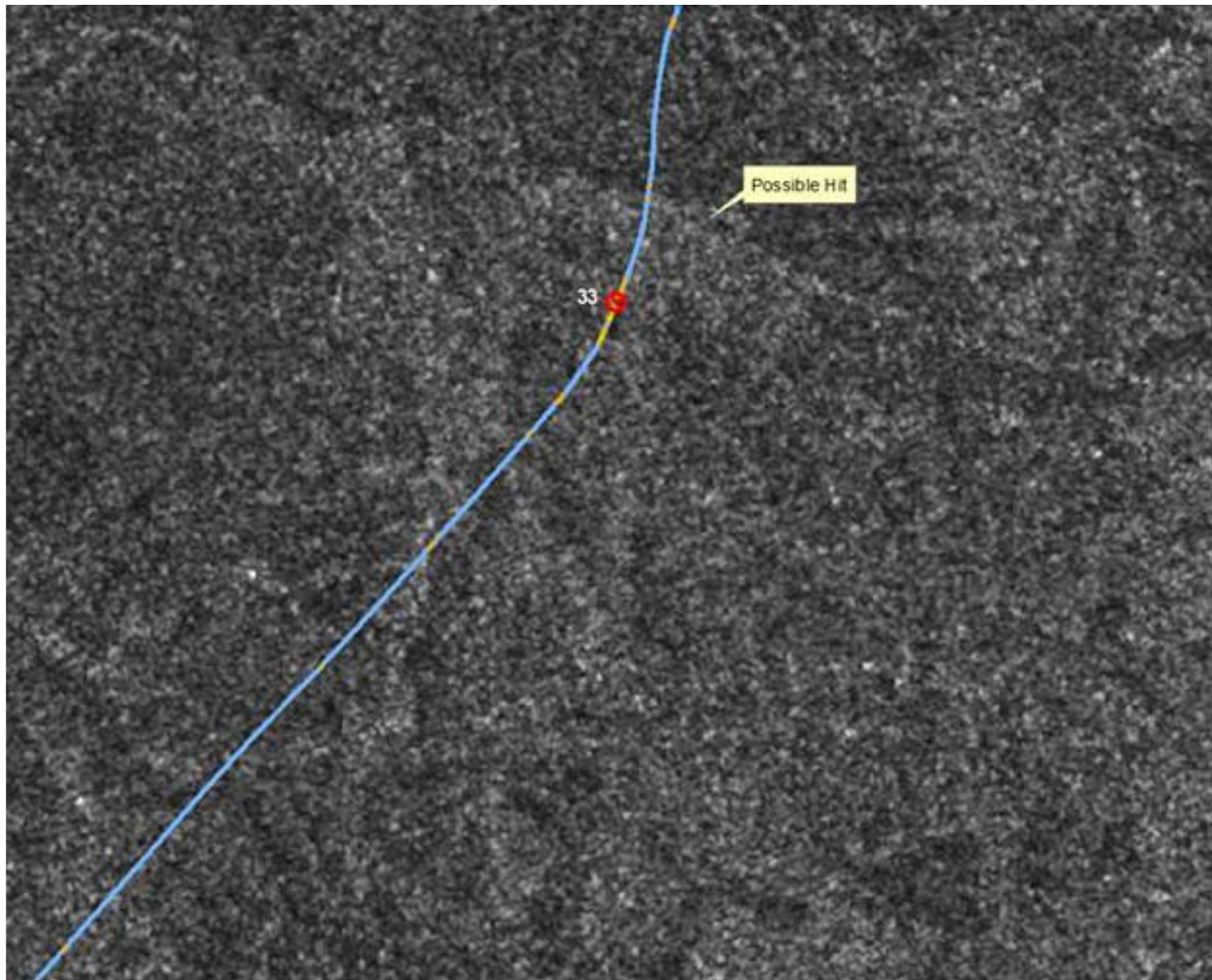


Figure 31. Possible hit for Keel 33

4.2.6 Keel 42, 43, 44 and 45 in Landsat 7

ULS data for keels 42 to 45 between detection and the Landsat 7 image are shown in Figure 32 through Figure 35, respectively. A Landsat 7 image (acquisition time 20040623_20:22:16), shown in Figure 36, shows sea ice in an advanced stage of break-up in late June. The CIS classifies sea ice at keel locations for this date as predominantly old ice mixed with small amounts of first-year thick ice. While some loose correlation with open water leads is displayed, ice floe mobility makes it highly unlikely that correlation of surface features with ULS data can be achieved with any degree of confidence.

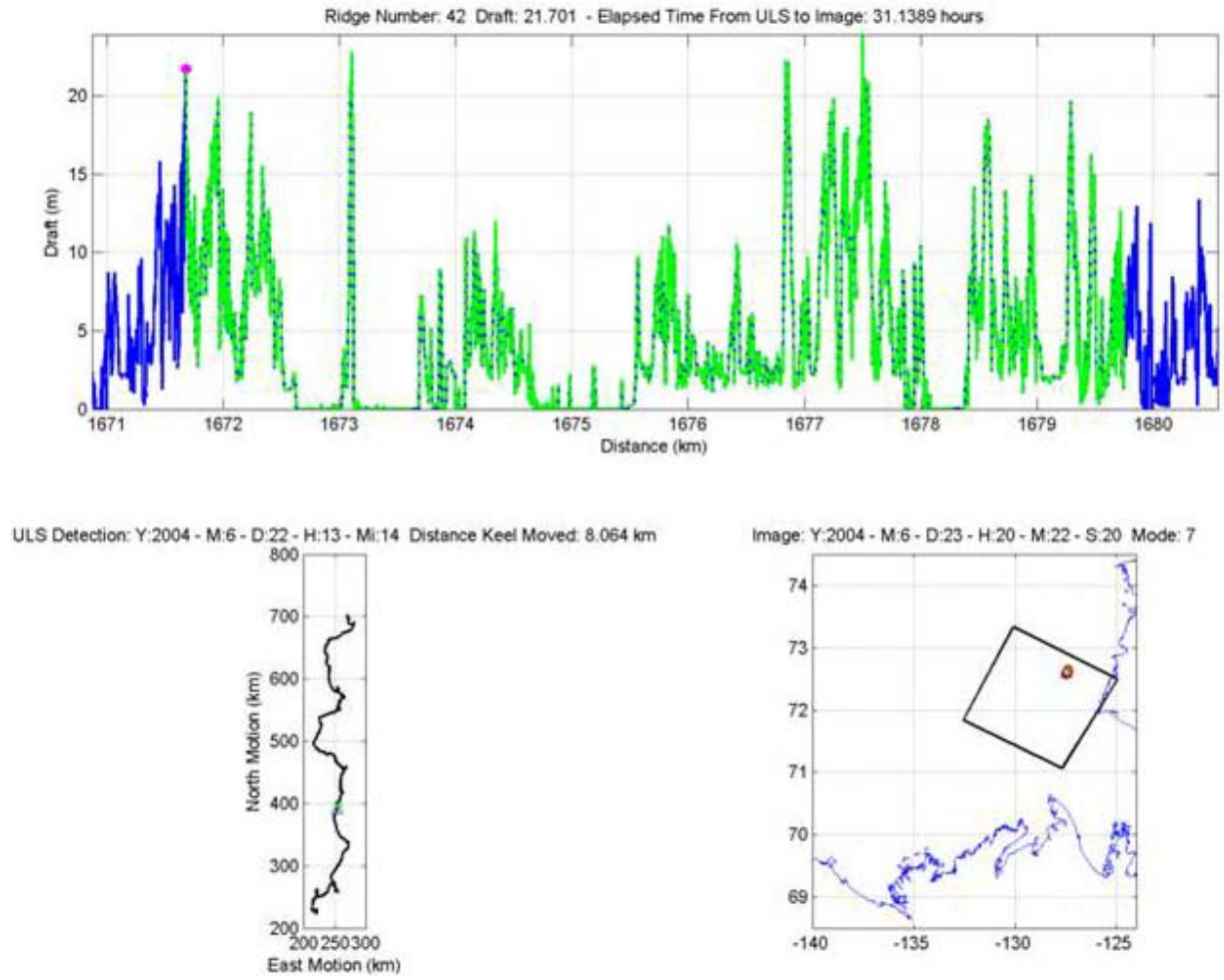
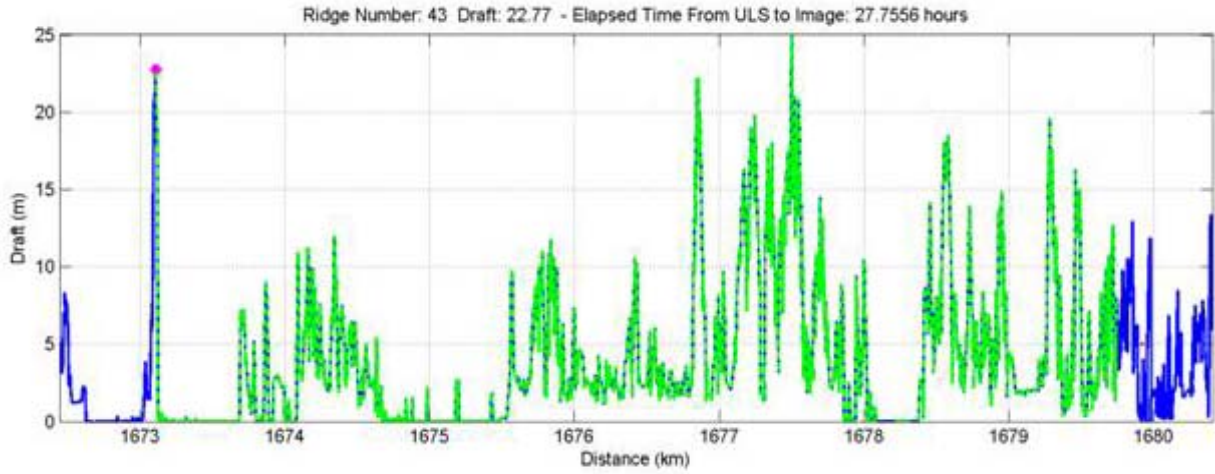


Figure 32. Sea ice draft profile (top), projected drift trajectory (bottom left) and imagery keel location (bottom right) for Keel 42



ULS Detection: Y:2004 - M:6 - D:22 - H:16 - Mi:37 Distance Keel Moved: 6.637 km

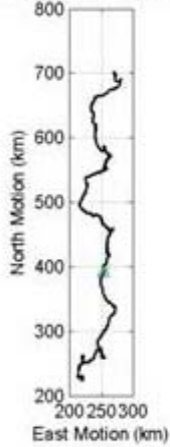


Image: Y:2004 - M:6 - D:23 - H:20 - M:22 - S:20 Mode: 7

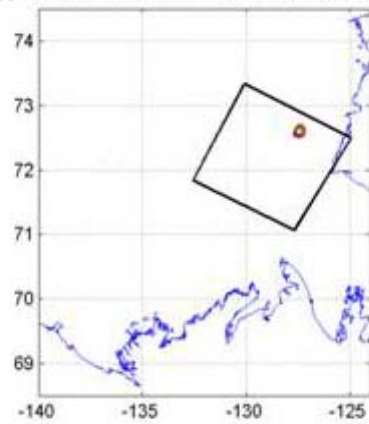


Figure 33. Sea ice draft profile (top), projected drift trajectory (bottom left) and imagery keel location (bottom right) for Keel 43

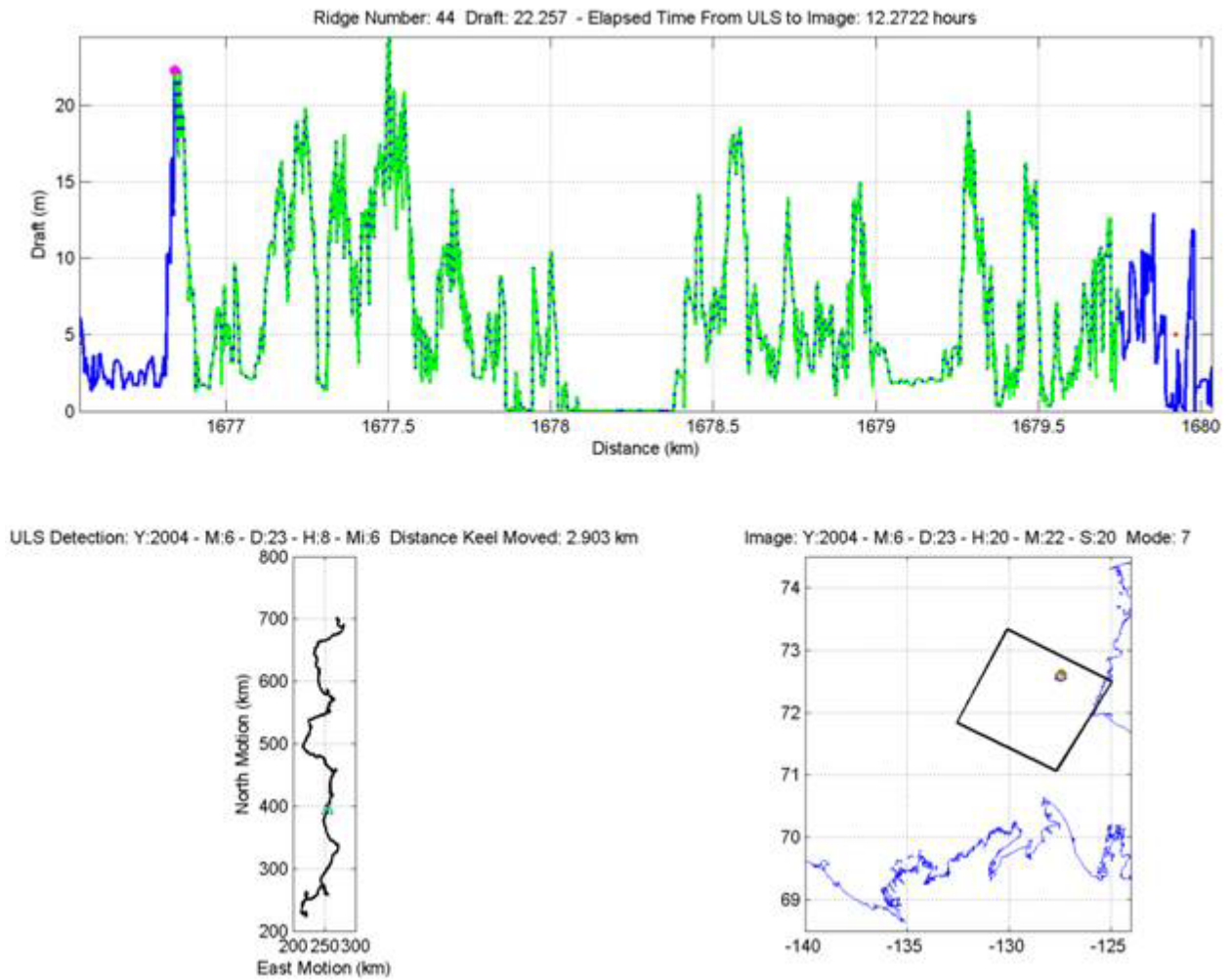
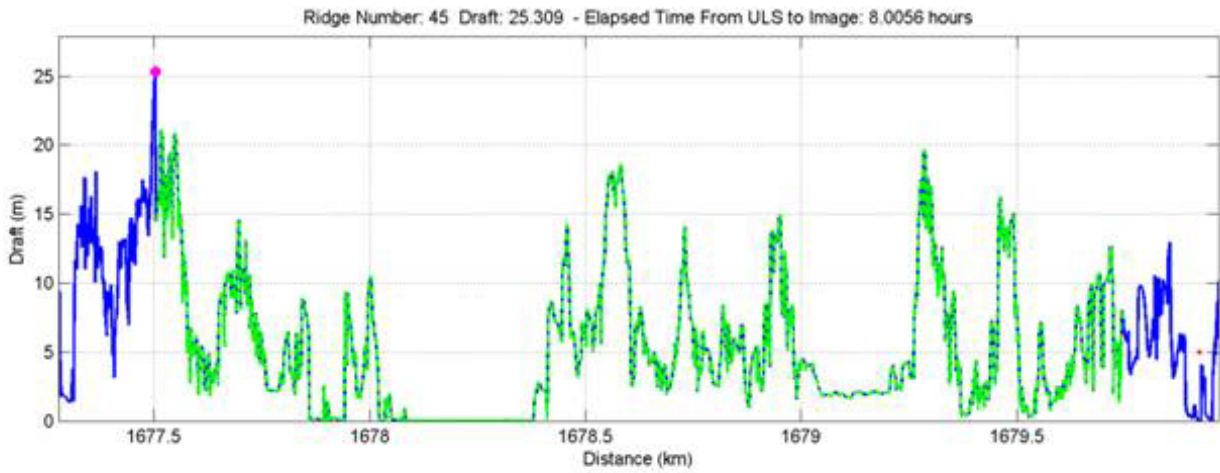


Figure 34. Sea ice draft profile (top), projected drift trajectory (bottom left) and imagery keel location (bottom right) for Keel 44



ULS Detection: Y:2004 - M:6 - D:23 - H:12 - Mi:22 Distance Keel Moved: 2.241 km

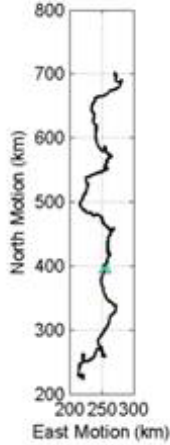


Image: Y:2004 - M:6 - D:23 - H:20 - Mi:22 - S:20 Mode: 7

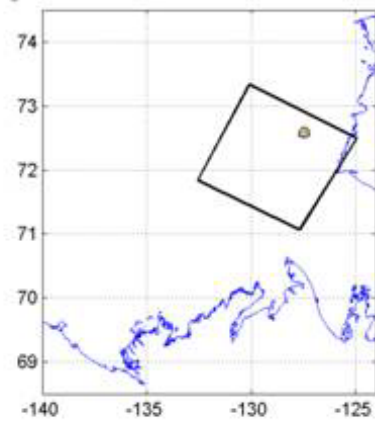


Figure 35. Sea ice draft profile (top), projected drift trajectory (bottom left) and imagery keel location (bottom right) for Keel 45

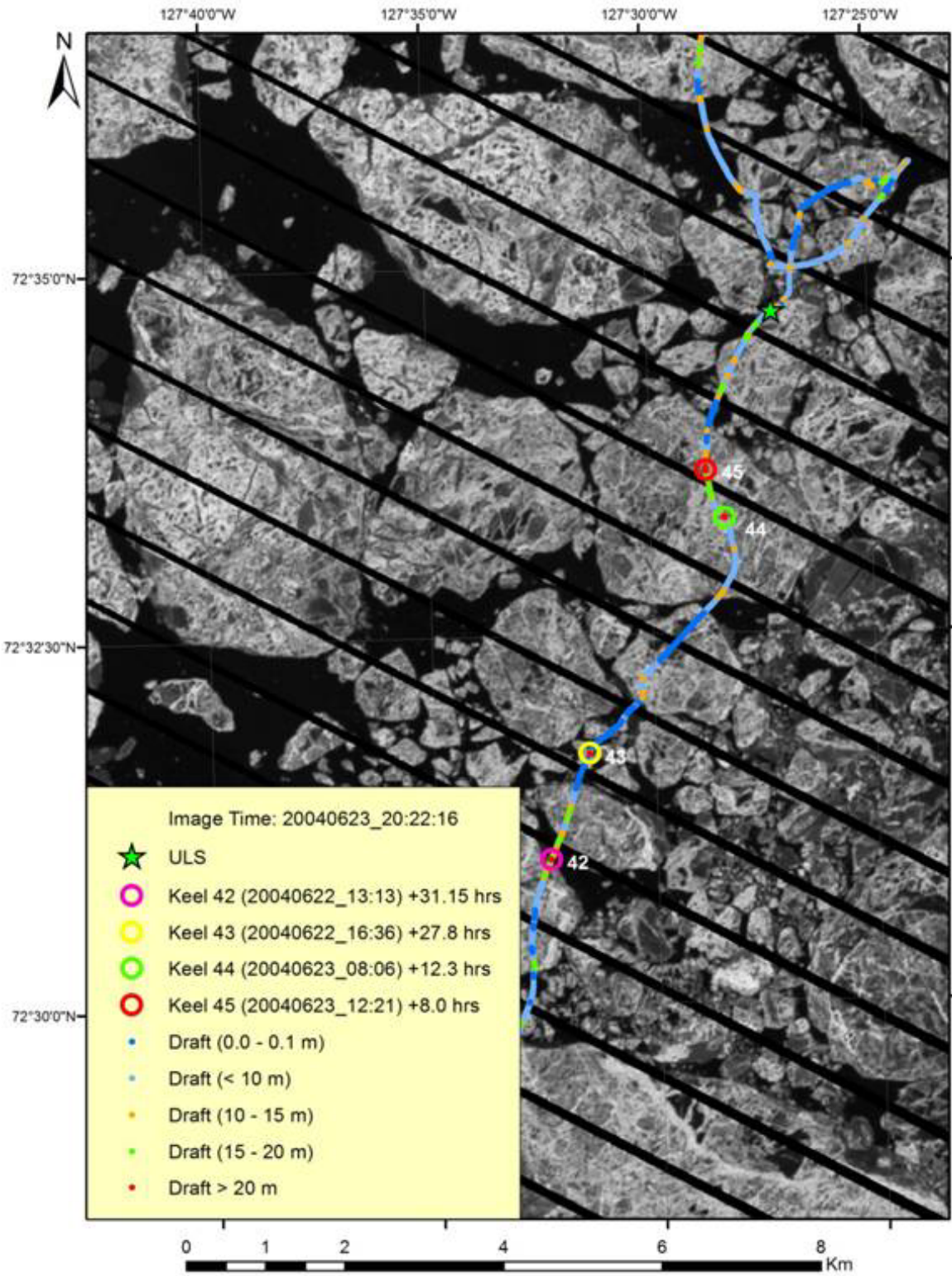


Figure 36. Landsat 7 image (acquisition time 20040623_20:22:16) for Keel 42, Keel 43, Keel 44 and Keel 45

4.2.7 Keel 50 in Landsat 7

Keel 50 was covered by two Landsat 7 images, the first on June 30 and the second on July 1. ULS data for keel 50 between detection and the first Landsat 7 image are shown in Figure 37, and the corresponding Landsat image is shown in Figure 38. Likewise, ULS data for keels 50 between detection and the second Landsat 7 image are shown in Figure 39, and the corresponding Landsat image is shown in Figure 40. A possible match with an inferred ridge feature is shown in Figure 41. Both images show sea ice in an advanced stage of break-up. The CIS classifies sea ice at the site of keel 50 as predominantly old ice with trace amounts of first-year thick ice. Similar to keels 42-45, some loose correlation with open water leads is displayed in both images, however, ice floe mobility and the opening and closing of leads makes it highly unlikely that correlation of surface features with ULS data can be achieved with any degree of confidence.

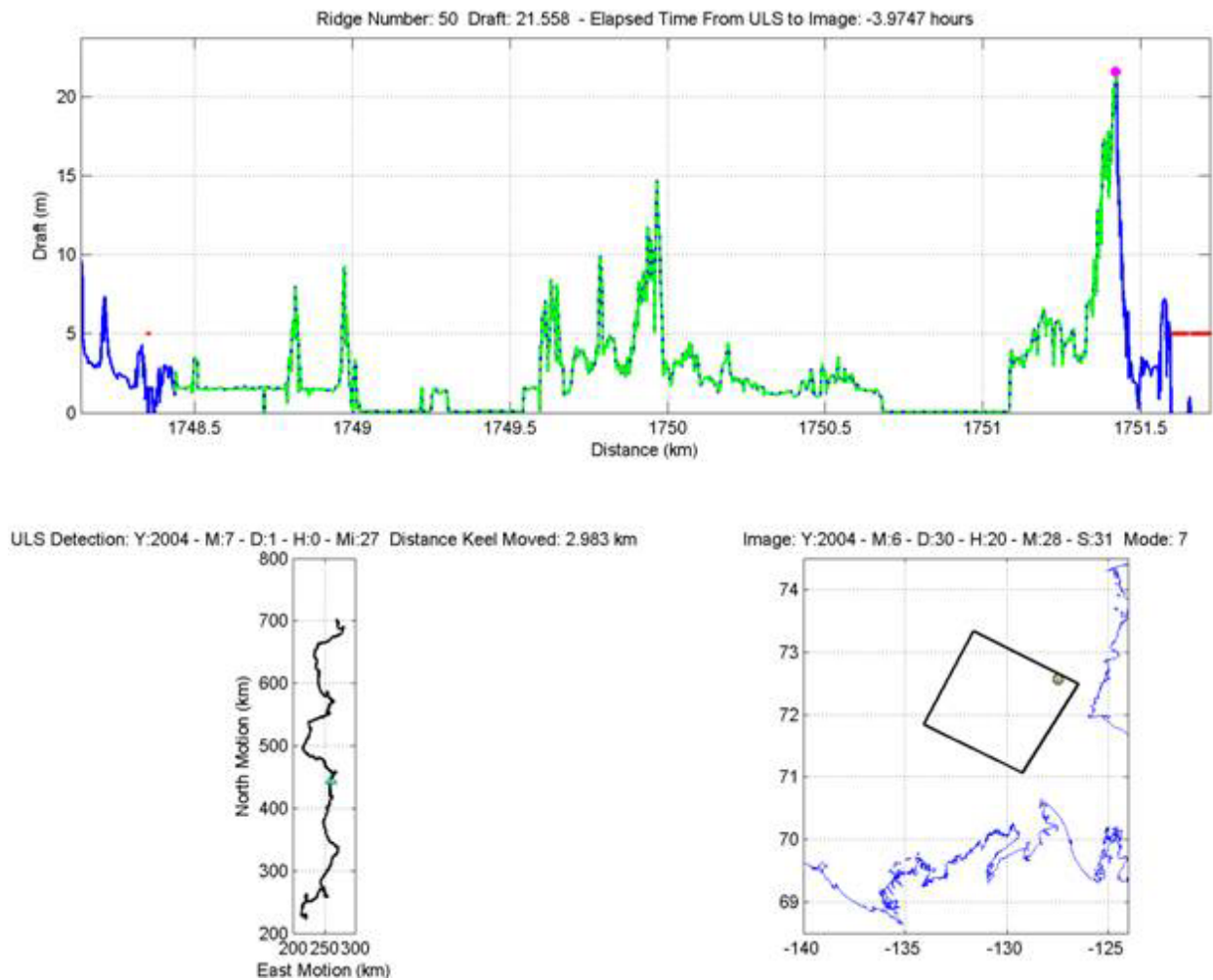


Figure 37. Sea ice draft profile (top), projected drift trajectory (bottom left) and imagery keel location (bottom right) for Keel 50 Landsat 7 image (acquisition time 20040630_20:28:28)

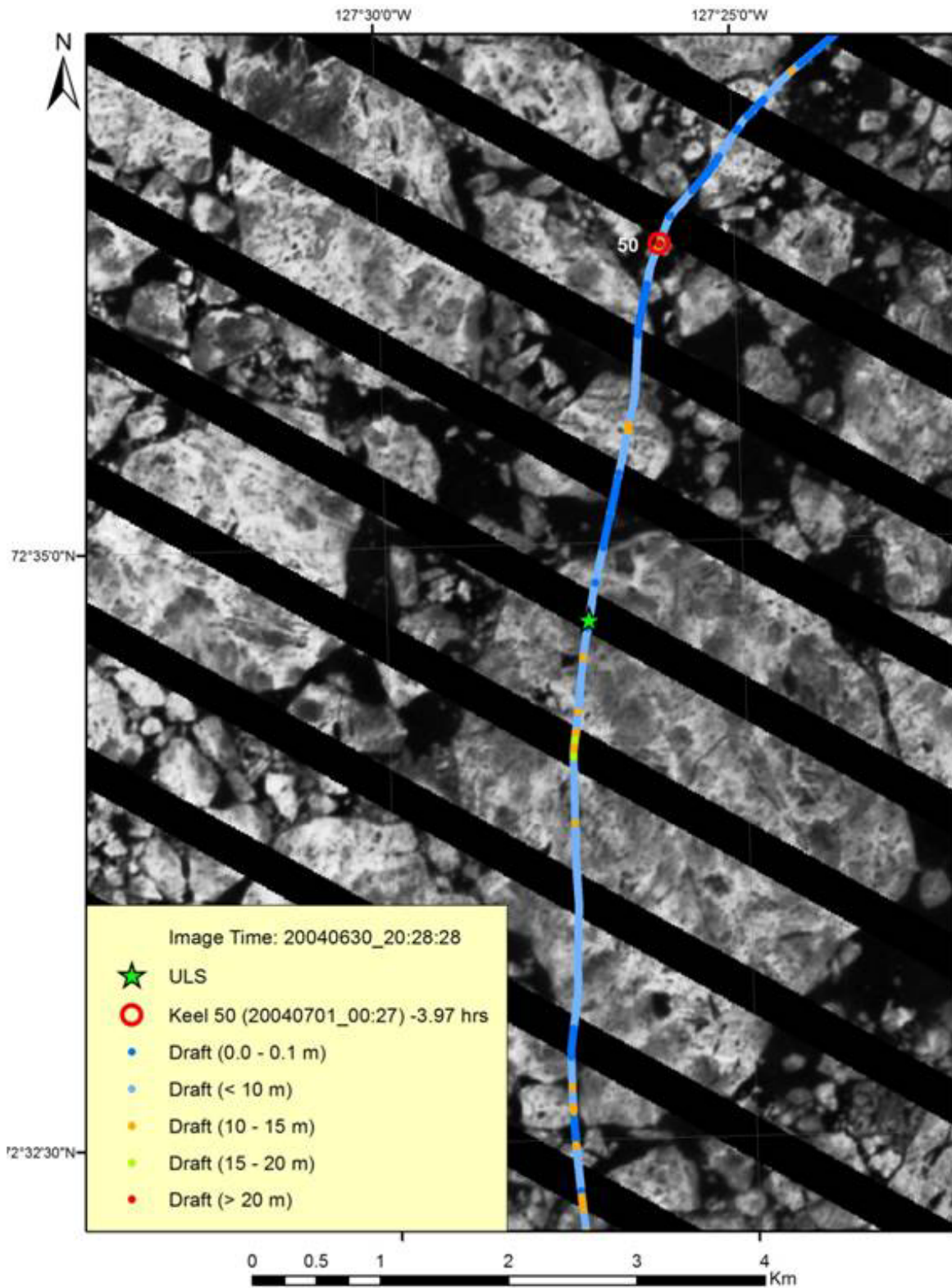


Figure 38. Landsat 7 image (acquisition time 20040630_20:28:28) for Keel 50

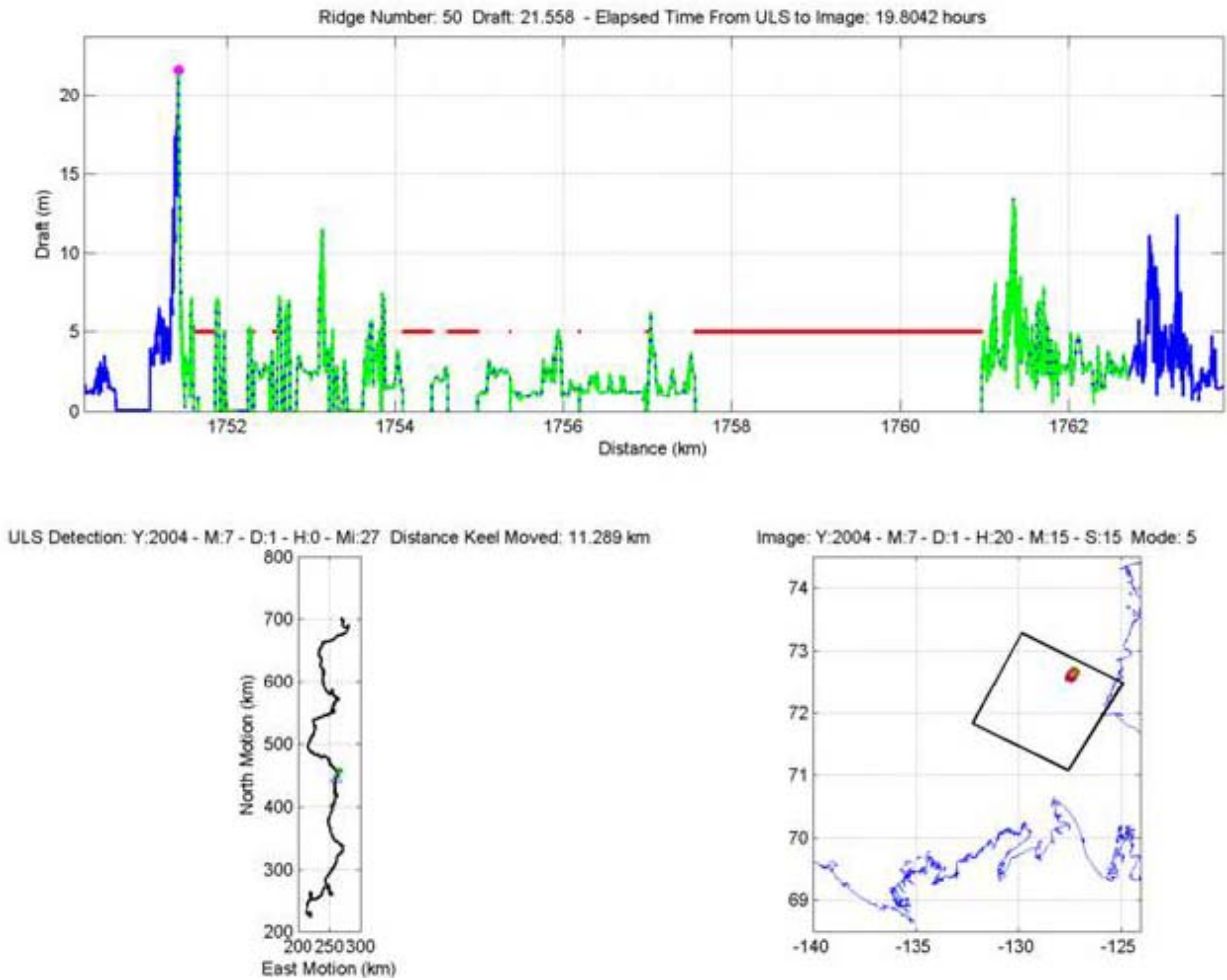


Figure 39. Sea ice draft profile (top), projected drift trajectory (bottom left) and imagery keel location (bottom right) for Keel 50 Landsat 5 image (acquisition time 20040701_20:15:28)

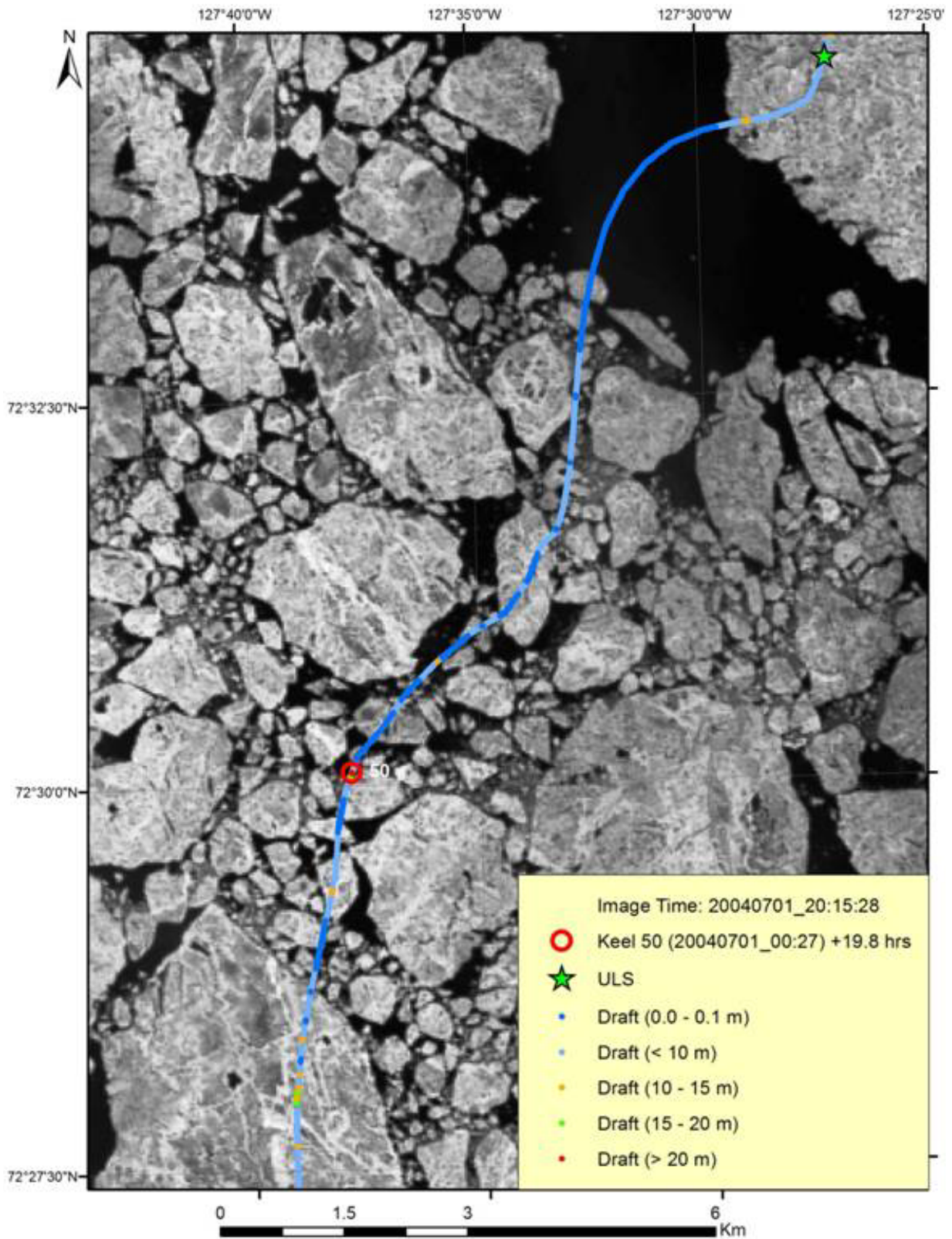


Figure 40. Landsat 7 image (acquisition time 20040701_20:15:28) for Keel 50

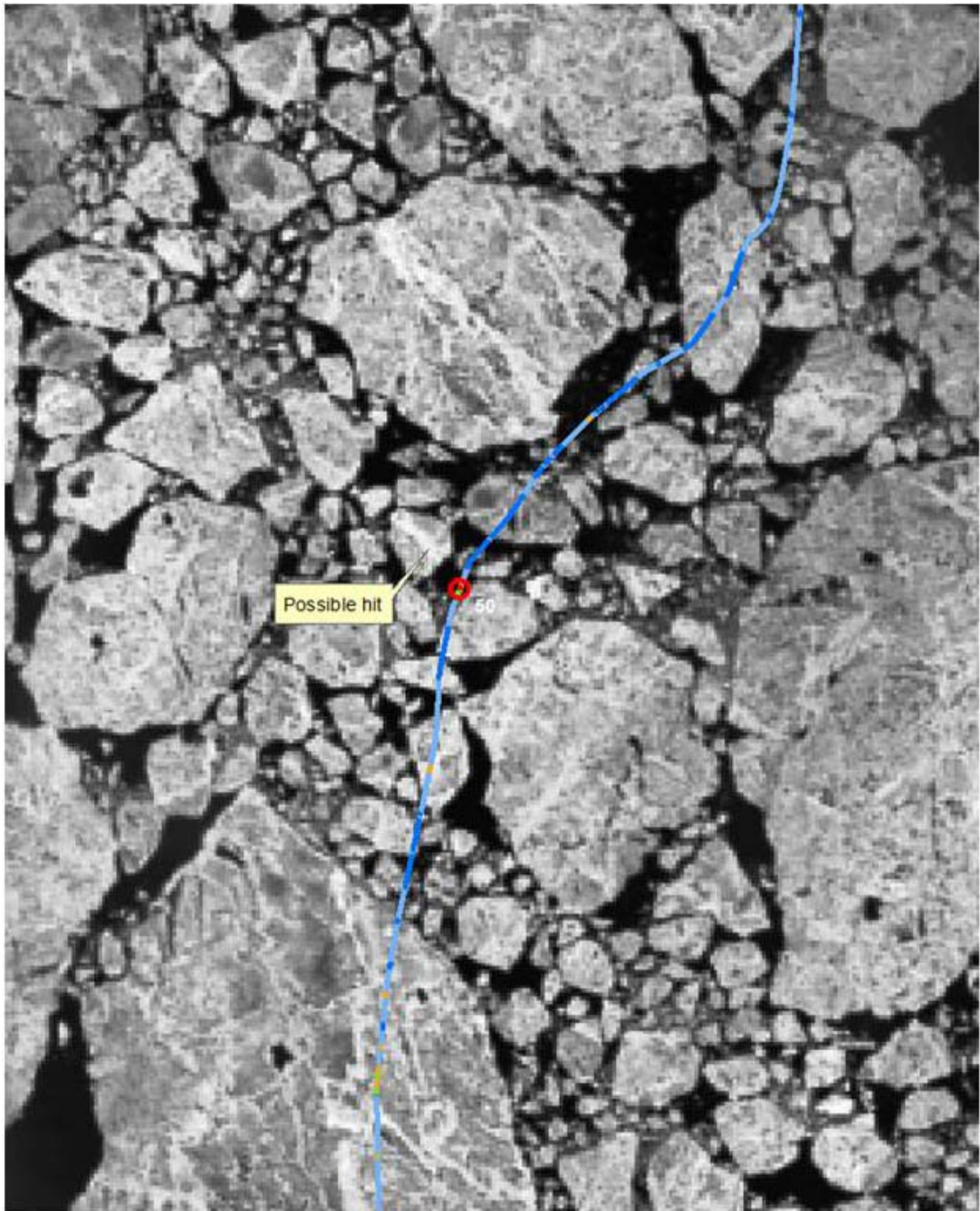


Figure 41. Possible hit for keel 50

4.2.8 Keel 59 to 70 in Landsat 7

Coverage for keels 59 to 70 is provided with a Landsat 7 image acquired in late July. ULS data for between detection and Landsat 7 image are shown in Figure 42 through Figure 53, and the Landsat image is shown in Figure 54 (acquisition time 20040718_20:16:05). The CIS classifies sea ice in the vicinity of the keel locations as predominantly old ice with lesser amounts of first-year thick ice. As with keels 42 - 45 and keel 50, the ice is in an advanced stage of break-up and although loose correlation of ULS data and open water exists, ice floe mobility makes it highly unlikely that correlation of surface features with ULS data can be achieved with any degree of confidence particularly with increased distance from the ULS location.

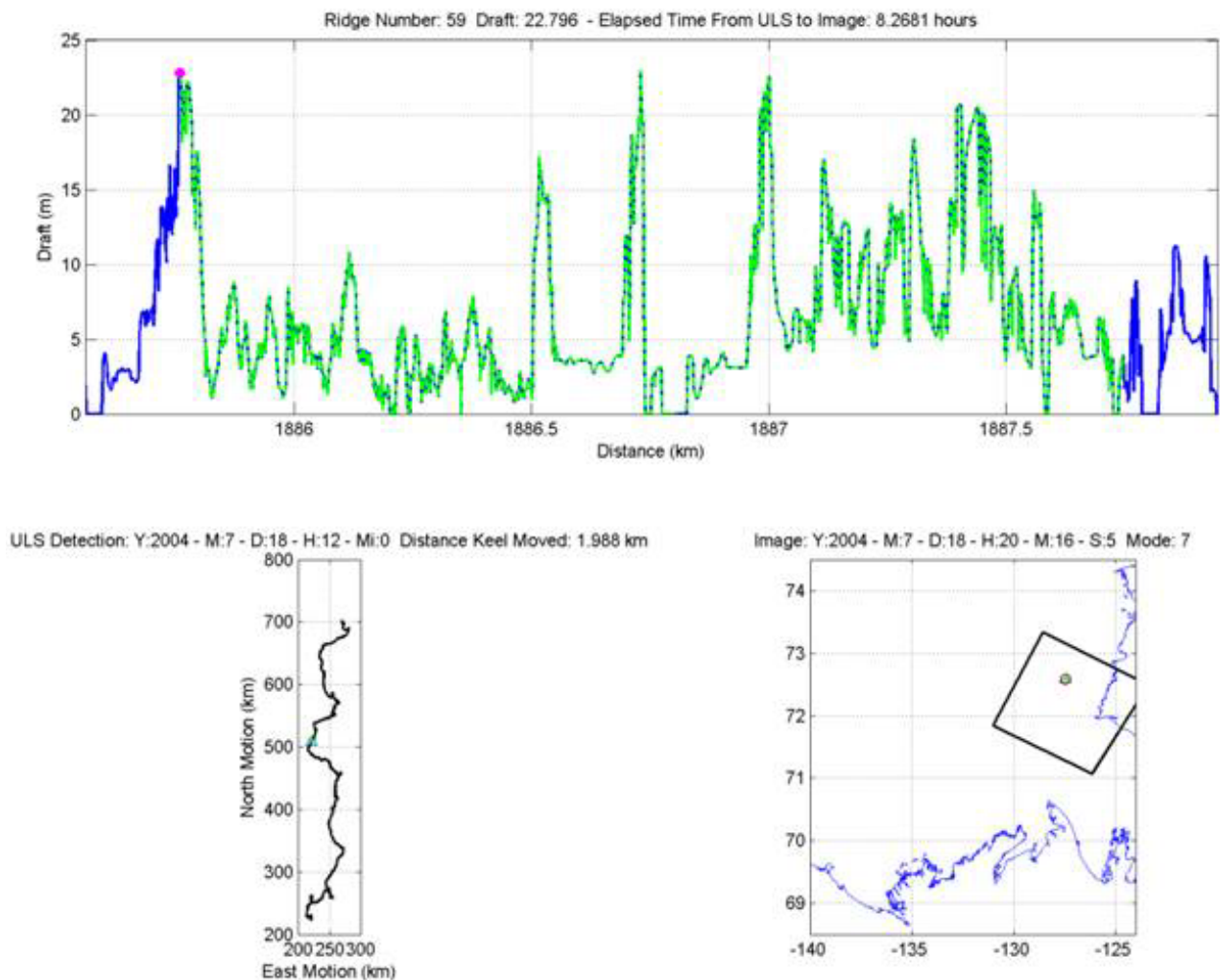
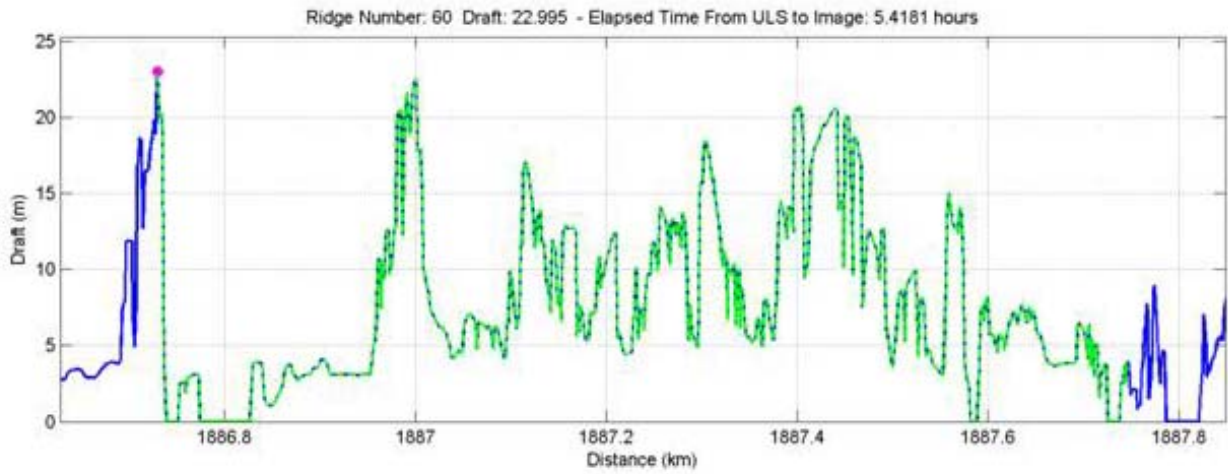


Figure 42. Sea ice draft profile (top), projected drift trajectory (bottom left) and imagery keel location (bottom right) for Keel 59



ULS Detection: Y:2004 - M:7 - D:18 - H:14 - Mi:51 Distance Keel Moved: 1.017 km

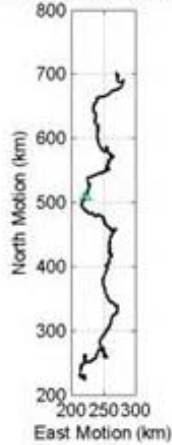


Image: Y:2004 - M:7 - D:18 - H:20 - M:16 - S:5 Mode: 7

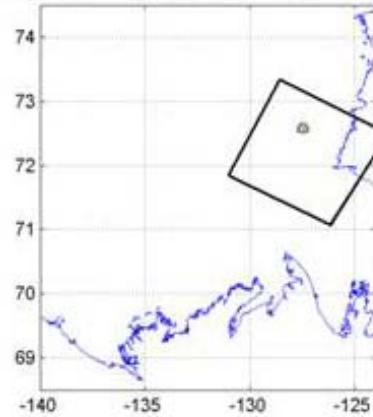
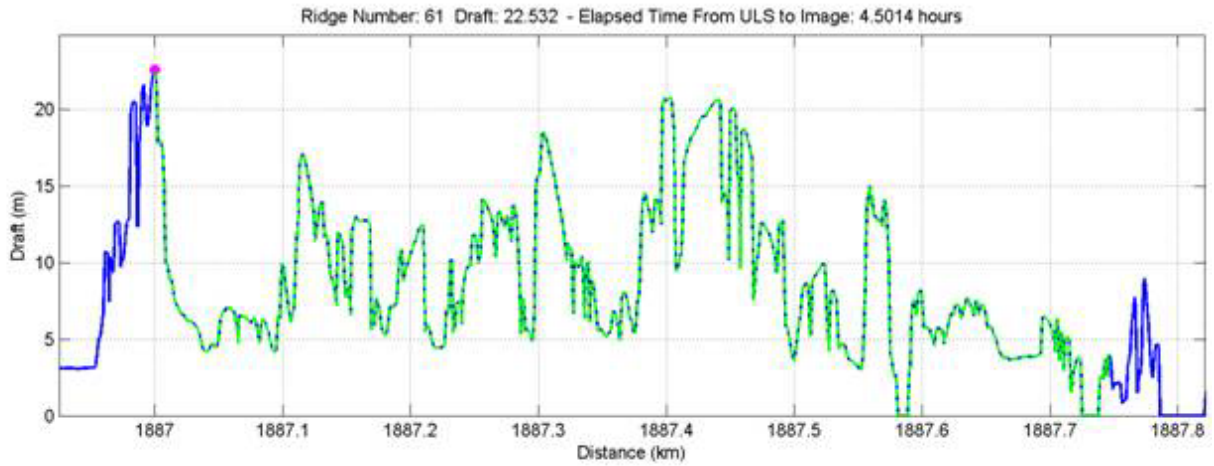


Figure 43. Sea ice draft profile (top), projected drift trajectory (bottom left) and imagery keel location (bottom right) for Keel 60



ULS Detection: Y:2004 - M:7 - D:18 - H:15 - Mi:46 Distance Keel Moved: 0.747 km

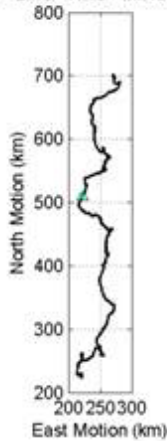


Image: Y:2004 - M:7 - D:18 - H:20 - M:16 - S:5 Mode: 7

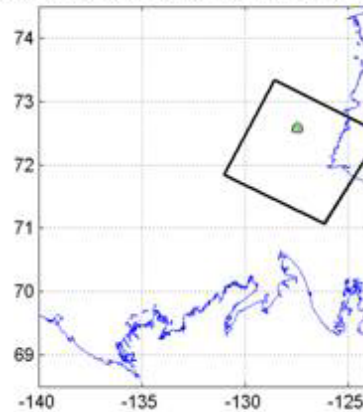
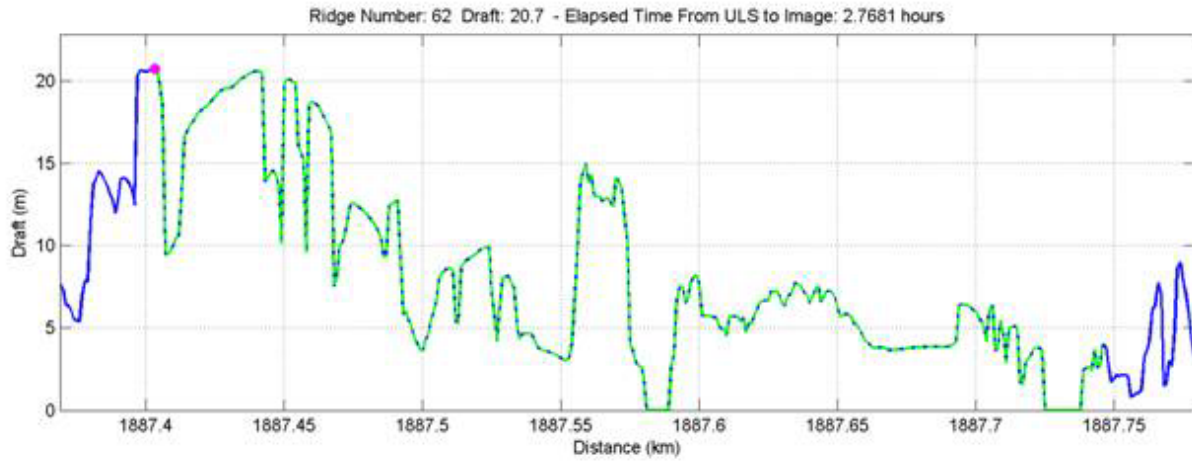


Figure 44. Sea ice draft profile (top), projected drift trajectory (bottom left) and imagery keel location (bottom right) for Keel 61



ULS Detection: Y:2004 - M:7 - D:18 - H:17 - Mi:30 Distance Keel Moved: 0.342 km

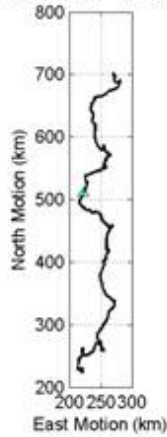


Image: Y:2004 - M:7 - D:18 - H:20 - M:16 - S:5 Mode: 7

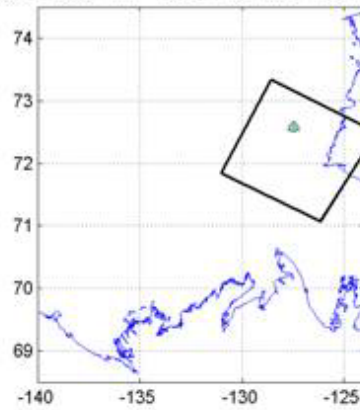
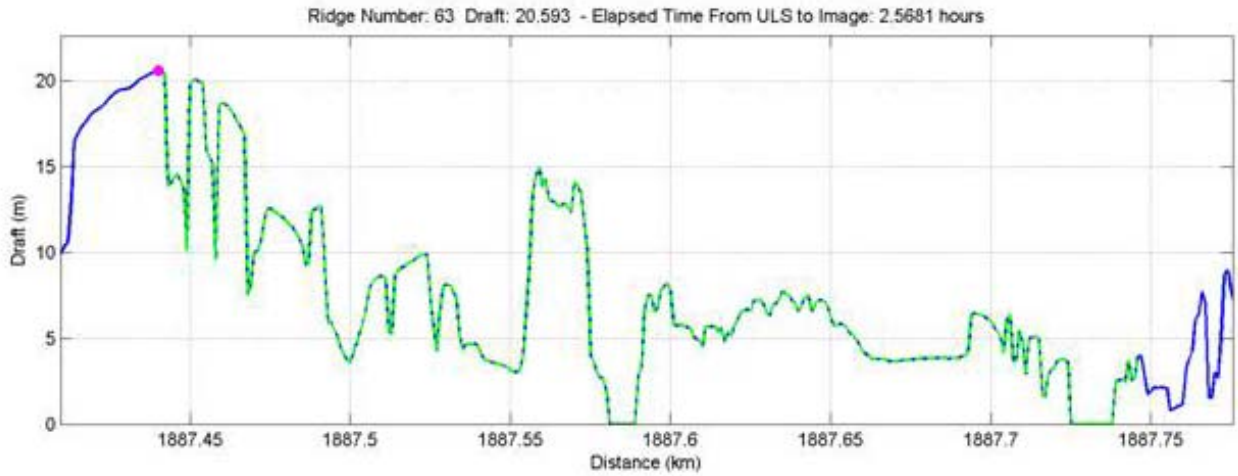


Figure 45. Sea ice draft profile (top), projected drift trajectory (bottom left) and imagery keel location (bottom right) for Keel 62



ULS Detection: Y:2004 - M:7 - D:18 - H:17 - Mi:42 Distance Keel Moved: 0.305 km

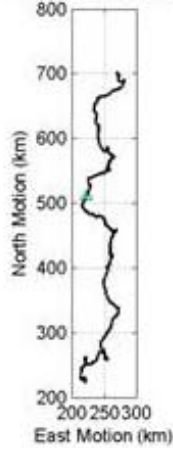


Image: Y:2004 - M:7 - D:18 - H:20 - M:16 - S:5 Mode: 7

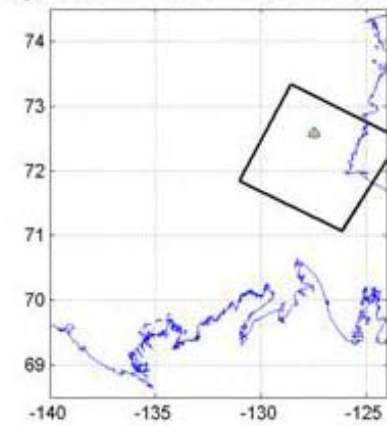
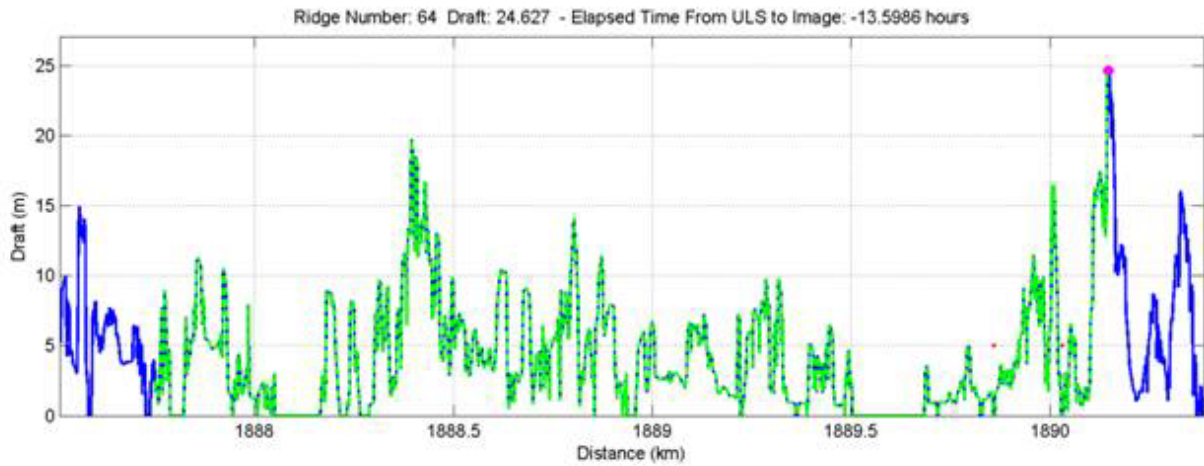


Figure 46. Sea ice draft profile (top), projected drift trajectory (bottom left) and imagery keel location (bottom right) for Keel 63



ULS Detection: Y:2004 - M:7 - D:19 - H:9 - Mi:52 Distance Keel Moved: 2.399 km

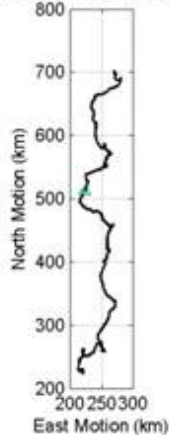


Image: Y:2004 - M:7 - D:18 - H:20 - M:16 - S:5 Mode: 7

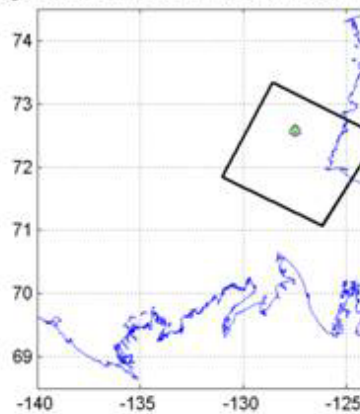


Figure 47. Sea ice draft profile (top), projected drift trajectory (bottom left) and imagery keel location (bottom right) for Keel 64

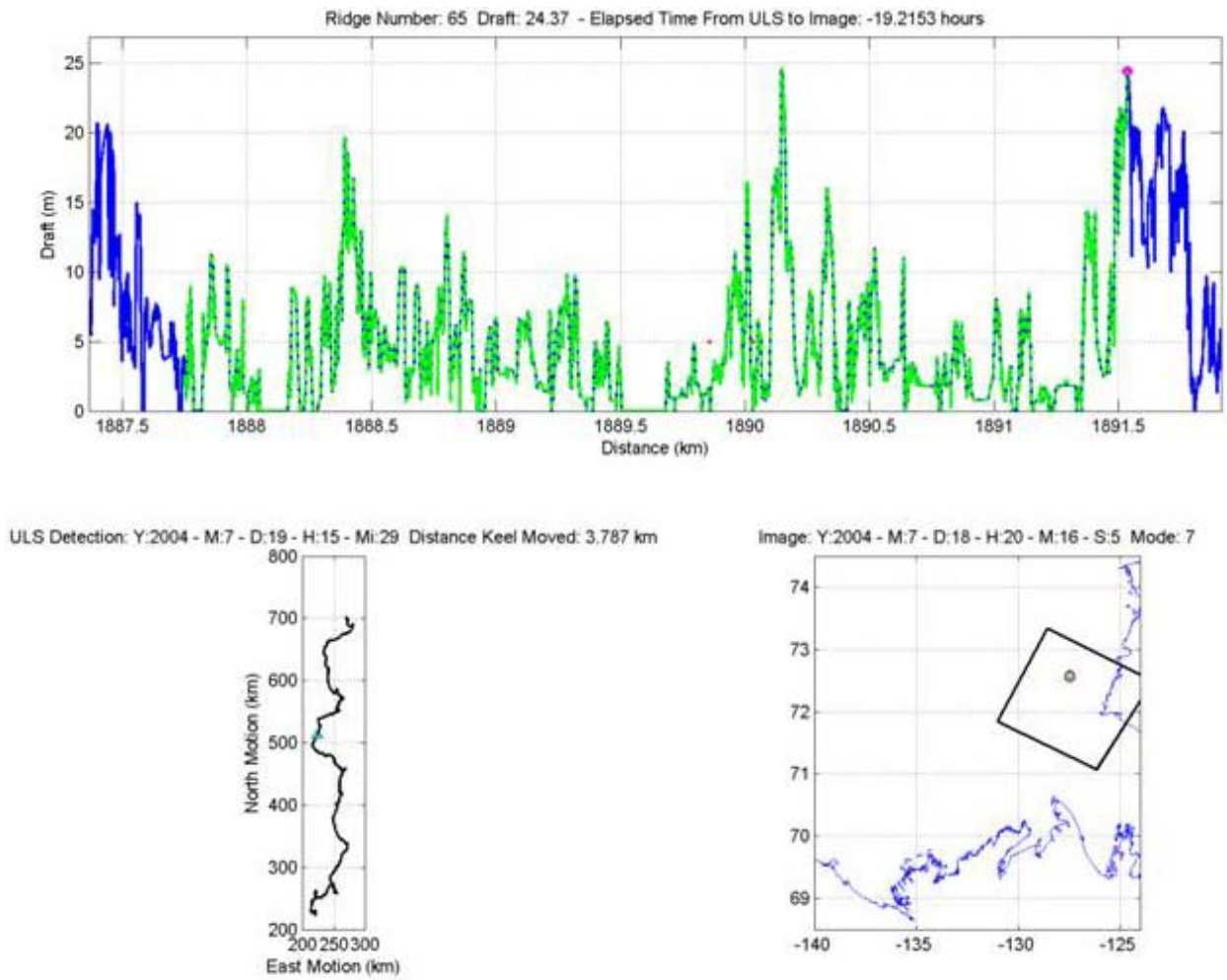
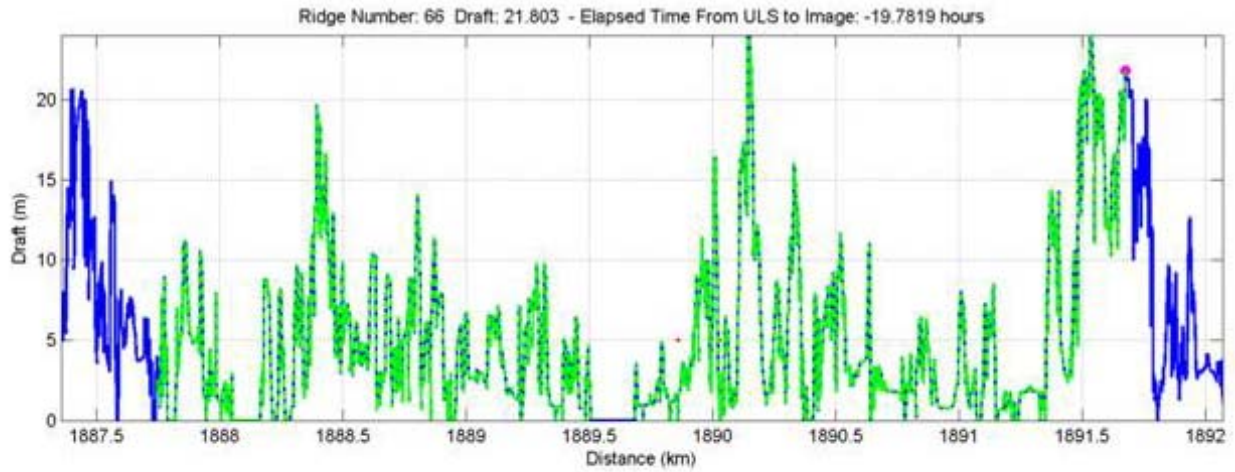


Figure 48. Sea ice draft profile (top), projected drift trajectory (bottom left) and imagery keel location (bottom right) for Keel 65



ULS Detection: Y:2004 - M:7 - D:19 - H:16 - Mi:3 Distance Keel Moved: 3.928 km

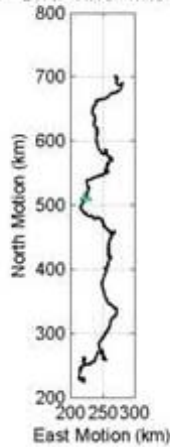


Image: Y:2004 - M:7 - D:18 - H:20 - M:16 - S:5 Mode: 7

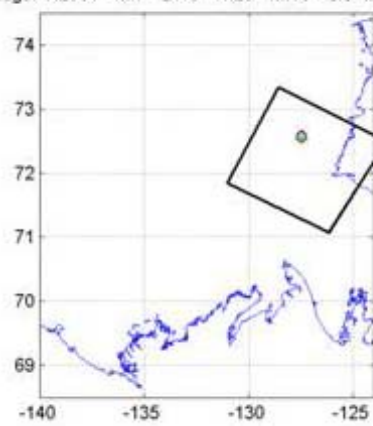
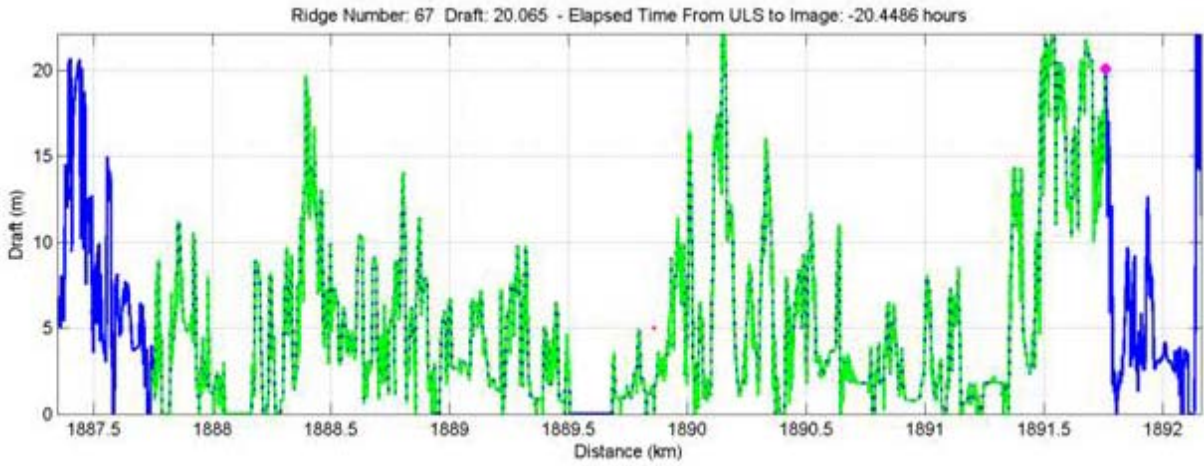


Figure 49. Sea ice draft profile (top), projected drift trajectory (bottom left) and imagery keel location (bottom right) for Keel 66



ULS Detection: Y:2004 - M:7 - D:19 - H:16 - Mi:43 Distance Keel Moved: 4.011 km

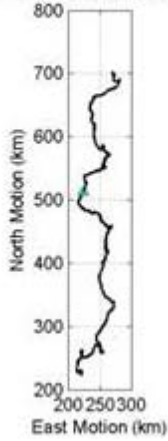


Image: Y:2004 - M:7 - D:18 - H:20 - M:16 - S:5 Mode: 7

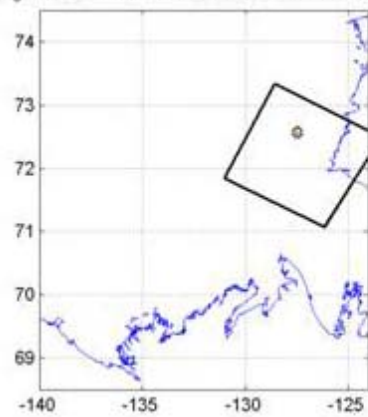
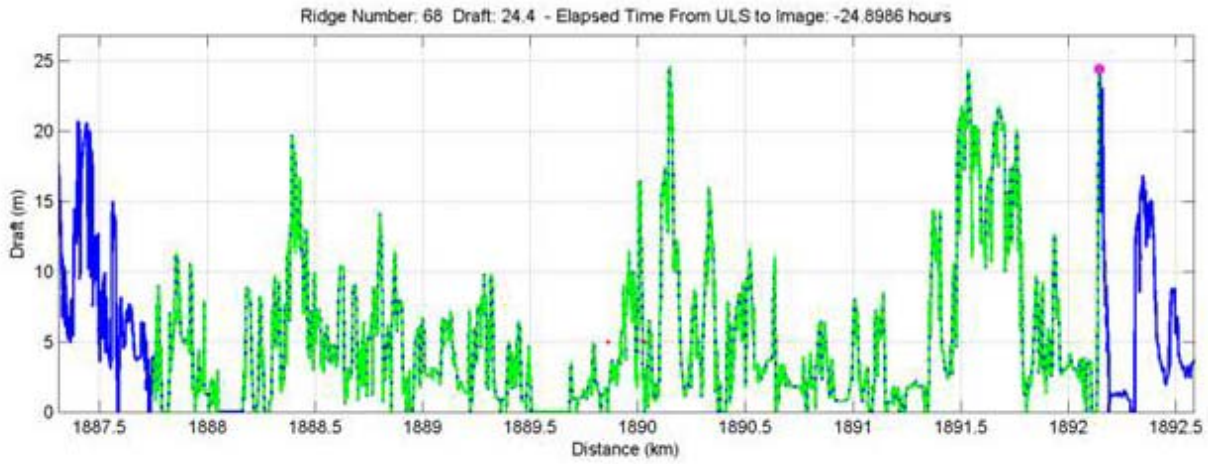


Figure 50. Sea ice draft profile (top), projected drift trajectory (bottom left) and imagery keel location (bottom right) for Keel 67



ULS Detection: Y:2004 - M:7 - D:19 - H:21 - Mi:10 Distance Keel Moved: 4.398 km

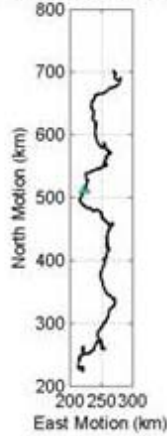


Image: Y:2004 - M:7 - D:18 - H:20 - M:16 - S:5 Mode: 7

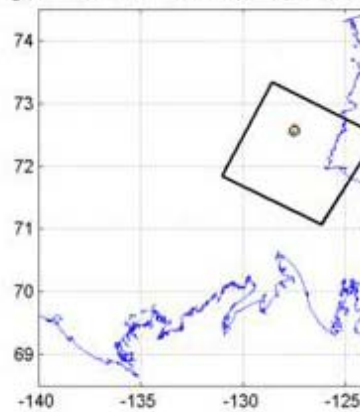
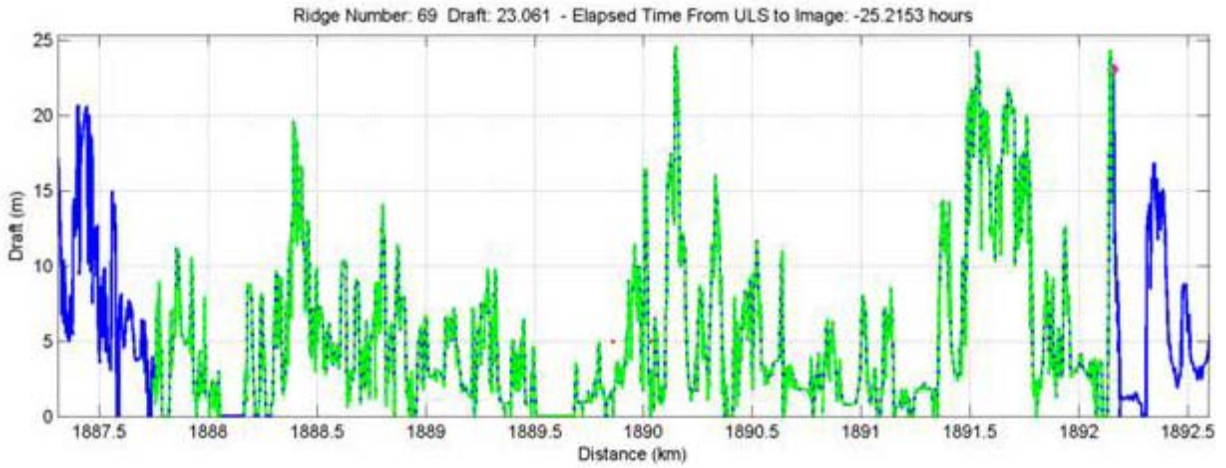


Figure 51. Sea ice draft profile (top), projected drift trajectory (bottom left) and imagery keel location (bottom right) for Keel 68



ULS Detection: Y:2004 - M:7 - D:19 - H:21 - Mi:29 Distance Keel Moved: 4.408 km

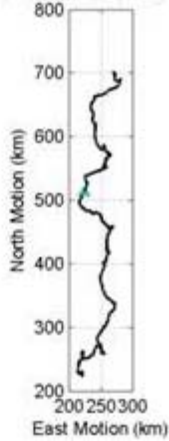


Image: Y:2004 - M:7 - D:18 - H:20 - M:16 - S:5 Mode: 7

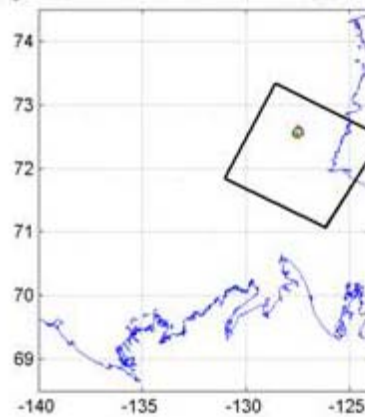
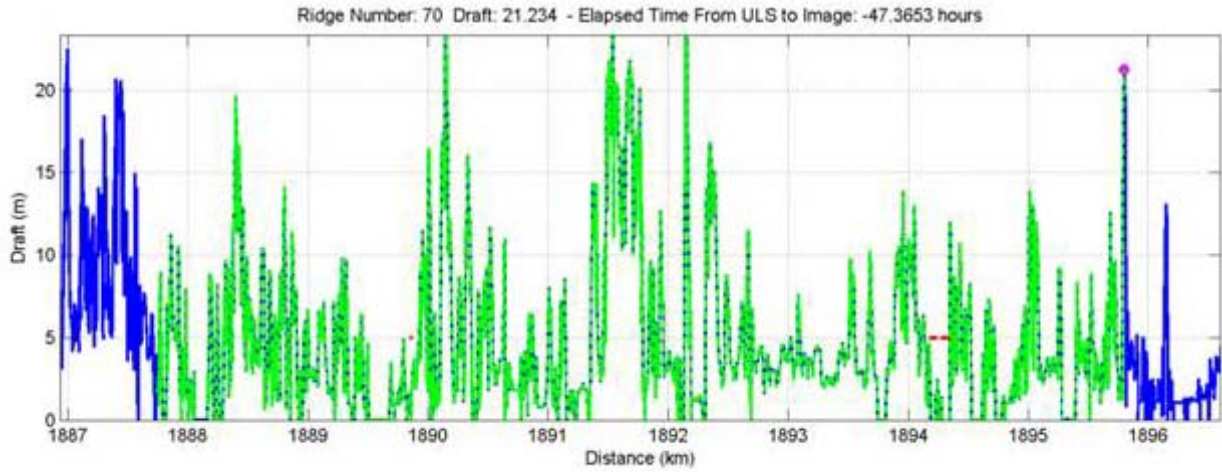


Figure 52. Sea ice draft profile (top), projected drift trajectory (bottom left) and imagery keel location (bottom right) for Keel 69



ULS Detection: Y:2004 - M:7 - D:20 - H:19 - Mi:38 Distance Keel Moved: 8.05 km

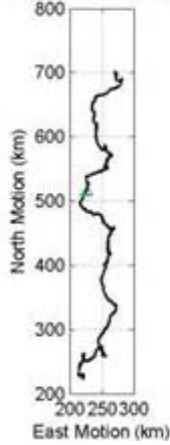


Image: Y:2004 - M:7 - D:18 - H:20 - M:16 - S:5 Mode: 7

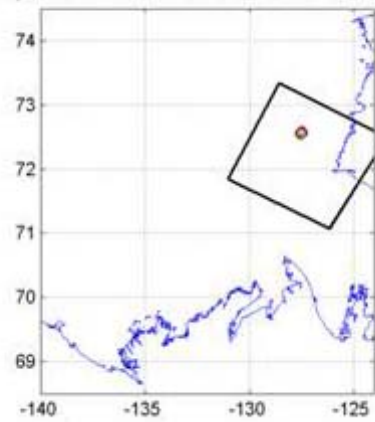


Figure 53. Sea ice draft profile (top), projected drift trajectory (bottom left) and imagery keel location (bottom right) for Keel 70

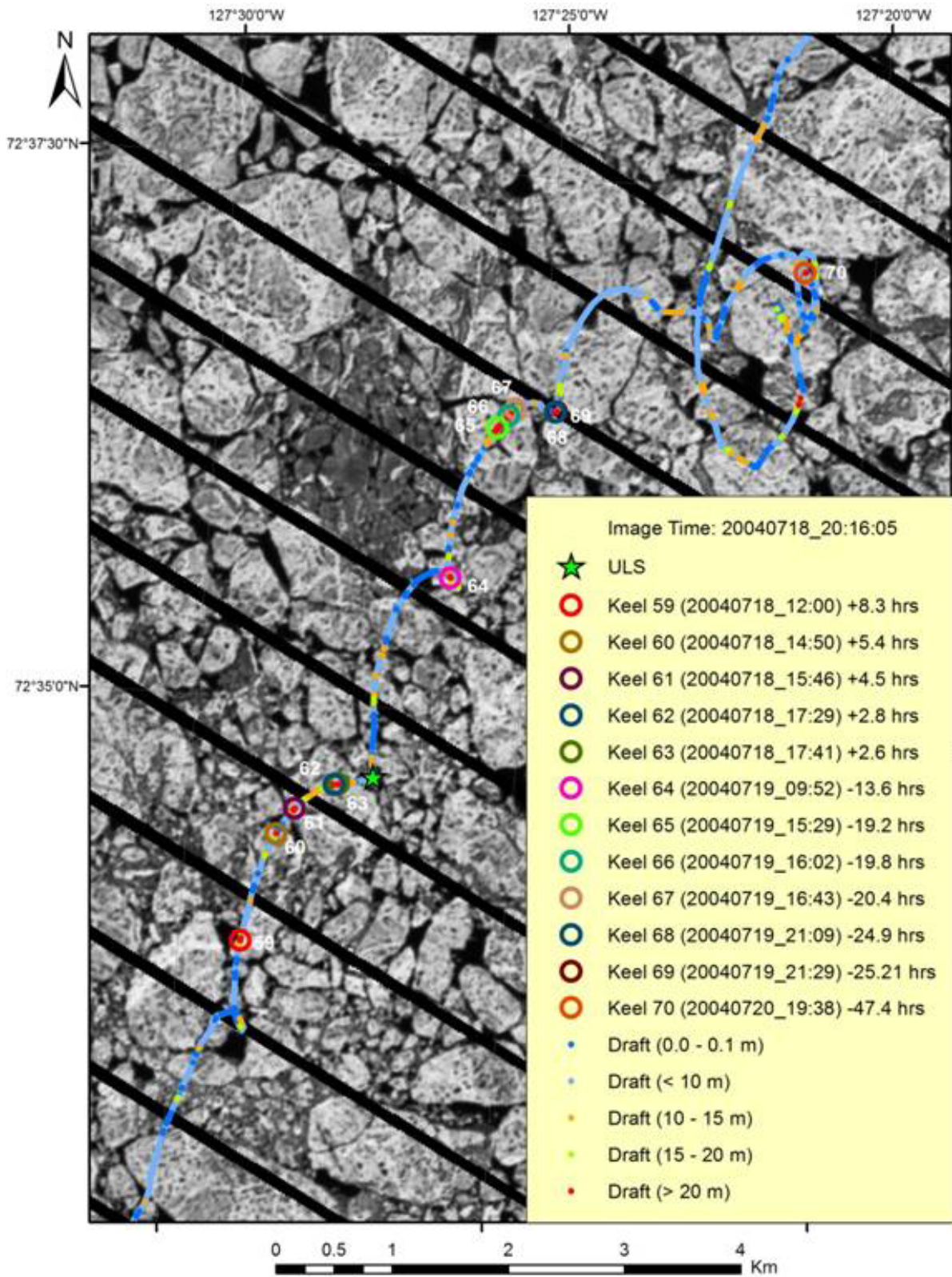


Figure 54. Landsat 7 image (acquisition time 20040718_20:16:05) for Keels 59 through 70

4.2.9 Keel 74 in Envisat

Coverage for keel 74 is provided with two Envisat WS images acquired in late July. The CIS classifies sea ice at the site of keel 74 as predominantly old ice with lesser amounts of first-year thick ice. ULS data collected between keel detection and the first image acquisition (20040728_19:44:43) is shown in Figure 55, with the Envisat image shown in Figure 56. Likewise, ULS data collected between keel detection and the second image acquisition (20040729_19:13:57) is shown in Figure 57, with the Envisat image shown in Figure 58. The coarse resolution (150 m) renders this data type unsuitable for detecting surface features (unless very large, such as rubble fields) with any degree of confidence.

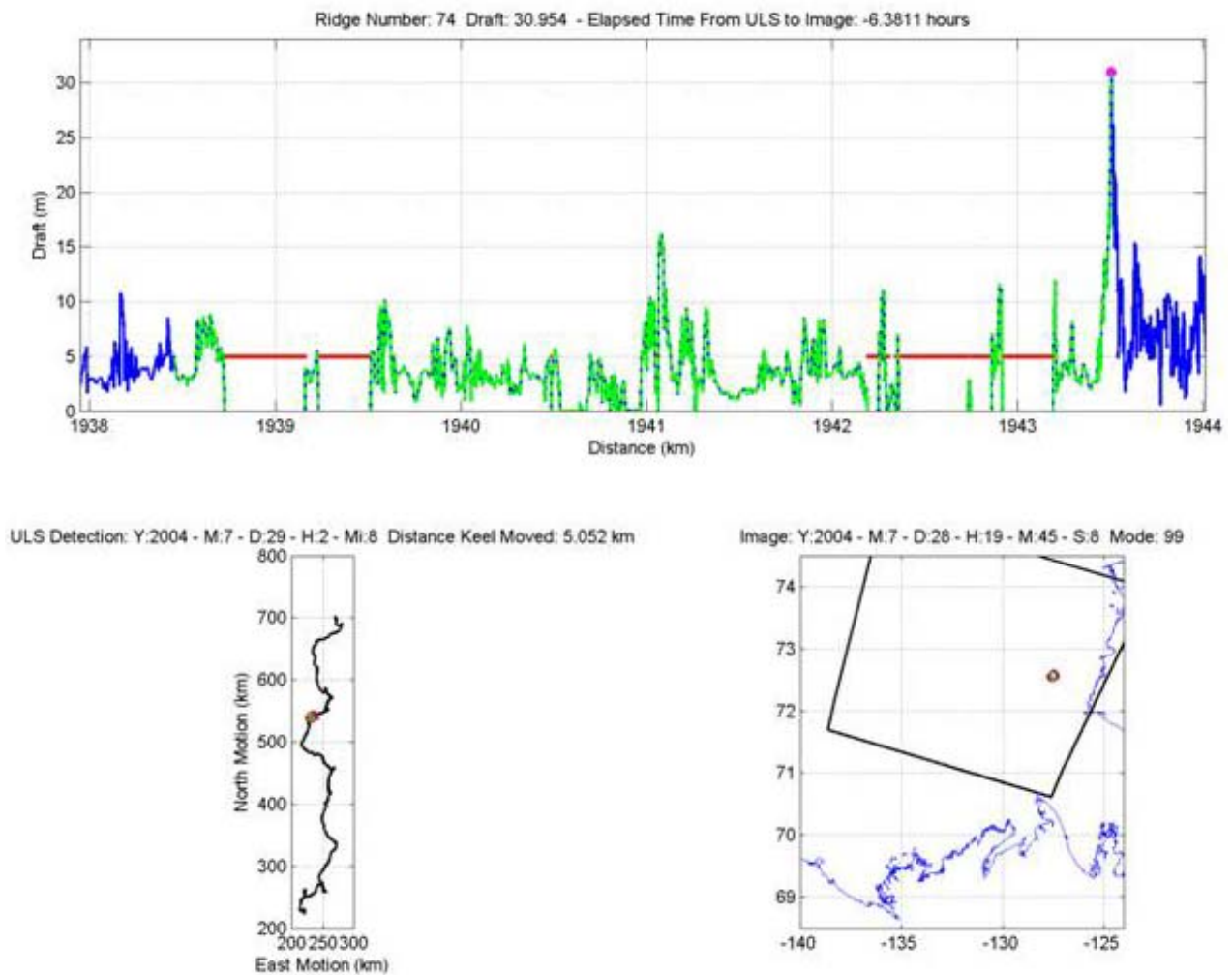


Figure 55. Sea ice draft profile (top), projected drift trajectory (bottom left) and imagery keel location (bottom right) for Keel 74 for Envisat WS image acquisition 20040728_19:44:43

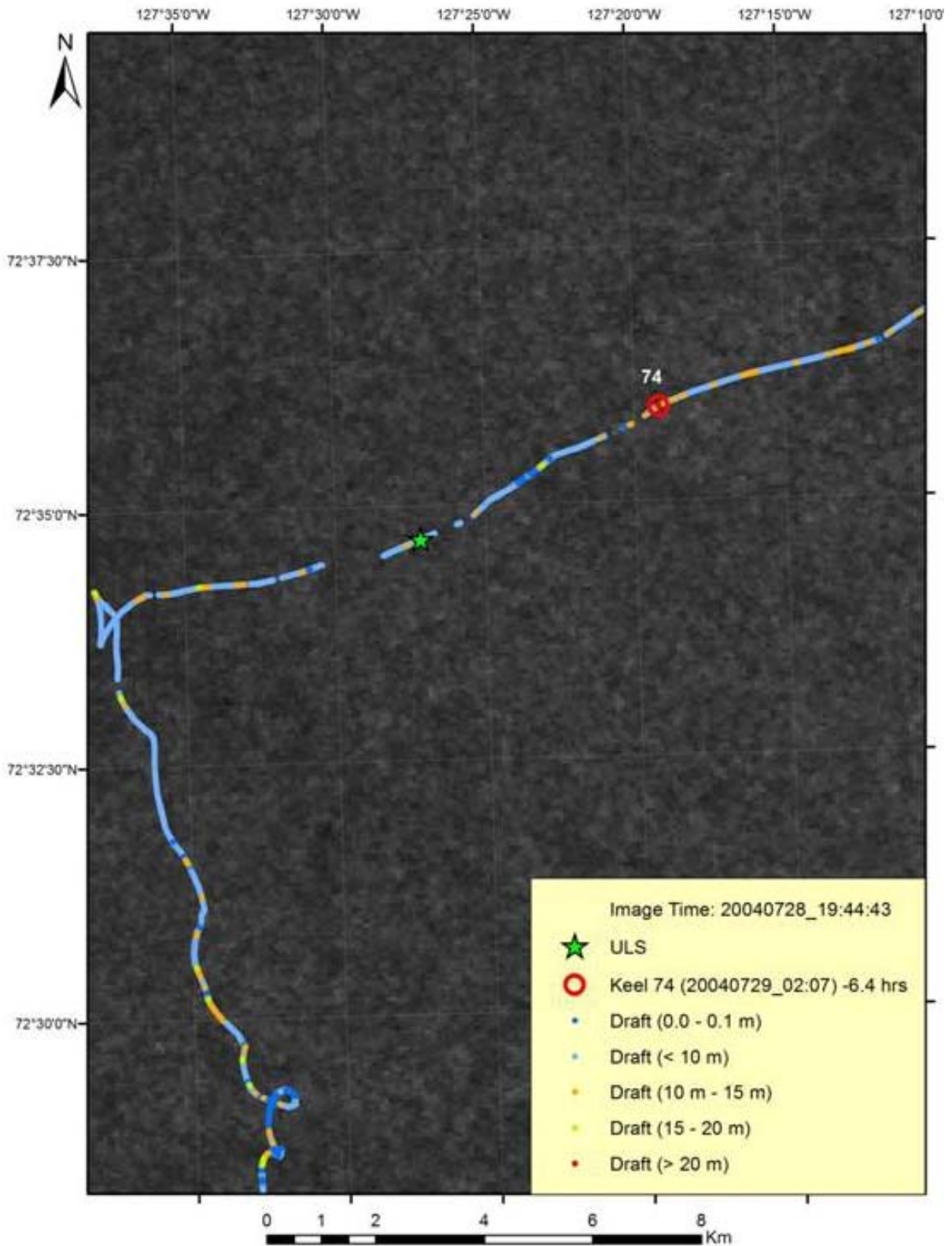


Figure 56. Envisat WS image (acquisition time 20040728_19:44:43) for Keel 74

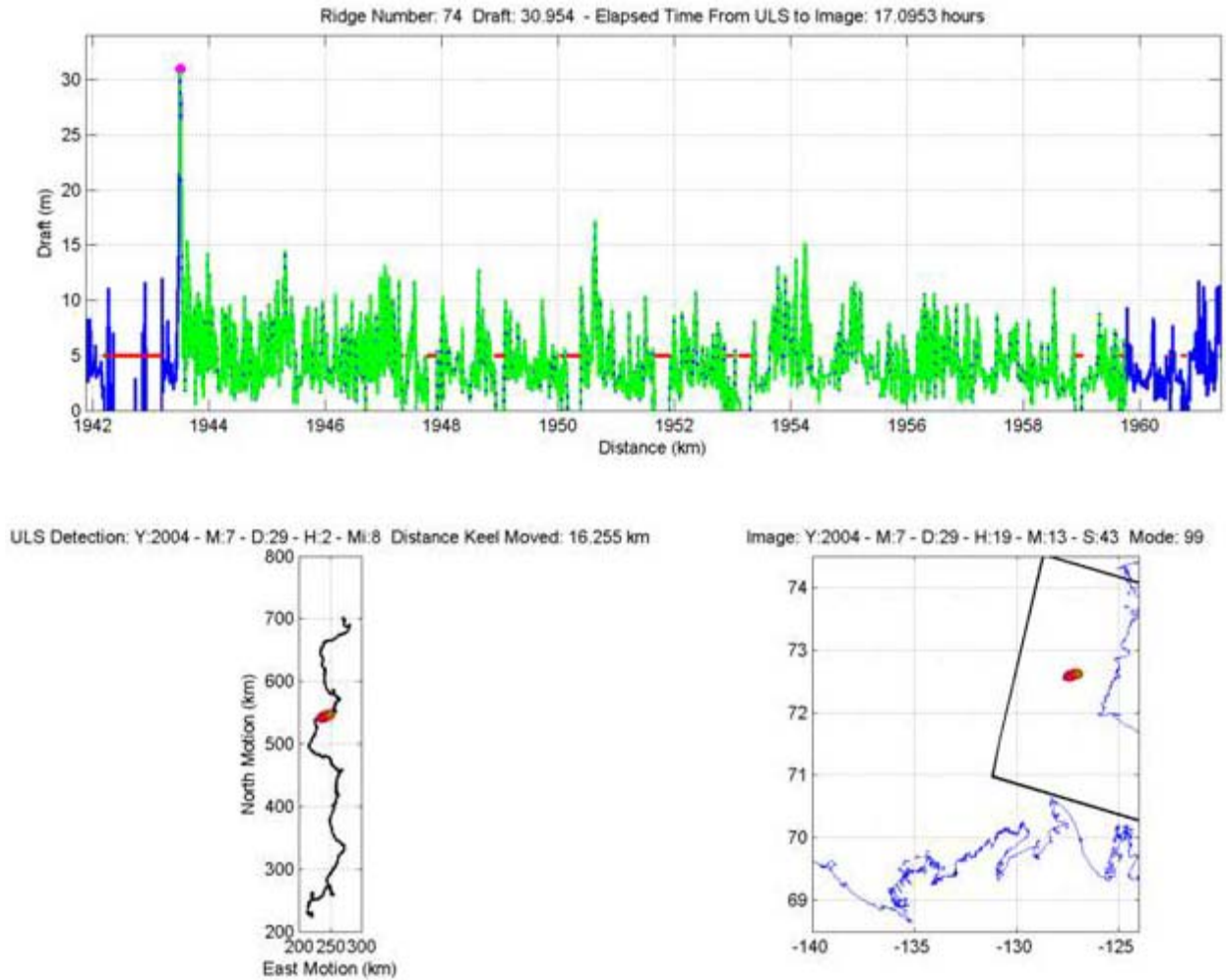


Figure 57. Sea ice draft profile (top), projected drift trajectory (bottom left) and imagery keel location (bottom right) for Keel 74 for Envisat WS image acquisition 20040729_19:13:57

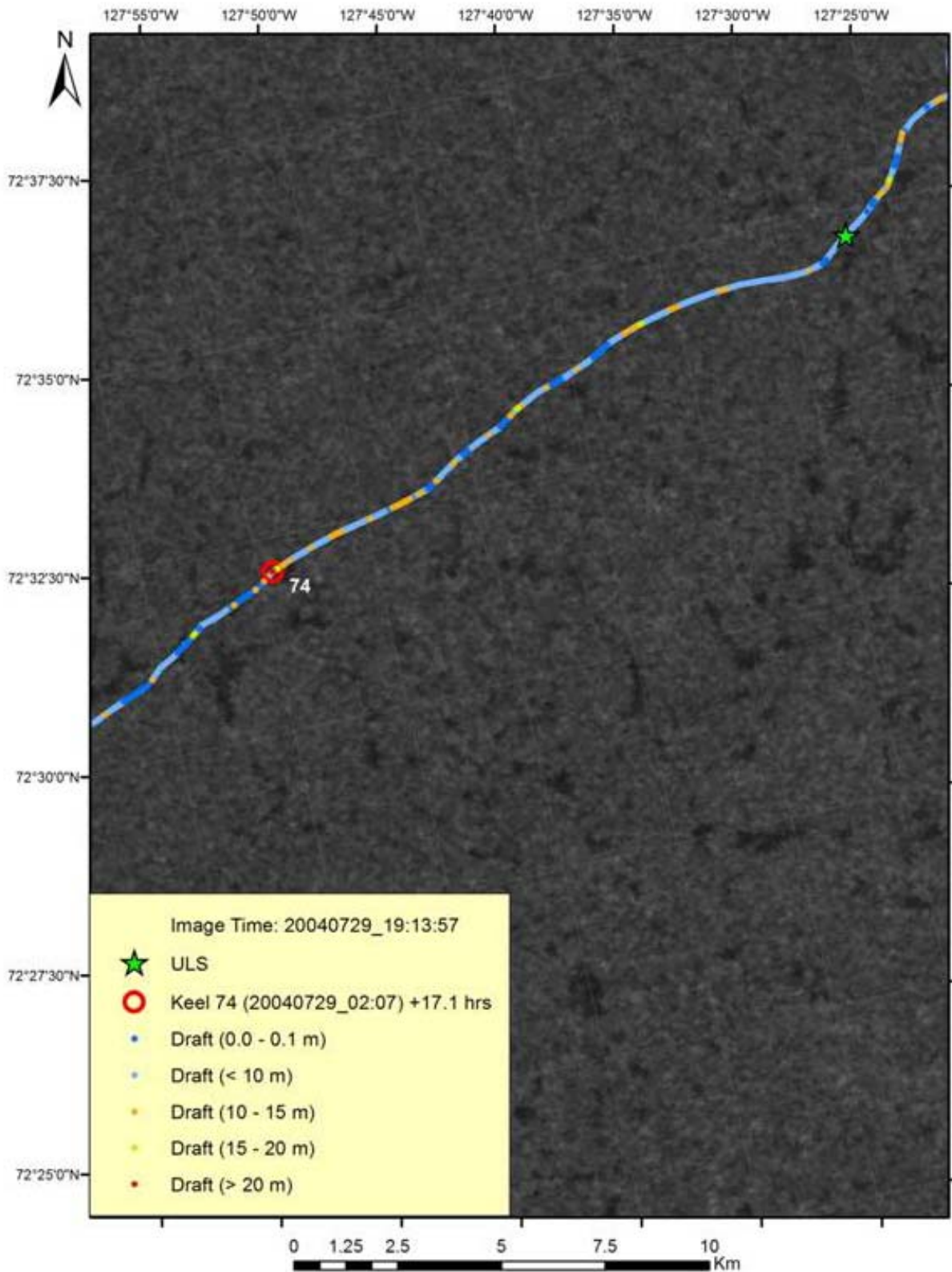


Figure 58. Envisat WS image (acquisition time 20040729_19:13:57) for Keel 74

4.2.10 Keel 85 in Envisat

Coverage for keel 85 is provided with an Envisat WS image acquired in February, 2005. ULS data collected between the time of keel detection and image acquisition is shown in Figure 59. The CIS classifies sea ice at the site of keel 85 as predominantly old ice with lesser amounts of first-year thick ice. Although mentioned previously, this data type is not considered ideal for detecting surface features due to its coarse resolution (150 m), Figure 60 and Figure 61 show a good correlation of ULS data and possible hit at the keel site and two locations with drafts greater than 20 m close to the ULS. Given the time of year when the ice sheet is assumed to be consolidated (exhibiting limited drift, as opposed to break-up), and the close proximity to the ULS site, implies a high confidence observation.

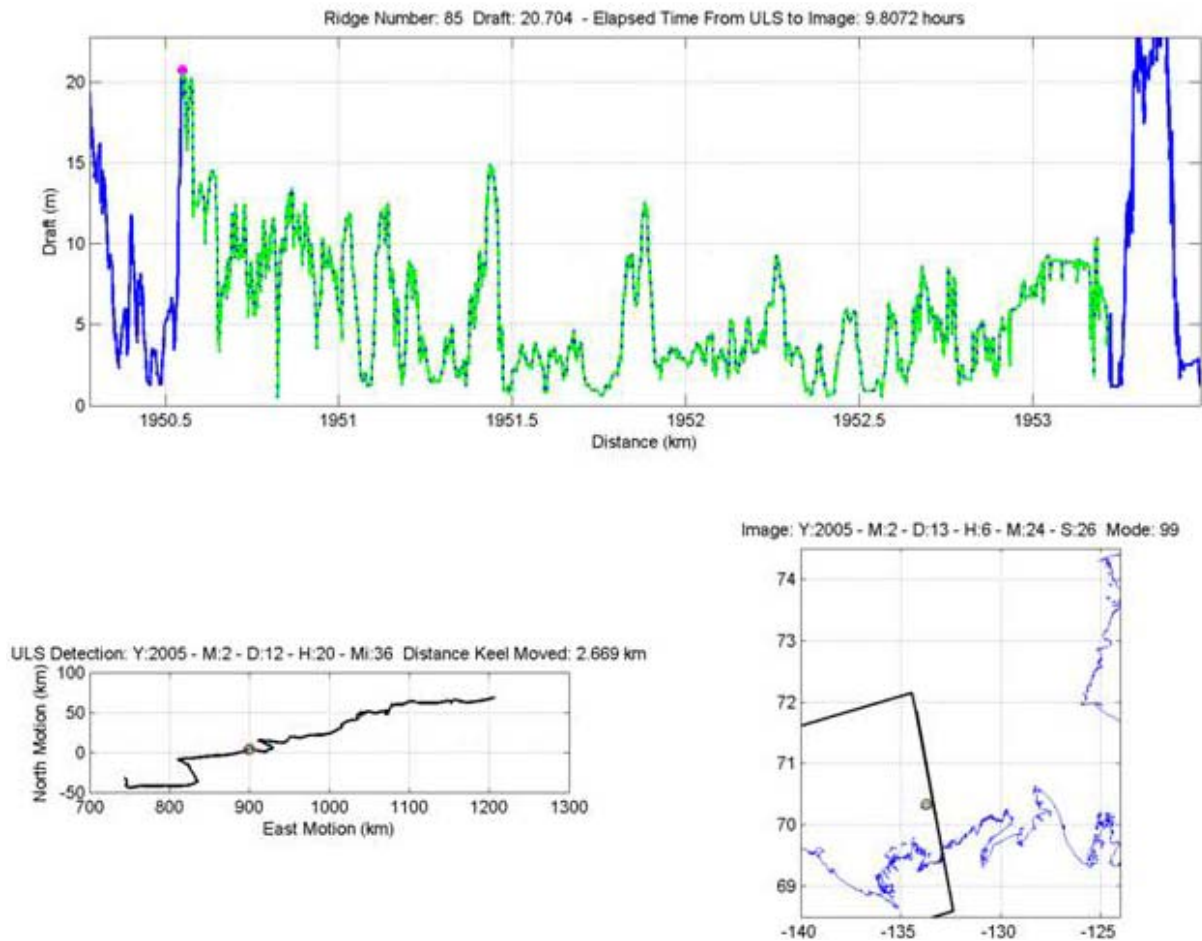


Figure 59. Sea ice draft profile (top), projected drift trajectory (bottom left) and imagery keel location (bottom right) for Keel 85

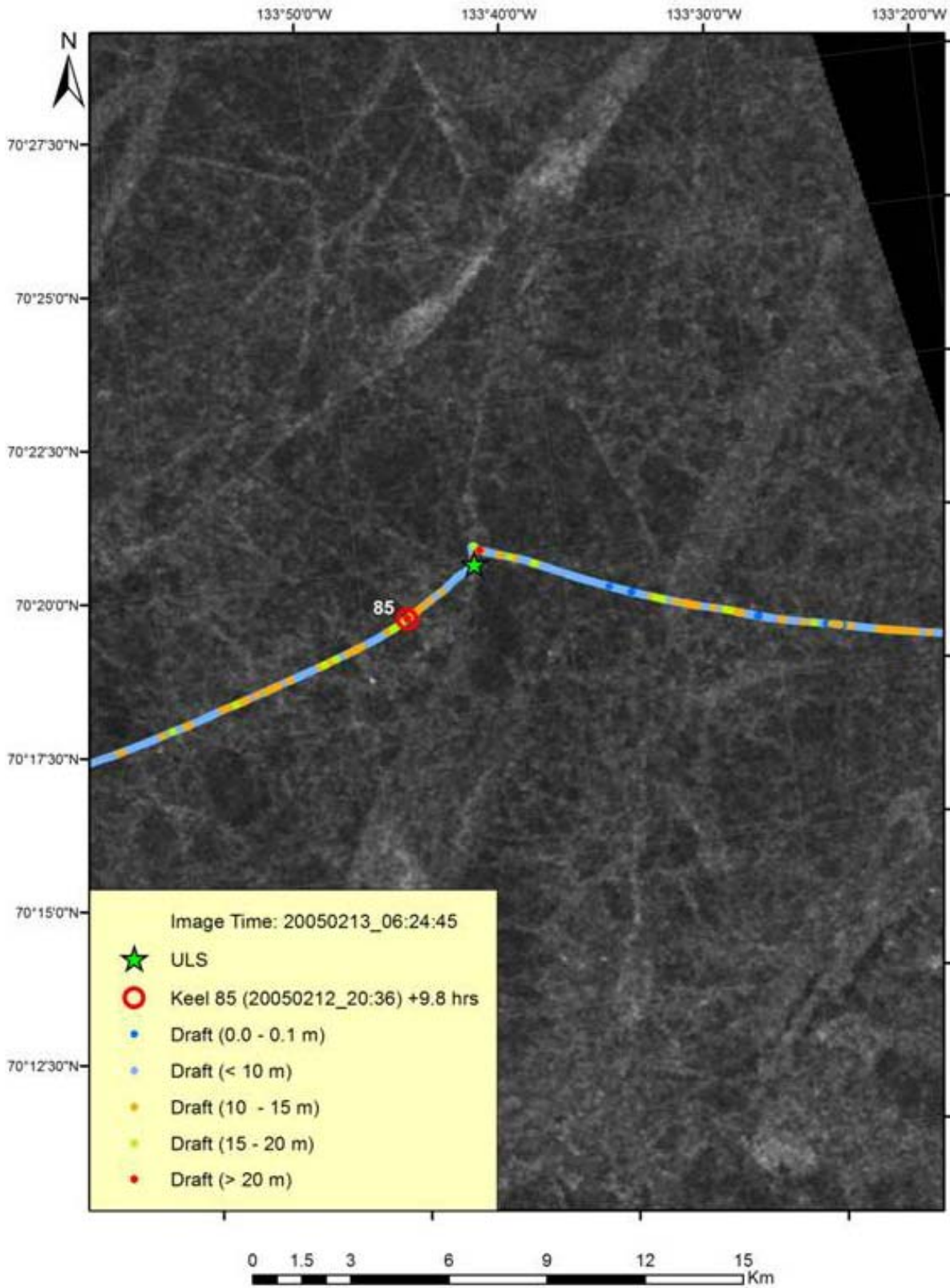


Figure 60. Envisat WS image (acquisition time 20050213_06:24:45) for Keel 85

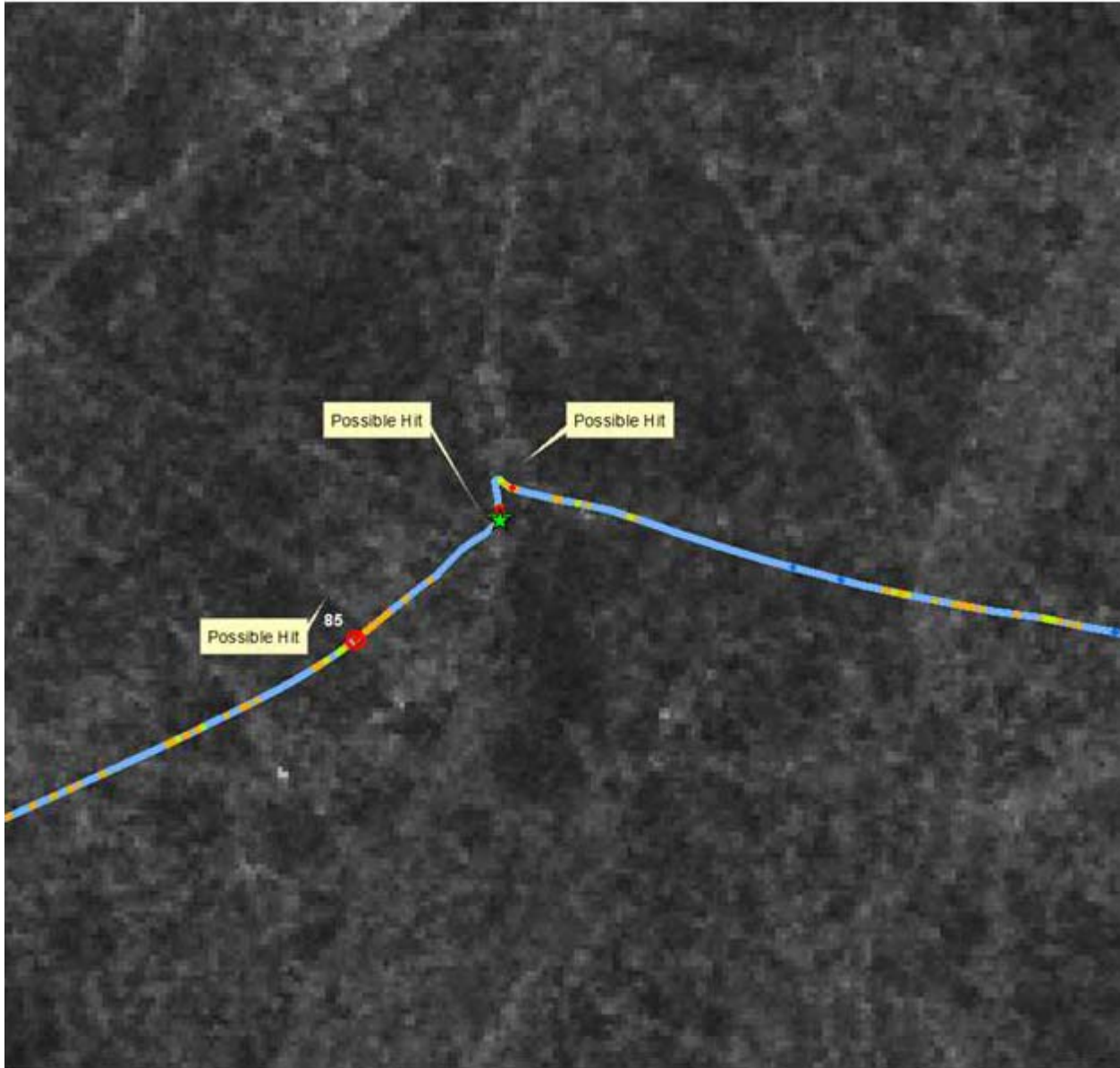


Figure 61. Possible hit for keel 85 and drafts > 20 m near ULS location

4.2.11 Keel 88 in Envisat

Coverage for keel 88 was provided with an Envisat WS images and an Envisat APP image, both acquired in March of 2005. Sea ice at the site of keel 88 is classified by the CIS as predominantly first-year thick with trace amounts of old ice. ULS data collected between keel detection and the first image acquisition (20050314_19:48:27) is shown in Figure 62, with the Envisat WS image shown in Figure 63. Likewise, ULS data collected between keel detection and the second image acquisition (20050315_05:42:02) is shown in Figure 64, with the Envisat APP image shown in Figure 65. Except for open water leads, the coarse resolution (150 m) in the

Envisat WS image shown in Figure 63 impedes identification of features. Although the time difference between image acquisition and the keel location is minimal, there is little evidence of ULS and surface feature correlation. Features in the Envisat APP imagery (25 m resolution) shown in Figure 65, while a little more distinguishable, also exhibit a poor correlation. It is of importance to note the change in position of open water leads close to the ULS and keel locations in both images illustrating the ice dynamics over a short time interval.

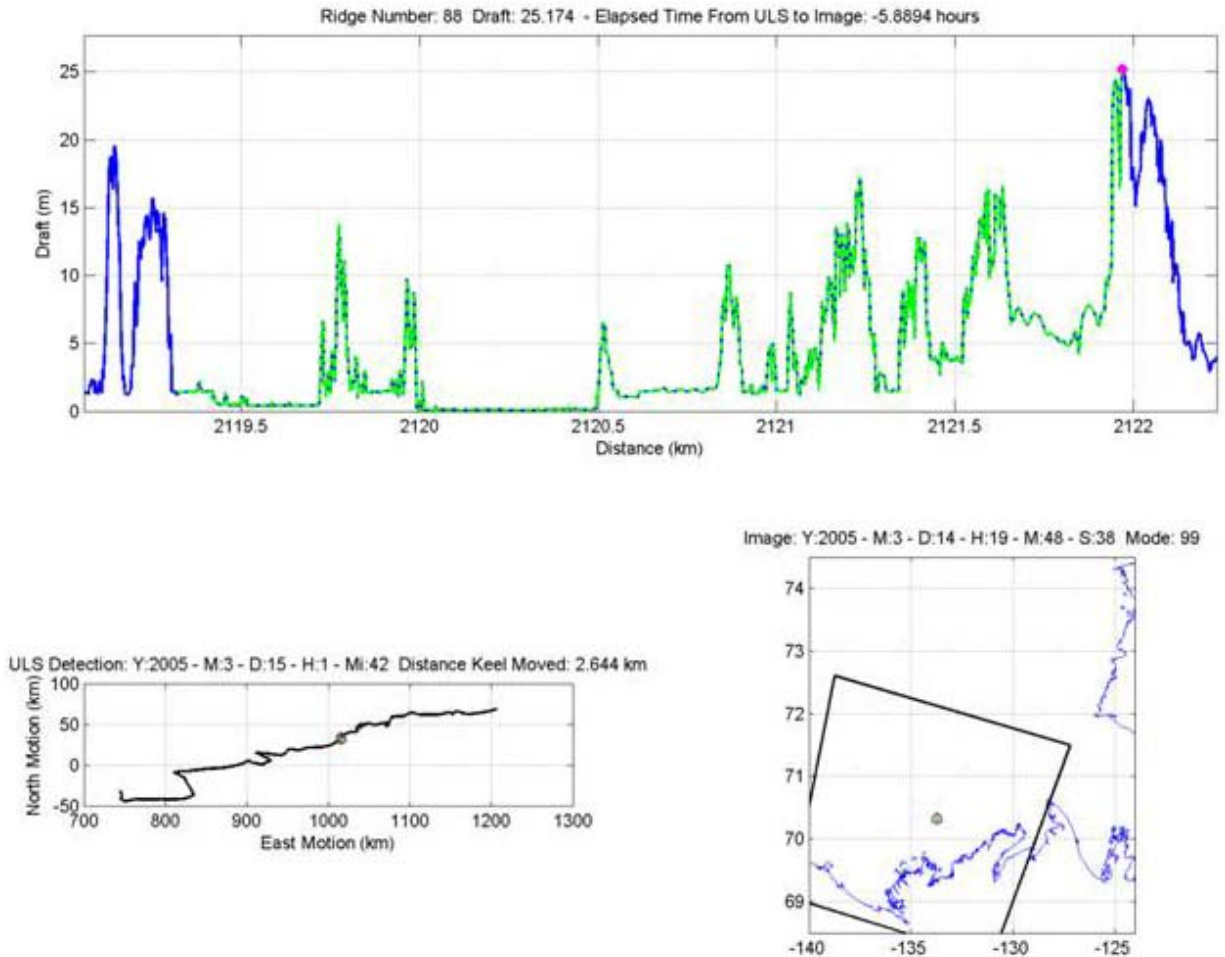


Figure 62. Sea ice draft profile (top), projected drift trajectory (bottom left) and imagery keel location (bottom right) for Keel 88 Envisat WS image acquisition

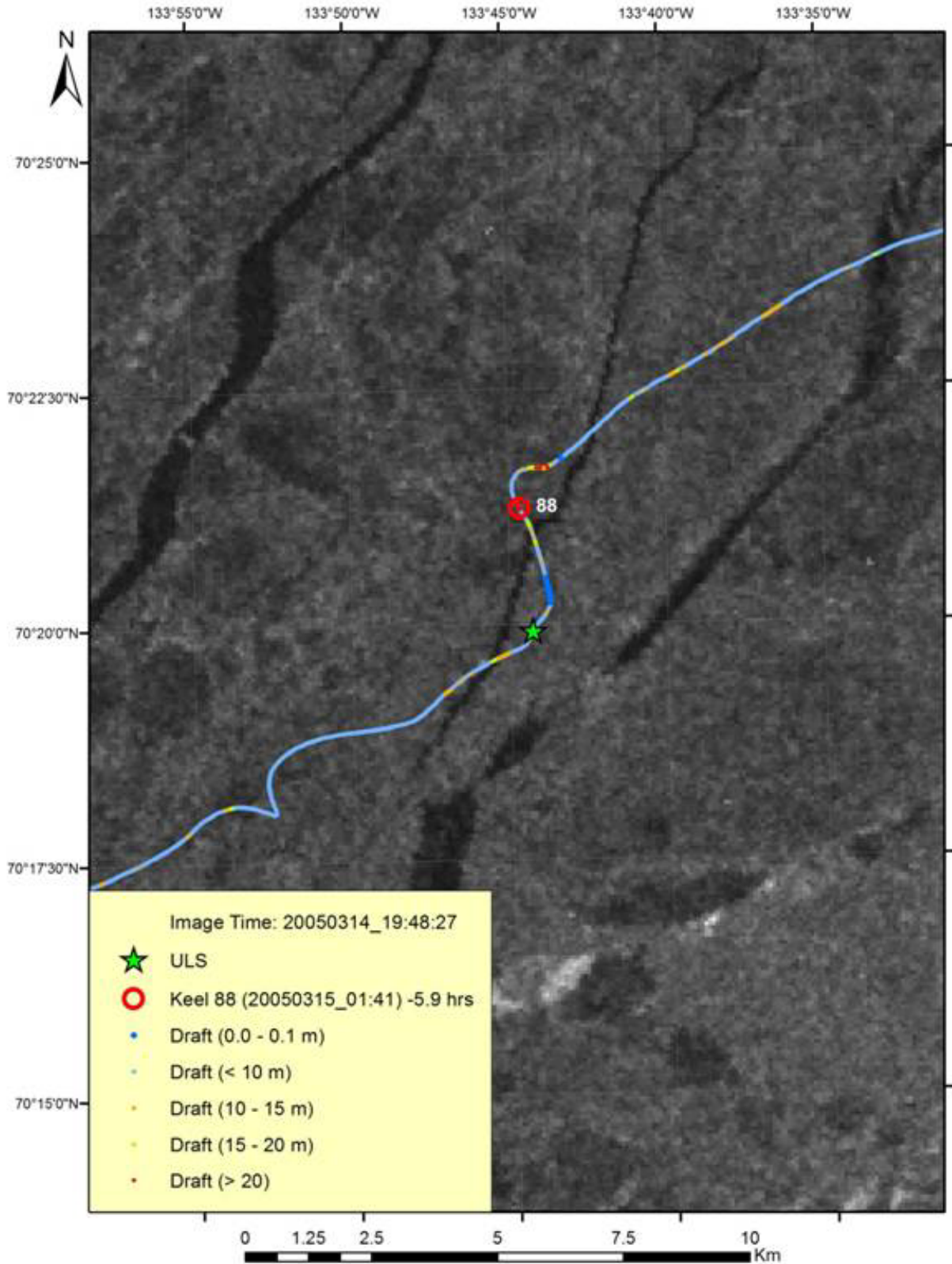


Figure 63. Envisat WS image (acquisition time 20050314_19:48:27) for Keel 88

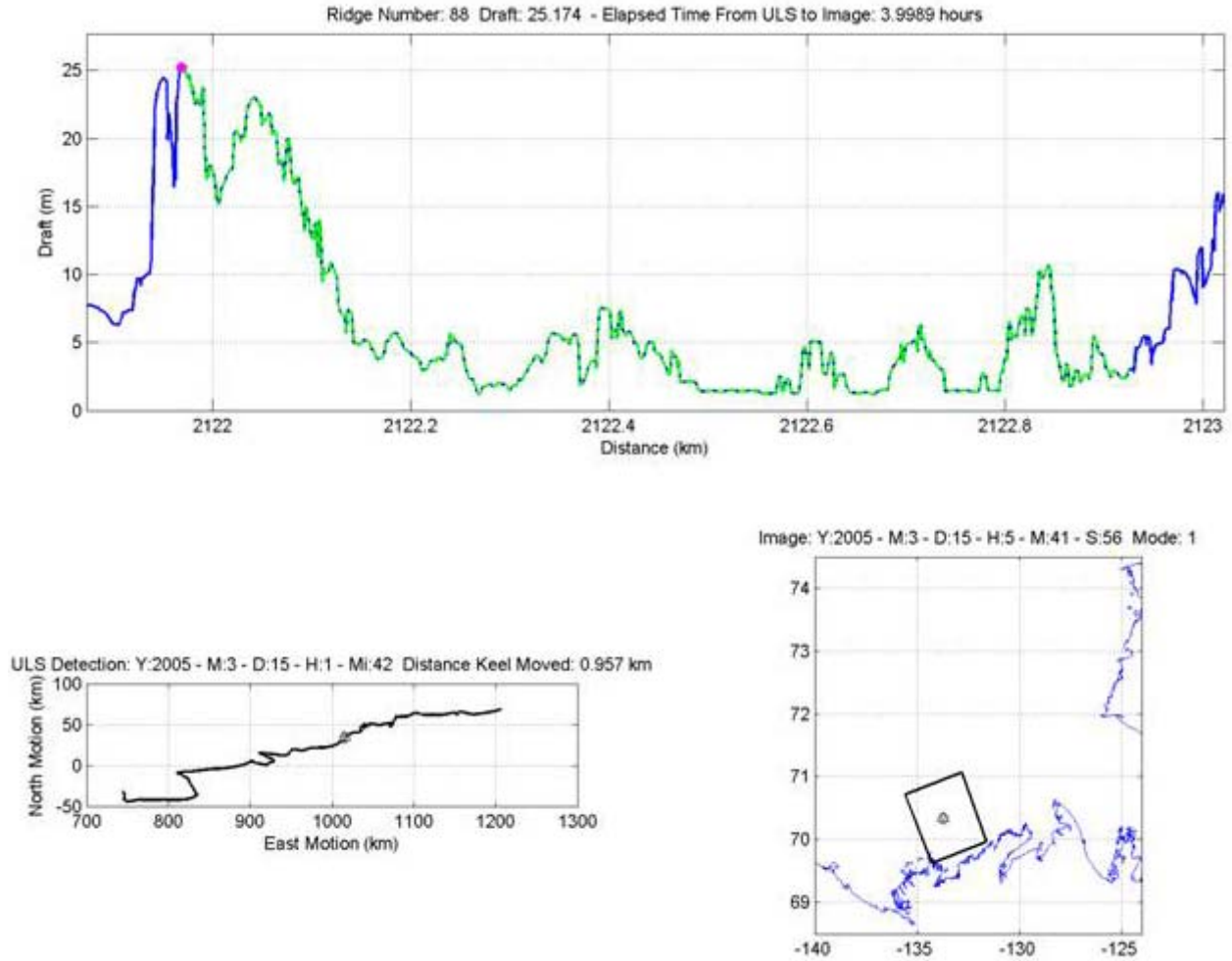


Figure 64. Sea ice draft profile (top), projected drift trajectory (bottom left) and imagery keel location (bottom right) for Keel 88 Envisat APP image acquisition 20050315_05:42:02

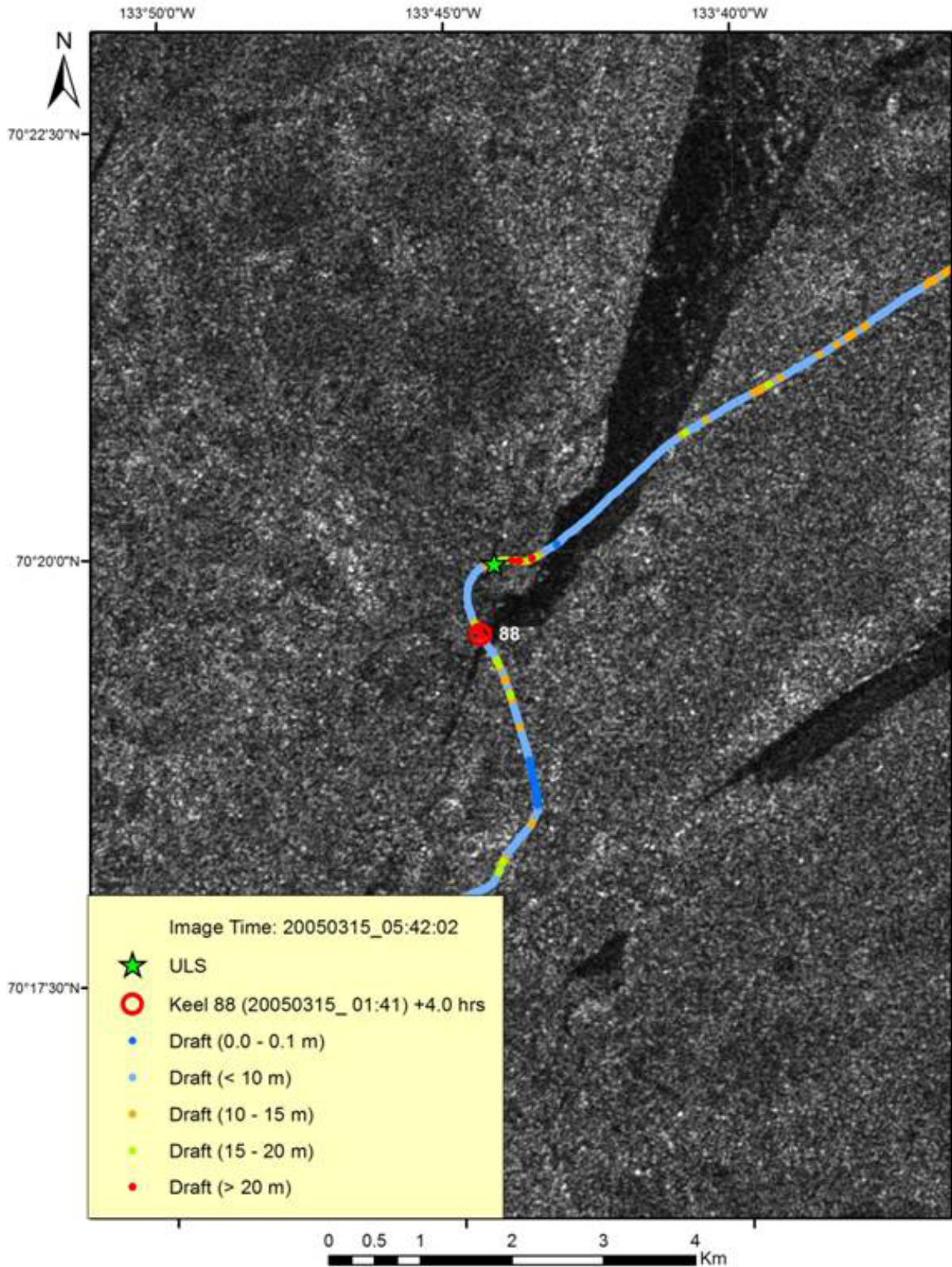


Figure 65. Envisat APP image (acquisition time 20050315_05:42:02) for Keel 88

4.2.12 Keel 92 in Envisat APP

Coverage for keel 92 is provided with an Envisat APP image (image swath IS6, incidence angle 39.1° - 42.8°) acquired on 20050511. ULS data collected between the time of keel detection and image acquisition are shown in Figure 66 and the Envisat images are shown in Figure 67. The CIS classify sea ice at keel 92 location as predominantly first-year thick with trace amounts of old ice. While there are features (rubble piles and what appear to be ridges) evident throughout the image, resolution impedes positive identification. Figure 68 shows a feature crossing the drift trajectory just east of the keel 92 projected location, however, the pixel 'coarseness' makes it difficult to identify with a high degree of confidence.

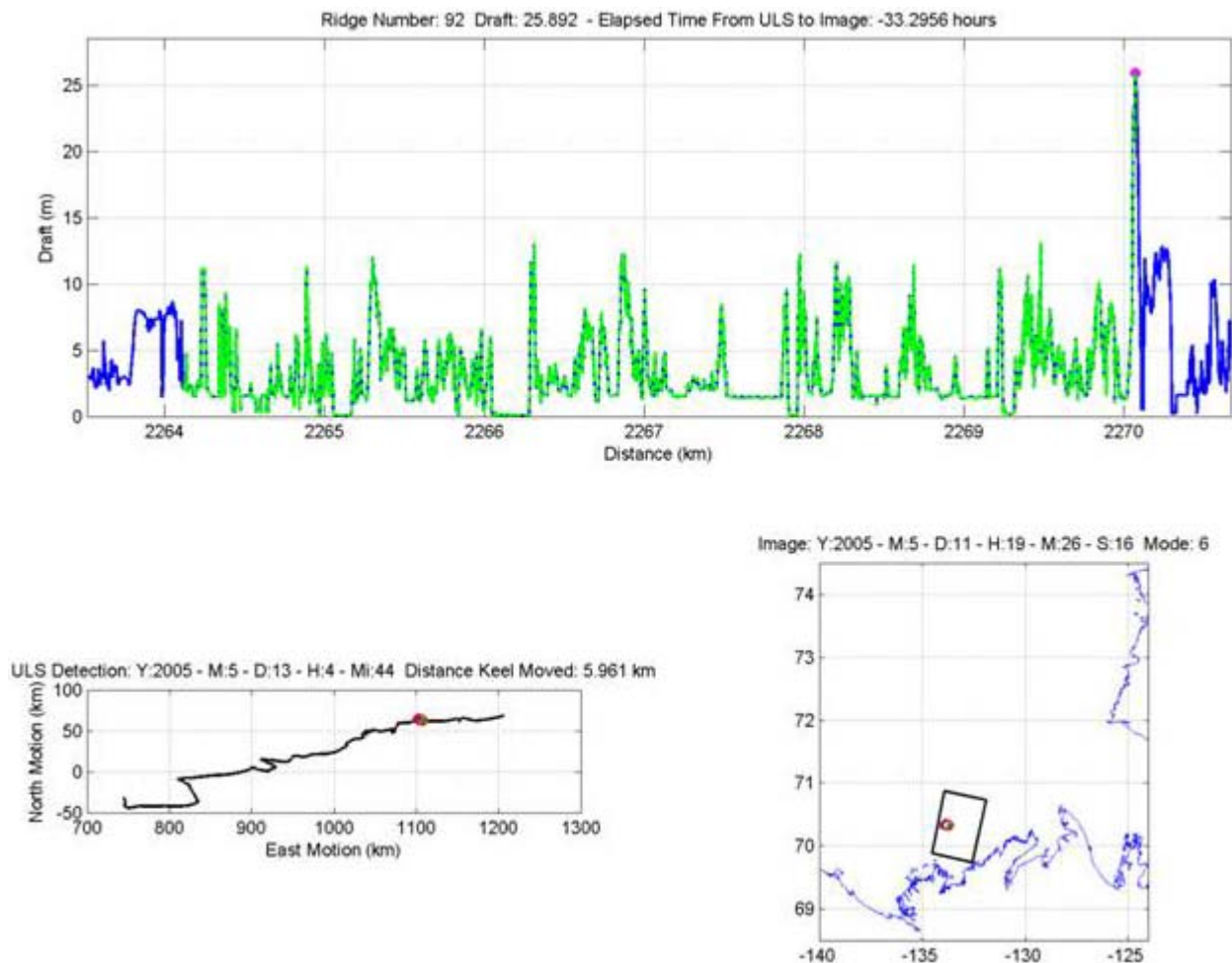


Figure 66. Sea ice draft profile (top), projected drift trajectory (bottom left) and imagery keel location (bottom right) for Keel 92

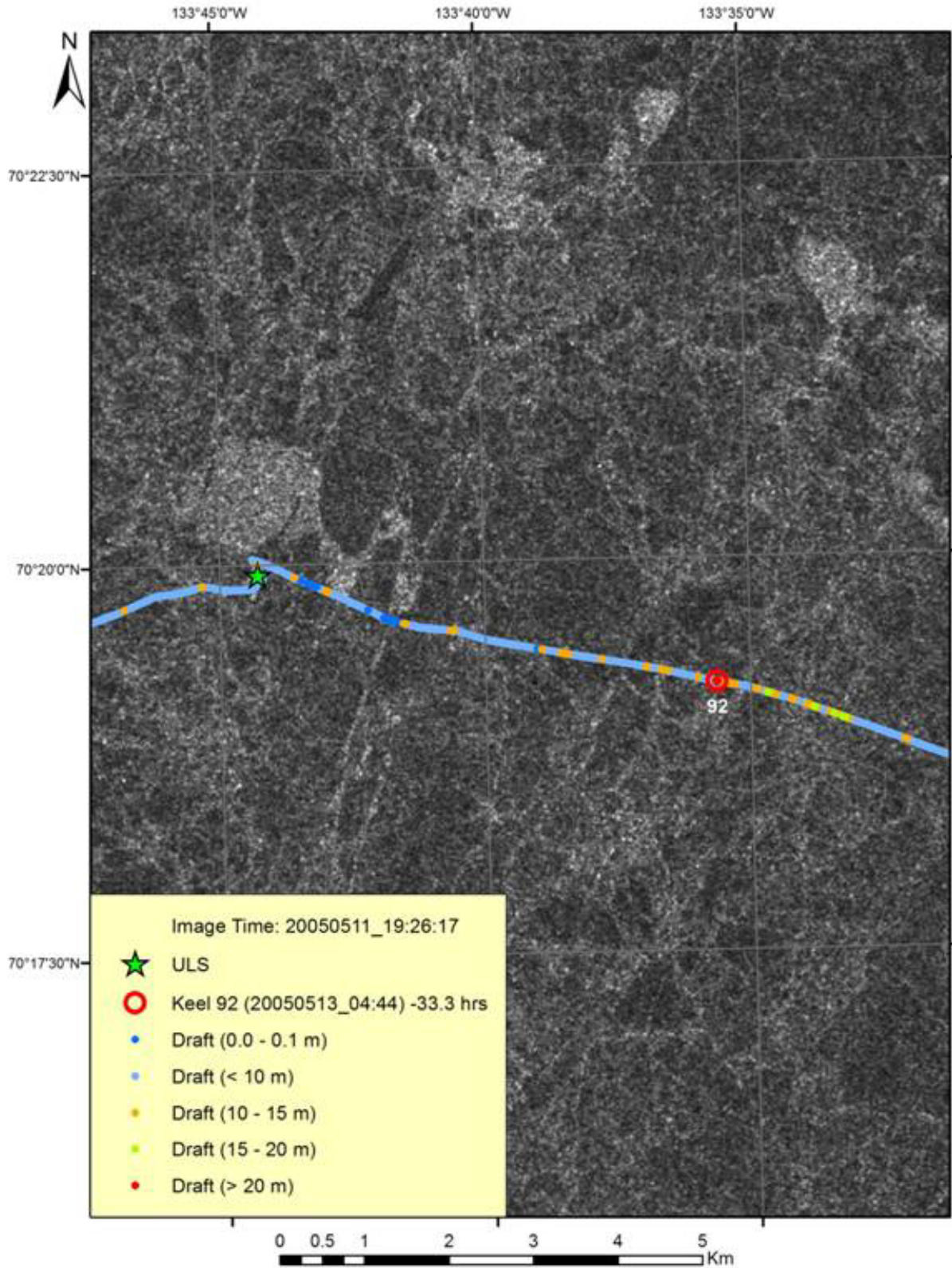


Figure 67. Envisat APP image (acquisition time 20050511_19:26:17) for Keel 92

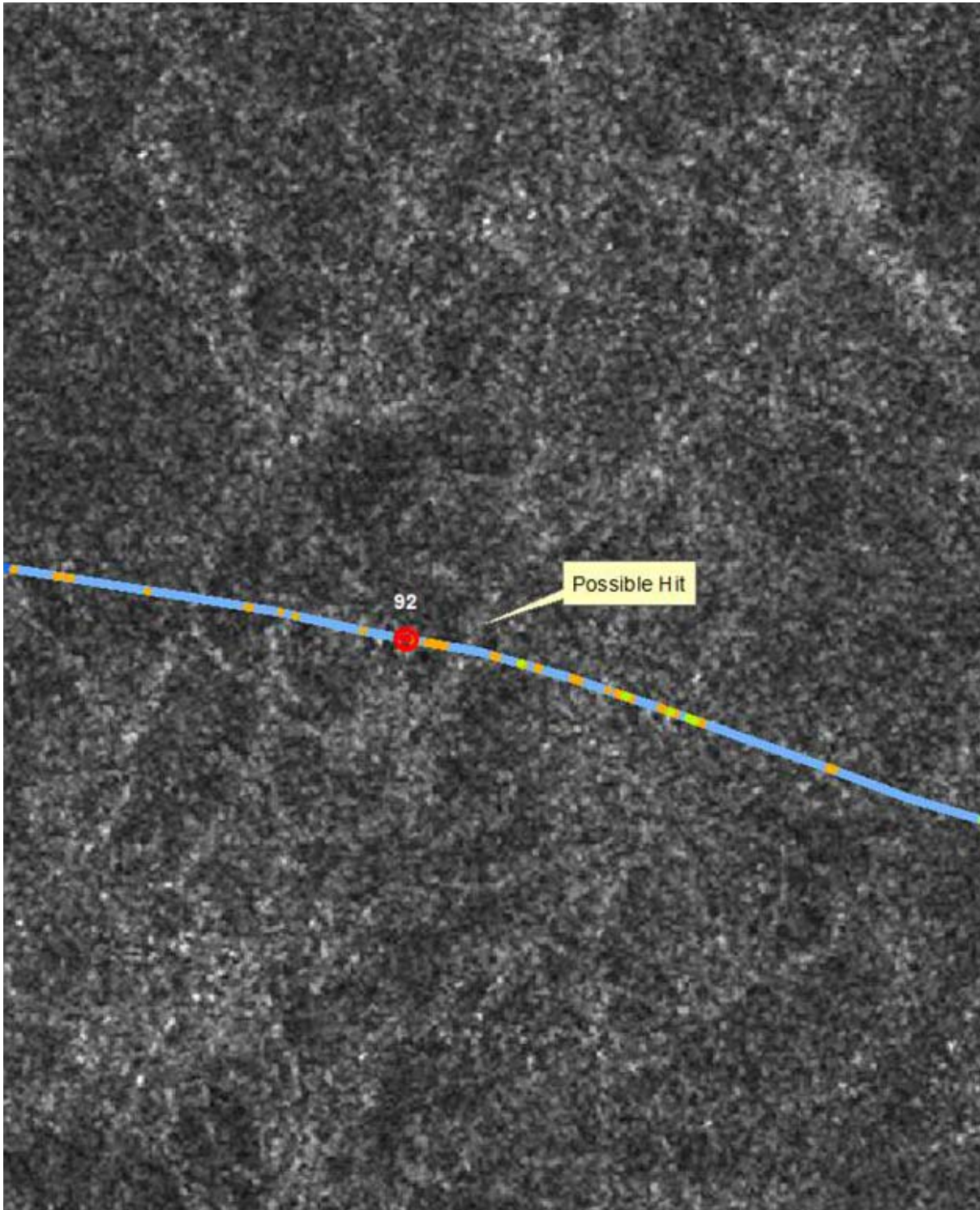


Figure 68. Possible hit for keel 92

4.2.13 Keel 117 in Envisat

Coverage for keel 117 is provided by an Envisat WS image acquired on 20080420. The CIS classifies sea ice at the keel location as predominantly first-year thick with lesser concentrations of first-year medium and trace amounts of old ice. ULS data collected between the time of keel detection and image acquisition is shown in Figure 69, and the Envisat WS image is shown in Figure 70. Although some larger features are visible (rubble fields), there is poor correlation between ULS data and surface features. The coarse resolutions of these data type make it unsuitable for this type of application.

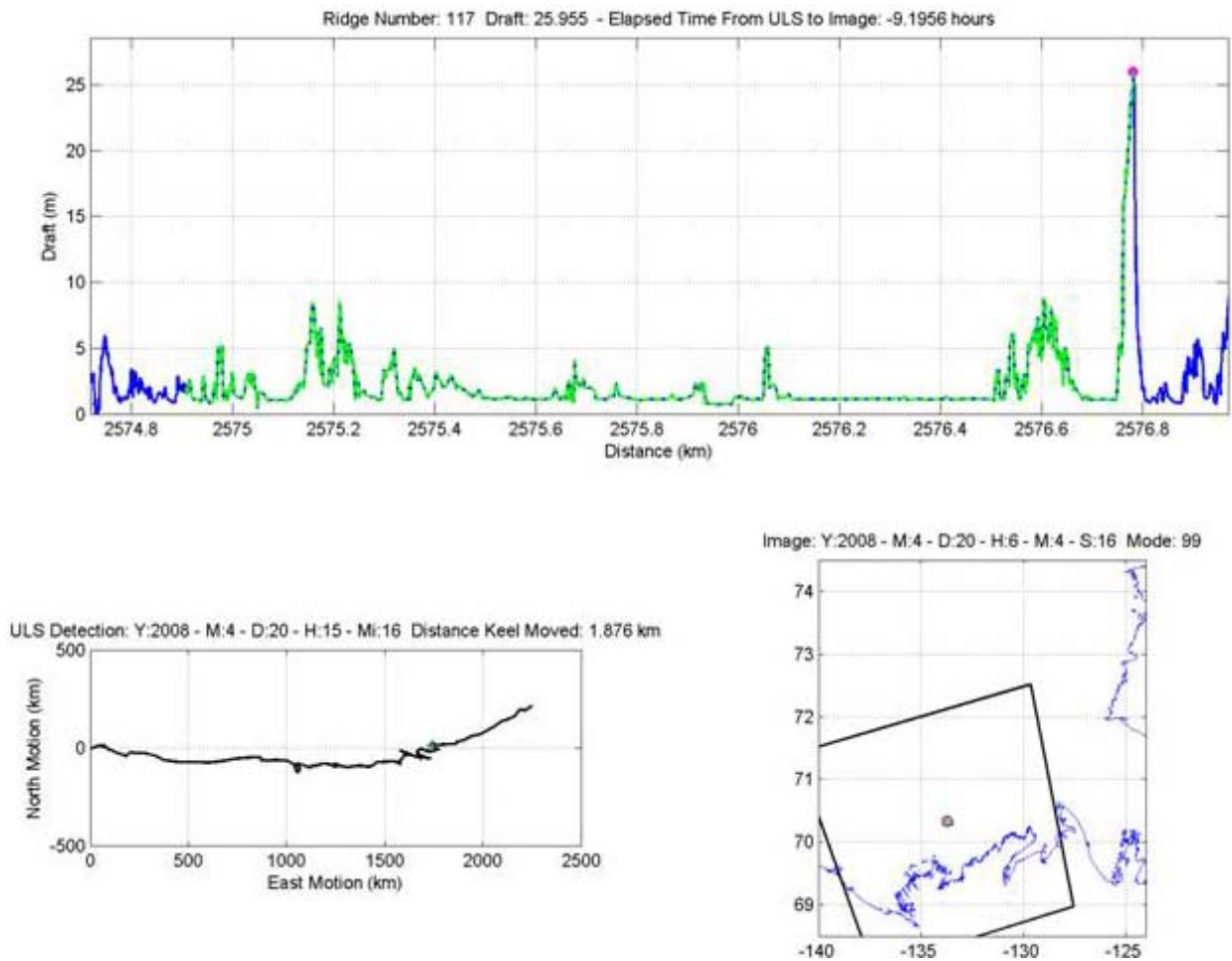


Figure 69. Sea ice draft profile (top), projected drift trajectory (bottom left) and imagery keel location (bottom right) for Keel 117

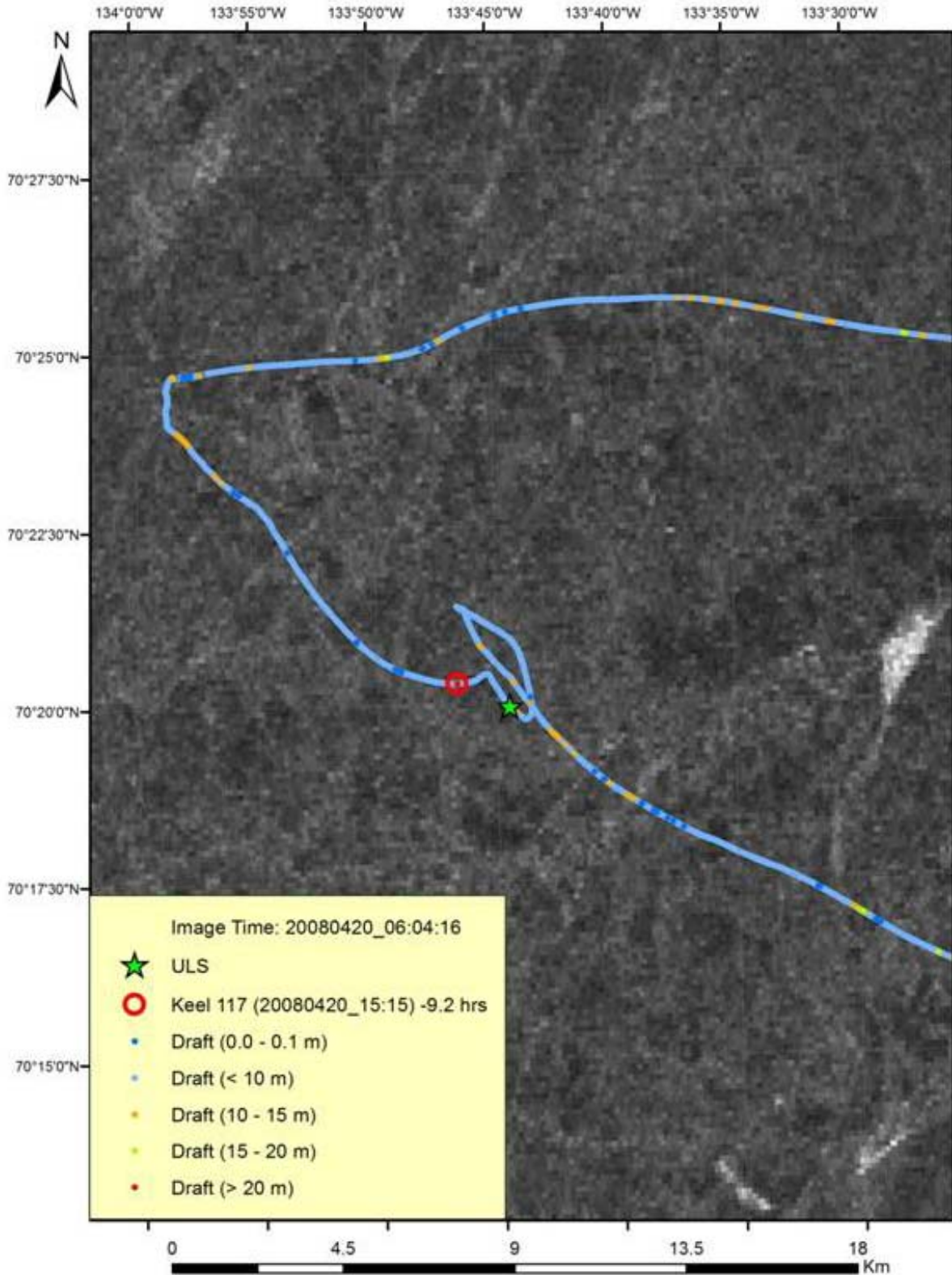


Figure 70. Envisat WS image (acquisition time 20080420_06:04:16) for Keel 117

4.3 SUMMARY OF ANALYSIS

Correlation of ULS data and various satellite imagery platforms achieved limited success partly due to several factors. Availability of suitable imagery held in the various archives corresponding both spatially and temporally with ULS data collection provided limited options. Ice dynamics played a major role in attempting to successfully correlate surface features to ULS output. Figure 71 illustrates how quickly conditions can change; the differences shown in the figure occurring over a mere 9 hours. The degree of confidence in ULS data correlation decreased with increased distance from ULS locations, especially in imagery acquired in late spring and early summer when break-up is underway. Attempting to correlate data with surface features in mixtures of loose floes and open water leads was difficult to perform with any degree of confidence. While surface features were evident in SAR imagery, they were not clearly identifiable compared to features in optical imagery.

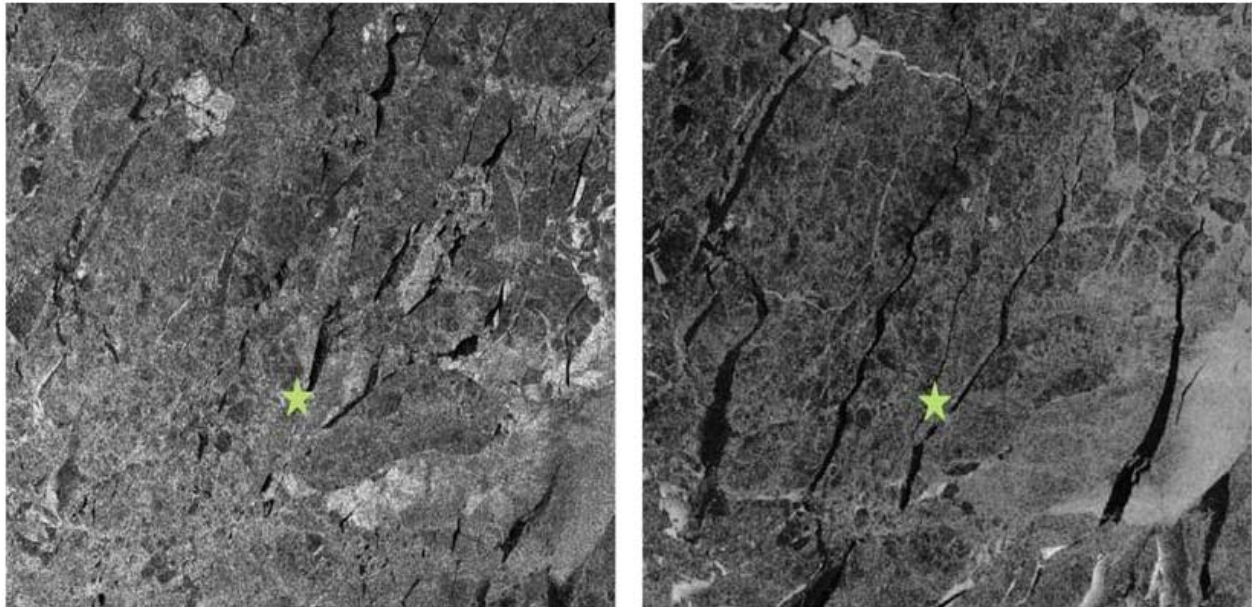


Figure 71. Envisat WS 20050314_19:48:27 (left) and Envisat APP 20050315_05:42:02 (right) illustrating mobility and dynamics of ice sheet

5 ADDITIONAL DATA SOURCES CONSIDERED

5.1 SATELLITE PLATFORM COMPARISON PARAMETERS

5.1.1 SAR/Electro-Optical (EO)

Synthetic aperture radar is the *de facto* standard for monitoring ice conditions and was the primary motivation of RADARSAT-1 and other satellites. Each year national ice centers use thousands of satellite SAR images to monitor ice conditions in the Antarctic, Arctic and sub-Arctic regions. Radar is an active sensor and can be used for imaging day and night and can penetrate fog and cloud cover. SAR data has high information content, but expert image interpretation is required.

Understanding EO data is more intuitive since images are similar to photographs. Data can be captured in black and white as well as multiple optical and infra-red channels, however the cloud cover that is prevalent in polar regions limits the usefulness of EO data.

5.1.2 Tasking

Satellites may be designed for scientific or commercial purposes. Scientific satellites, such as ENVISAT and Landsat, collect data with a set acquisition schedule. These satellites may be tasked with specific image orders, provided that the request does not interfere with the scientific priorities. Baseline data collection usually consists of low resolution data, which can be shared with all interested users.

Commercial satellite data, such as from RS2 and TSX, can be tasked as required, however, conflicts can arise when there are multiple users. To minimize conflicts, end users can work together in developing acquisition plans or higher priority can be purchased. Standard image orders can be placed up to three days in advance for most satellites, but later programming can be purchased if required.

Satellite tasking is important when supporting operations and coordinating with field trials. Tasking was not relevant for this project since historical data were analyzed, but it may be important in the future.

5.1.3 Resolution

The resolution of a sensor determines its ability to resolve two closely spaced objects and is related to the smallest size object that can be reliably distinguished. Older satellites were available at low and medium resolution up to 10 m. Recently launched satellites have resolutions as fine as 40 cm. Data available for this project had resolutions ranging from 150 m to 15 m. High resolution data will be better at detecting ridges.

5.1.4 Coverage

There is generally an inverse relationship between coverage area and resolution. High resolution data are available in narrow swath widths and low resolution data have broader coverage areas. The data used for this project had coverage widths ranging from 400 km to 100 km. Since the satellites are polar orbiting, it is possible to collect multiple images in the roughly north-south direction.

5.1.5 Revisit

Imaging satellites are polar orbiting, which allows them to capture data more frequently close to the poles. A constellation of satellites provides more imaging opportunities than a single satellite. Older satellites were individual, but CSK and TSX presently operate in constellations. As well, the large number of satellites presently in operation can be used together as a virtual SAR constellation.

5.1.6 Bands

A single satellite image may consist of multiple channels of information. Satellite SAR data are available at multiple polarizations and EO data have several spectral bands. Older satellites, such as RADARSAT-1, were available in single polarization. The satellite would transmit horizontally polarized radiation (H) and receive horizontally polarized radiation and would be known as HH data. Similarly vertically polarized transmit and receive would result in the VV channel. Each polarization is sensitive to different target aspects and using multi polarized data provides additional information useful for detecting and classifying features. Recently launched satellites can collect data in dual polarization or quad polarization. The additional polarizations occur when there is horizontal transmit and vertical receive (HV) and vertical transmit and horizontal receive (VH). Quad polarized data has four channels of image information as well as phase differences between the channels. Most of the data acquired for this project was single polarization, but some medium resolution dual polarized data (ENVISAT) were used as well.

Multispectral imagery is acquired using portions of the electromagnetic spectrum. Examples of these include red, blue, green, near infrared, mid infrared, and far infrared. Landsat and SPOT are examples of multispectral satellites. These satellites provide the color images, such as those used in Google Earth and Bing Maps.

Hyperspectral is similar to multispectral imagery, except hyperspectral uses smaller portions of the electromagnetic spectrum, providing a large variety of images channels. These sensors contain channels that go beyond what the human eye can perceive.

5.1.7 Archive

All data acquired for this project were ordered from the archive. Most of the archive SAR data were low resolution images originally ordered by Canadian Ice Service (CIS) for monitoring ice conditions. These data are from RADARSAT-1/2 and ENVISAT. Recently launched satellites, such as TerraSAR-X and COSMO SkyMed have also captured images in the area to tap into the potential market for images.

Archived low and medium resolution EO data are also available in the archives, primarily from scientific missions. Due to the prevalence of cloud cover over the Arctic, many of the available images will be at least partially degraded.

5.1.8 Cost

In general, data from scientific missions are free, while commercial data are available at the cost of a few thousand dollars per image. Commercial satellites, such as TSX and CSK, allow research users to obtain data at greatly reduced costs. RS2 data may be available at no cost, if the research project is through a Canadian Federal Department. All SAR satellites charge less for low resolution data.

High resolution multispectral imagery can be ordered from archived databases or the satellite can be tasked to acquire an image with an additional fee. The cost of optical data is based on the number of square kilometers required and there is a minimum purchase quantity. Archive data are available at reduced rates.

Table 5 to Table 15 show the parameters for several older and newer SAR and optical satellite sensors.

Table 5. Overview of ENVISAT

Parameter	ENVISAT
Launch Date	March 2002
SAR/EO	SAR – C-band
Tasking	Scientific mission, but can be tasked for specific acquisitions with 15 day lead time
Resolution	Data most commonly acquired at 150m resolution, but 30m and 1km data also available
Revisit	Single satellite system
Coverage	Data most commonly acquired in 400km swath width, but 100km data also available.
Bands	Can operate in single polarization (HH,VV) or dual polarization (HH/HV, HH/VV, VV/VH). Dual polarized data has roughly 100km swath width.
Archive	Substantial low resolution data of Arctic and Antarctic regions available in archive
Cost	Both new acquisitions and archive data are available free of charge

Table 6. Overview of RADARSAT-1

Parameter	RADARSAT-1
Launch Date	November 1995
SAR/EO	SAR – C-band
Tasking	Commercial mission, but failure of onboard data recorder means that images can only be captured in the vicinity of downlink stations. This is not a major restriction since downlink stations cover the Arctic. Satellite must be tasked a minimum of three days in advance
Resolution	Data are frequently acquired in 100 m and 50 m resolutions, but 25 m and 10 m data are available as well
Revisit	Single satellite system
Coverage	Swath width ranges from 500 km to 50 km
Bands	Single polarization HH alone
Archive	Substantial low and medium resolution data of Arctic and Antarctic regions available in archive
Cost	Approximately \$4000+ per image, with discounts for bulk orders and archived scenes

Table 7. Overview of RADARSAT-2

Parameter	RADARSAT-2
Launch Date	December 2007
SAR/EO	SAR – C-band
Tasking	Commercial mission with a large number of users in the Arctic. Standard ordering is three days advance notice, but emergency orders are accommodated up to four hours prior to image acquisition
Resolution	Resolution ranges from 100 m to 1 m (Spotlight mode).
Revisit	Single satellite system
Coverage	Swath width ranges from 500 km to 20 km. Consecutive Spotlight images cannot be acquired.
Bands	Single and dual polarization available for most imaging modes. Quad polarization available at medium and high resolution with reduced swath coverage
Archive	Archive data of Arctic and Antarctic regions available in archive
Cost	Approximately \$3500 to \$9000+ per image, with discounts for bulk and archive orders

Table 8. Overview of TerraSAR-X

Parameter	TerraSAR-X
Launch Date	June 2007
SAR/EO	SAR – X-band
Tasking	Commercial mission with a growing number of users. Standard order deadline of three days, but exclusive programming with approximately 12 hours advance notice is possible
Resolution	Resolution ranges from 16 m to 1 m (Spotlight mode).
Revisit	Dual satellite system, second satellite lags by hundreds of metres
Coverage	Swath width ranges from 100 km to 5 km. Consecutive Spotlight images cannot be acquired.
Bands	High resolution (6 m) dual polarization data available. All other data is single polarization
Archive	Data of Arctic and Antarctic regions available in archive
Cost	Approximately \$4000 to \$8500+ per image, with discounts for bulk orders and archive data

Table 9. Overview of COSMO SkyMed

Parameter	COSMO SkyMed
Launch Date	June 2007 to November 2010
SAR/EO	SAR – X-band
Tasking	Commercial mission with a growing number of users. Standard ordering is approximately two and a half days in advance, but 12 hour lead time can be accommodated
Resolution	Resolution ranges from 30 m to 1 m (Spotlight mode).
Revisit	Constellation of four satellites, revisit within hours
Coverage	Swath width ranges from 200 km to 10 km. Consecutive Spotlight images cannot be acquired.
Bands	Dual polarization data available at medium resolution. All other data is selectable single polarization (HH, HV, VV or VH)
Archive	Data of Arctic and Antarctic regions available in archive
Cost	Approximately \$2000 to \$12,000+ per image, with discounts for bulk orders

Table 10. Overview of MODIS

Parameter	MODIS
Launch Date	December 1999 (Terra) and May 2002 (Aqua)
SAR/EO	EO – Multispectral
Tasking	Continuous data acquisition, tasking not required
Resolution	Resolution varies from 250 m to 1 km
Revisit	Constellation of two satellites, revisit within hours
Coverage	Swath width of 2330 km
Bands	Imaging at 36 spectral bands covering visible and infrared (IR)
Archive	Large quantity of data of Arctic and Antarctic regions available in archive
Cost	All data are free of charge

Table 11. Overview of Landsat 5 & 7

Parameter	Landsat 5 & 7
Launch Date	March 1984 and April 1999
SAR/EO	EO – Multispectral
Tasking	Data acquisition over land masses for scientific purposes, tasking not possible
Resolution	30m (multispectral) and 15m (panchromatic for Landsat 7)
Revisit	Sporadic, based on scientific requirements
Coverage	Swath width of 185 km
Bands	Seven spectral bands, including visible, near IR, mid IR and thermal. Landsat 7 has an additional panchromatic band in the visible range
Archive	Data over Arctic and Antarctic regions available in archive
Cost	All data are free of charge

Table 12. Overview of SPOT 4 & 5

Parameter	Spot 4 & 5
Launch Date	March 1998 and May 2002
SAR/EO	EO – Multispectral
Tasking	Satellite sensors can be tasked for specific areas and date ranges. Satellite can be tasked up to 24 hours prior to acquisition
Resolution	Resolution varies from 2.5m to 20m. Highest resolution in panchromatic mode
Revisit	With two satellites potential revisit is within a few hours
Coverage	Nominal 60 km by 60k m, but 60 km by 80 km at nadir
Bands	Five spectral bands, including visible, near IR and shortwave IR
Archive	Data over Arctic and Antarctic regions available in archive
Cost	All data are free of charge

Table 13. Overview of WorldView-1/2

Parameter	WorldView-1/2
Launch Date	September 2007 and October 2009
SAR/EO	EO – Multispectral
Tasking	Satellite sensors can be tasked for specific areas and date ranges. Satellite can be tasked up to 24 hours prior to acquisition
Resolution	Resolution varies from 0.5 m to 2.4 m. Highest resolution in panchromatic mode
Revisit	Up to once every 1.7 days with WorldView-1, and 1.1 days with WorldView-2. Together
Coverage	Nominal 17.6 km for WorldView-1 and 16.4 km for WorldView-2
Bands	Imaging with eight multi spectral bands, including visible and near IR plus a panchromatic band
Archive	Data available in archive over the Arctic close to land and lesser quantities available offshore
Cost	Standard prices vary from \$20 to \$40/km ² with a minimum purchase of \$1800 for new acquisitions and \$14 to \$28/km ² for archive orders with minimum purchase of 25/km ² .

Table 14. Overview of RapidEye

Parameter	RapidEye
Launch Date	August 2008
SAR/EO	EO – Multispectral
Tasking	Standard tasking window of 45 days to guarantee acquisition, but shorter time frames available as well
Resolution	Resolution of 6.5 m
Revisit	Constellation of five satellites with frequent revisit
Coverage	Nominal 77 km swath width
Bands	Imaging with five multi spectral bands, including visible and near IR
Archive	Data available in archive over the Arctic and Antarctic close to land
Cost	Cost of \$1.28/km ² with a minimum order of 500 km ²

Table 15. Overview of GeoEye

Parameter	GeoEye
Launch Date	August 2008
SAR/EO	EO – Multispectral
Tasking	Satellite can be tasked for new acquisitions
Resolution	Resolution of 0.4 m (panchromatic) to 1.65 m (multispectral)
Revisit	Revisit within three days, will be improved when GeoEye-2 is launched late 2012
Coverage	Swath width of 15.2 km
Bands	Imaging with five multi spectral bands, including visible, near IR and panchromatic
Archive	Not available
Cost	Cost of \$12.50/km ²

5.2 COMPARISON BETWEEN EO AND SAR SENSORS

SAR and EO data provide differing and complementary information on ice conditions. SAR data are strongly dependent on surface roughness and geometry of the target. Even composition is relevant as radar signals will not penetrate the surface and have volume scatter from high salinity ice. It is challenging to unambiguously identify large ridges in SAR imagery, since small ridges, rafting, rubble ice and refrozen leads have similar signatures. SAR is useful for detecting deformed ice and studies have shown that there is a correlation between the number of

filaments observed and the average ice thickness in that area (Melling, 1998). SAR imagery is used by all the national ice centres for reporting on ice concentration, stage of development and floe sizes and is the single biggest application of SAR data. Optical imagery has the potential to provide information on ridging.

Optical imagery is easier to interpret as it provides a natural view of an area. Fewer linear features are visible over sea ice, but the filaments that are present can be reported as ridges with higher confidence. Images collected when the sun is closer to the horizon will have shadows from features that have surface relief. The reliance on the position of the sun means that it is easier to detect ridges that are perpendicular to the sun and very difficult to detect ridges that are parallel.

Cloud cover and the non-optimal angle of the sun may limit the quantity of optical data, but a system using both SAR and EO data can provide useful results. Initial detection of extreme features can be conducted using optical data and then correlated with routinely collected low resolution SAR data. The low resolution SAR data will be sufficient for detecting large ridges of interest. Continual monitoring and tracking of the ridge can take place using SAR data, possibly at high and medium resolution to improve detection success. Occasional high resolution EO acquisitions are recommended to determine if any new large ridges are being formed. Significant ridging is known to take place during storm conditions (Melling et al., 1993), suggesting that high resolution acquisitions be planned around those events.

5.2.1 Imaging Extended Features

Extended features, such as ridges will are typically visible in satellite SAR and optical data, if the sensor resolution is no more than three to five times bigger than the width of feature of interest (Dierking and Dall, 2007; Melling, 1998). However, the brightness of the signature in SAR data from that extended feature does not necessarily correlate to the height of the feature (Melling, 1998). Figure 72 shows snowmobile tracks over a frozen river as imaged by RADARSAT-2 UltraFine 3 m data. Even though the width and height of the track is much less than 3 m, it is clearly visible in the image. Similarly, a number of filamentary features are found in SAR imagery over sea ice, but those linear features may be due to several phenomena, not just large ridges.

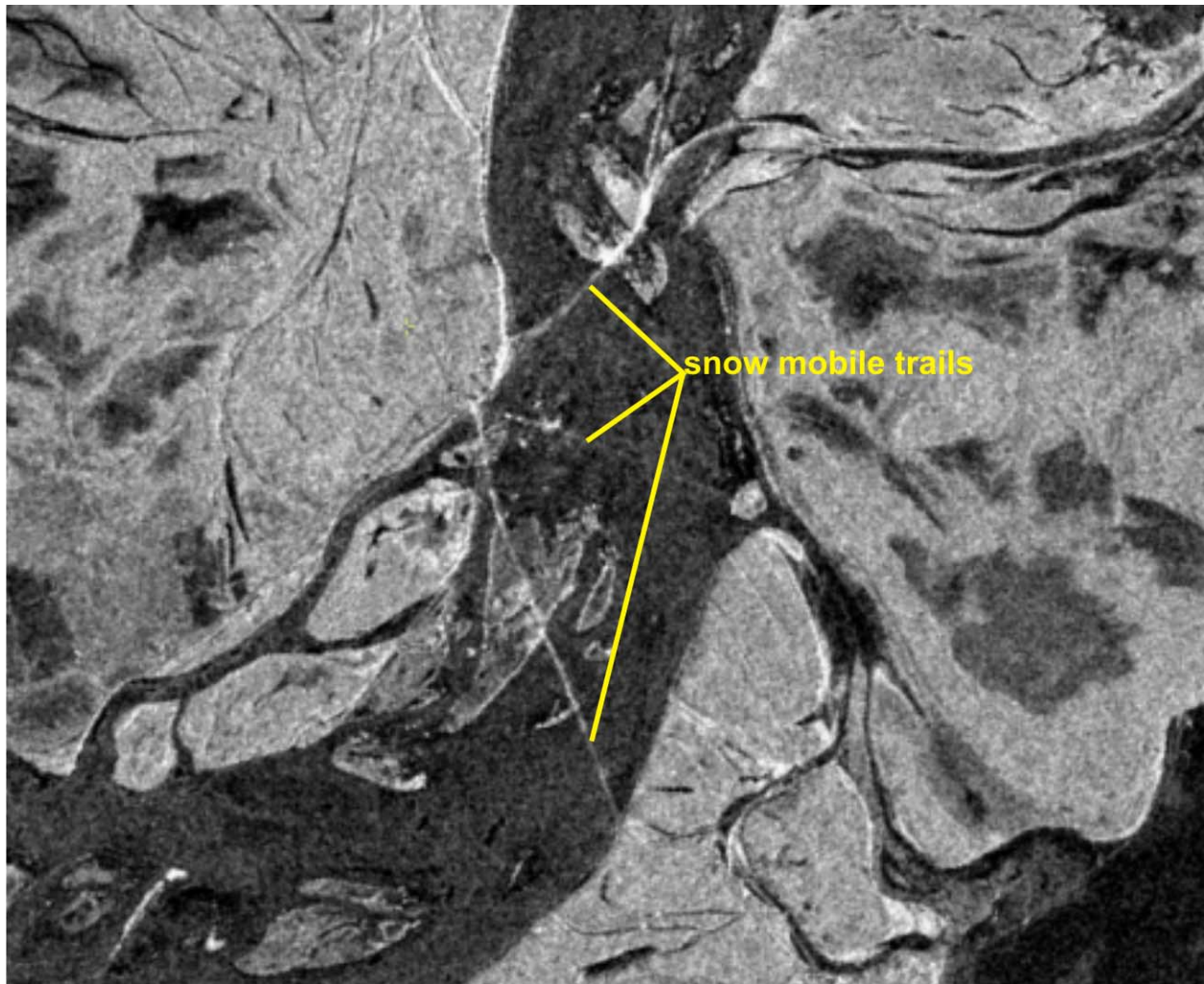


Figure 72. RADARSAT-2 U77 3m February 13, 2012 10:25:50 UTC

5.3 CRYOSAT-2/LANDSAT COMPARISON

Processed data from the European Space Agency's CryoSat-2 satellite only became available late in the project. Sufficient overlap coupled with available imagery limited comparison to three lines of data and one Landsat 7 image acquired on 20110524. Given the mobility of the ice in that portion of the image and the temporal change between image acquisition and Cryosat-2 data this was further reduced to two lines (green and purple in Figure 73). These lines represent +/- one day either side of acquisition date.

The complex waveform data stream from the CryoSat-2 altimeter requires a sophisticated processing scheme, in particular for exploiting the synthetic aperture and interferometry techniques over ocean and ice surfaces.

The main data product is the 'Level 2' product; sometimes called the Geophysical Data Record. This contains the surface elevation along the ground track together with all auxiliary data needed to fully exploit these measurements.

Height of surface (HoS) was extracted from the Level 2 product and compared to ice features appearing in the image. Plots of height of surface as a function of latitude are shown in Figure 74 for ground track 20110525T070716 and Figure 75 for ground track 20110523T070942. The only observation noted was the HoS which showed finite over water, experienced a sharp return to zero over ice. At the time of this reporting, the data format is such that a proper evaluation cannot be completed.

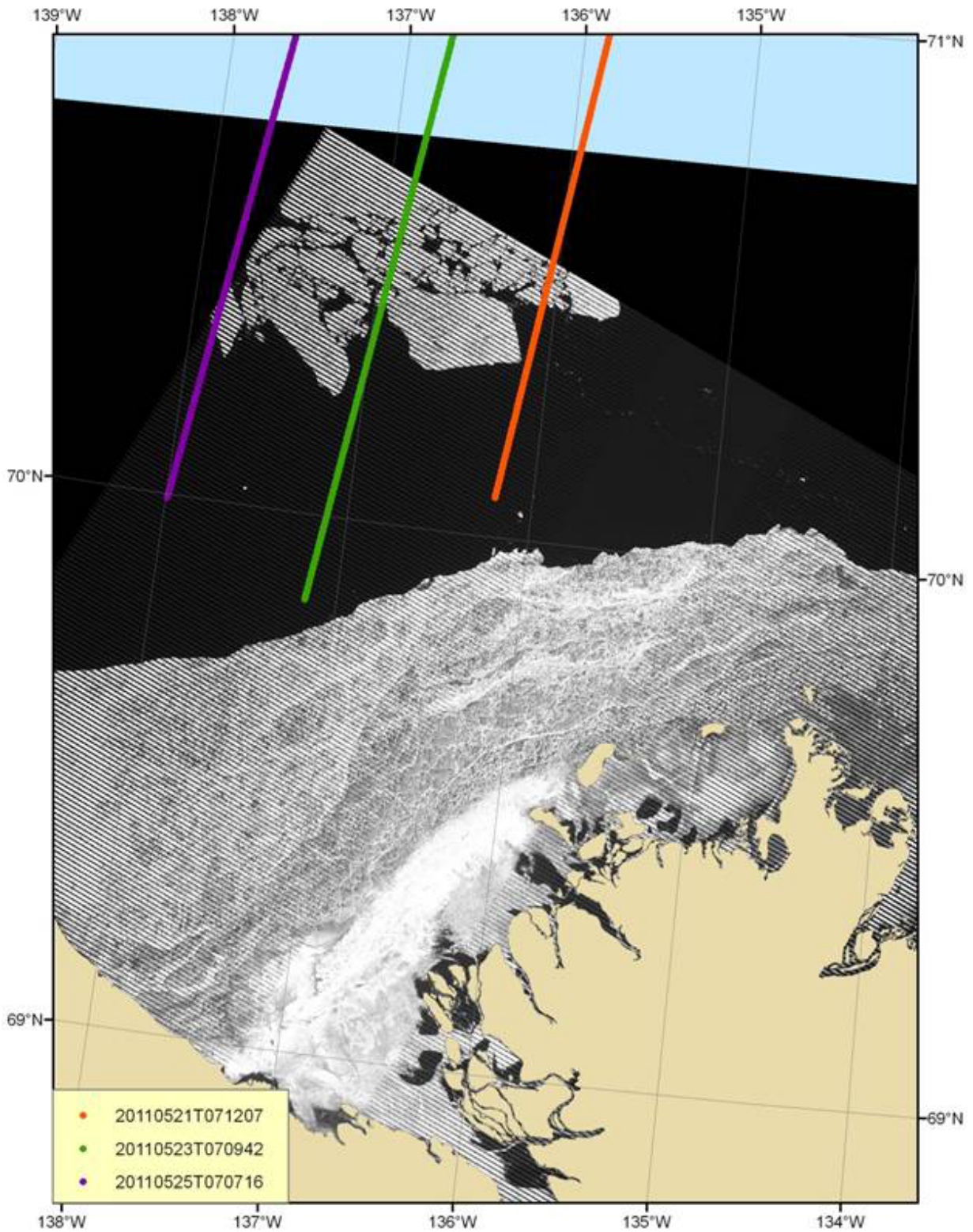


Figure 73. Location of Cryosat-2 data ground tracks

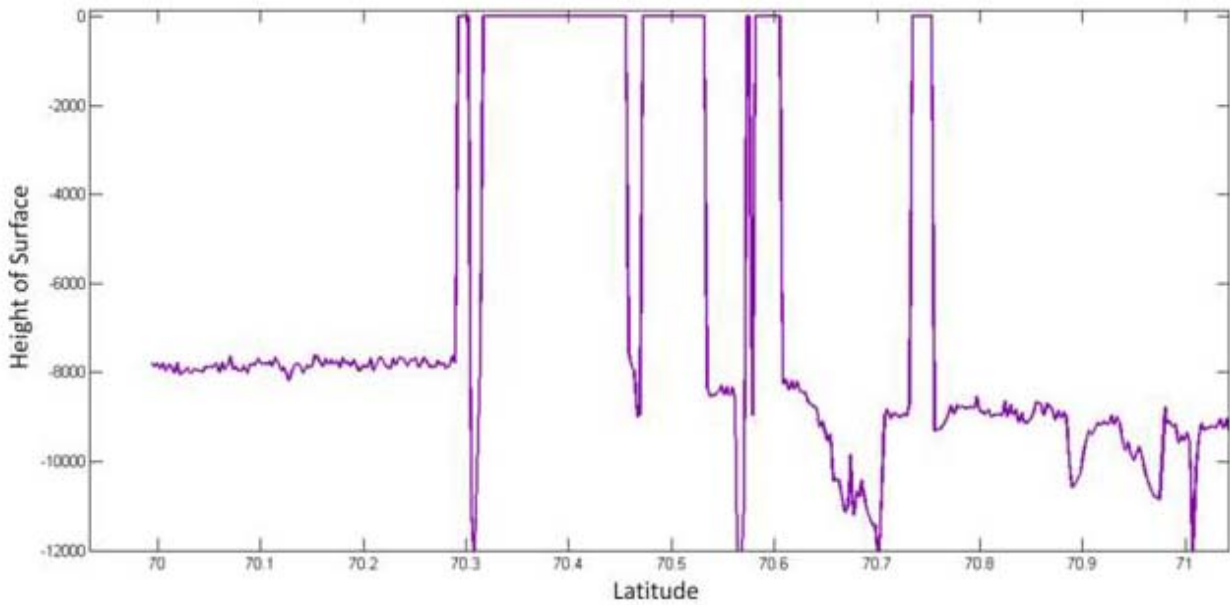


Figure 74. Cryosat-2 height of surface (HoS) vs Latitude for ground track 20110525T070716

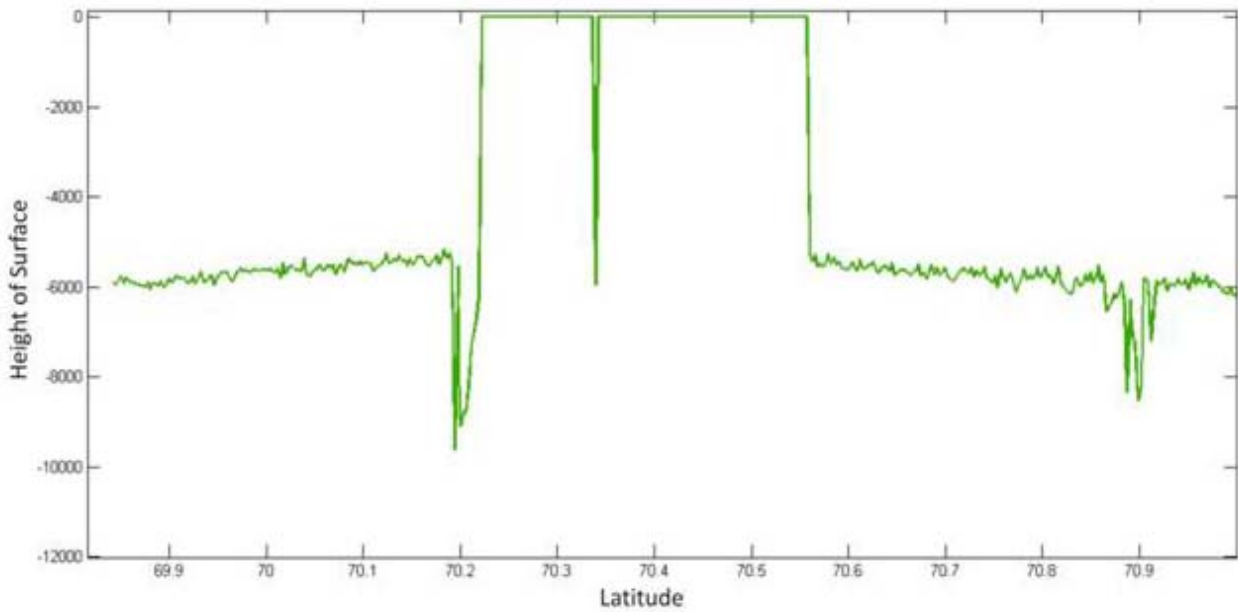


Figure 75. Cryosat-2 height of surface (HoS) vs Latitude for ground track 20110523T070942

5.4 COSMO-SKYMED COMPARISON

Other data types investigated include COSMO-SkyMed ScanSAR Wide shown in Figure 76 and ScanSAR Wide HH shown in Figure 77. Both are single look complex with 30 m resolution. There are no ULS data available at this time to attempt correlation of features, however surface features are identifiable in this image type.

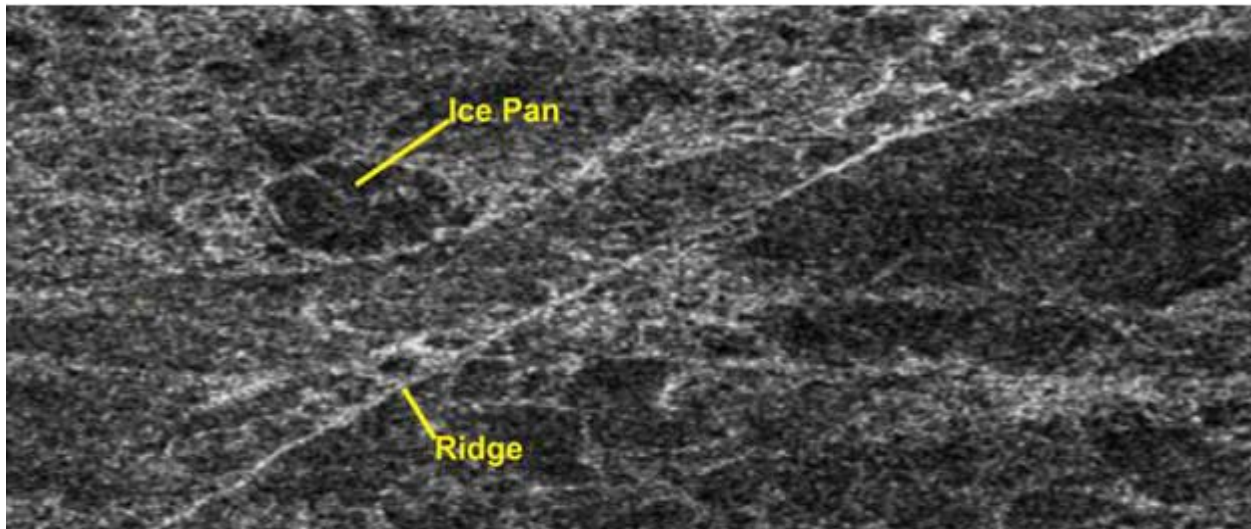


Figure 76. COSMO-SkyMed ScanSAR Wide (image acquisition 20100501_14:34:55) showing ridge

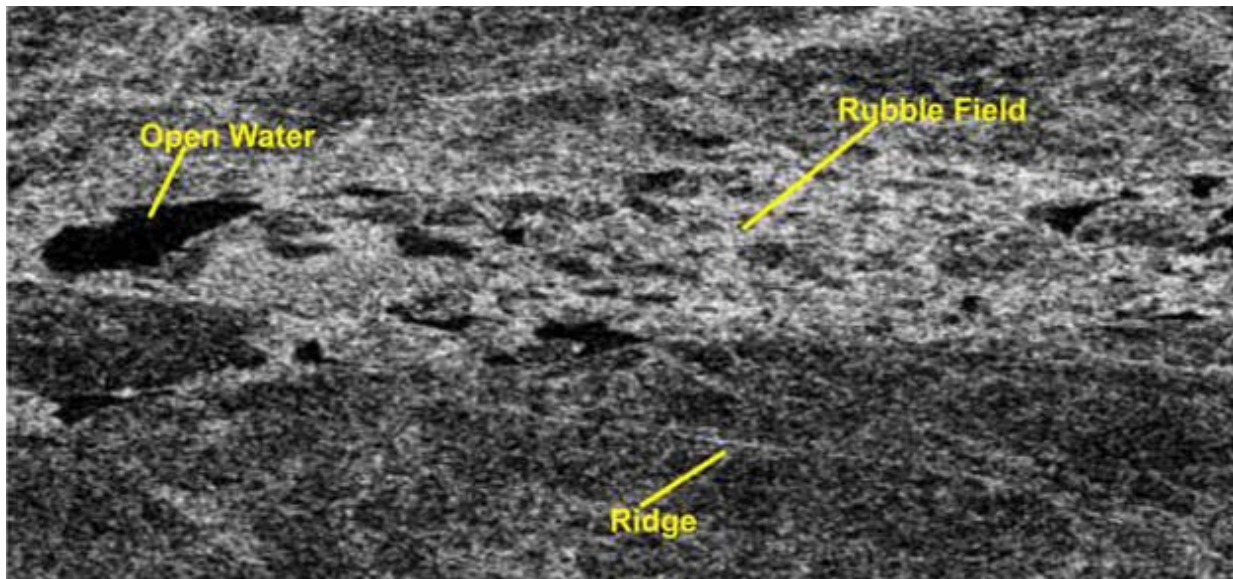


Figure 77. COSMO-SkyMed ScanSAR Wide HH (20100501_11:40:42) showing ridge feature, open water leads and rubble field

5.5 QUICKBIRD

High resolution Quickbird optical imagery has also been investigated. Figure 78 shows a sample portion of a panchromatic multispectral (MS) optical image (60 - 70 cm resolution) acquired on 20090525. Unfortunately the actual image has not been delivered at the time of this reporting. Figure 79 shows a close up of a portion of the image depicting several ridge features. The actual image which will appear in the final version of the report is anticipated to show these features in very high detail with a high degree of confidence.

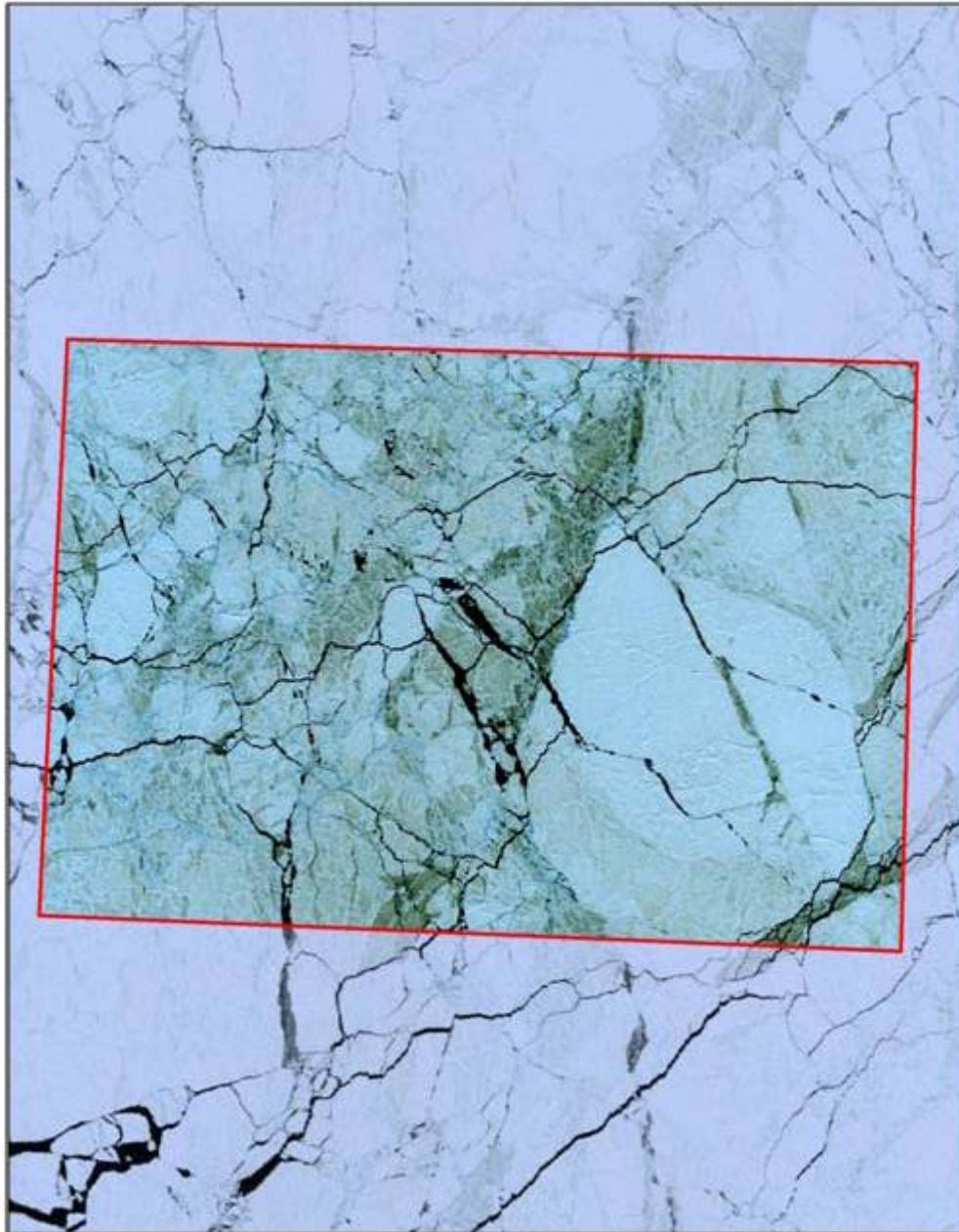


Figure 78. Sample of a Quickbird multispectral (MS) optical image acquisition date 20050525

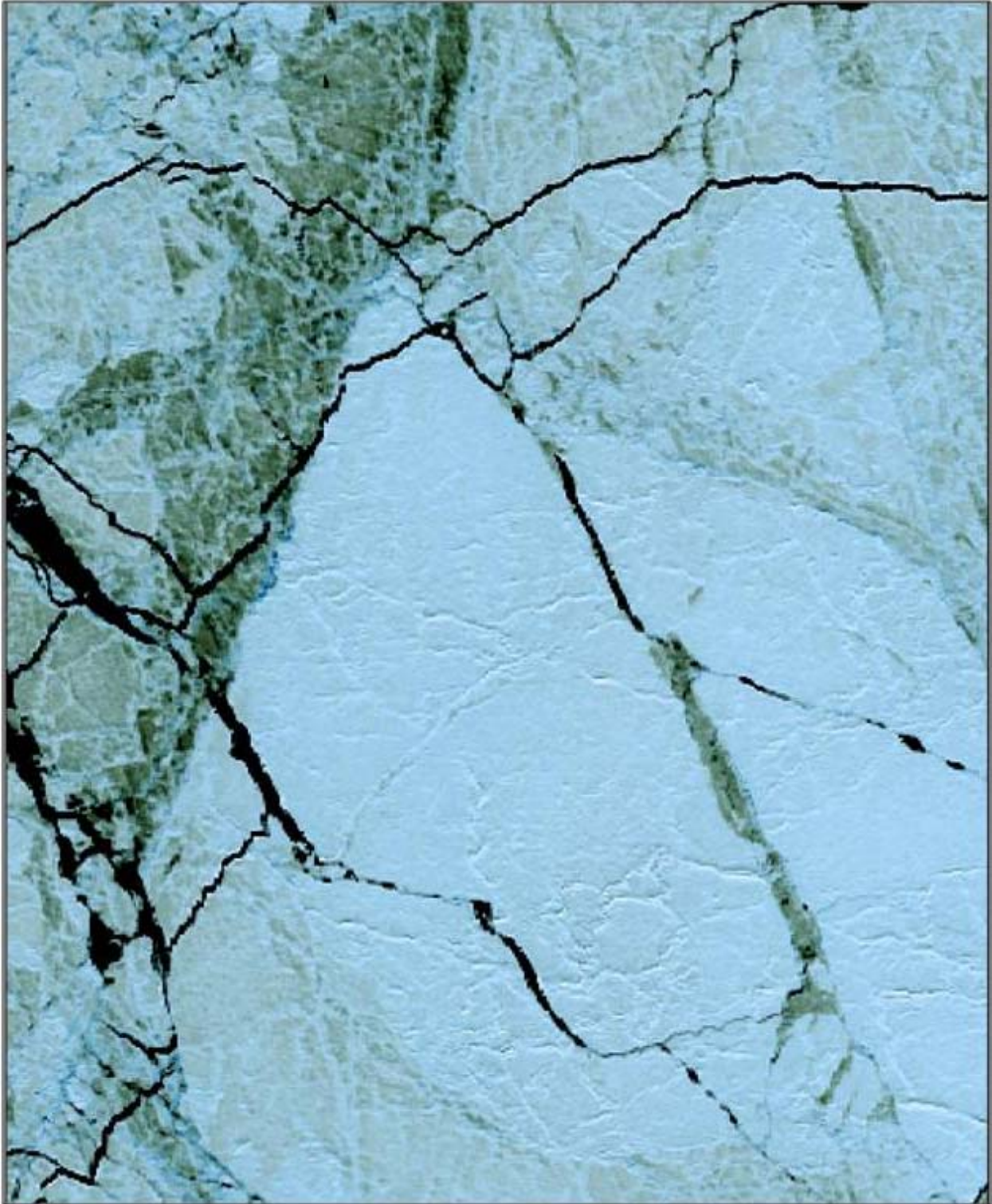


Figure 79. Close-up of sample Quickbird image showing ridge features

6 SEA ICE RIDGE DETECTION USING OPTICAL SATELLITE IMAGERY

6.1 INTRODUCTION

Sea ice ridges are readily identifiable in high resolution optical imagery such as Quickbird or Landsat-7. Quickbird panchromatic imagery having a 0.6 m resolution has a better probability of detecting smaller ridge features than coarser resolution Landsat-7 panchromatic at 15 meter resolution. Coarser resolution optical imagery such as Landsat-5 can also be used to identify larger ridge features. The Landsat-7 panchromatic data presented here was processed and quality controlled to identify 152 ridge features in sea ice floe. These ridge features were most often elongated bright regions with an adjacent associated shadow (see Figure 80). Ridge features lengths identified here were observed to range from tens of kilometers to as small of hundreds of meters.

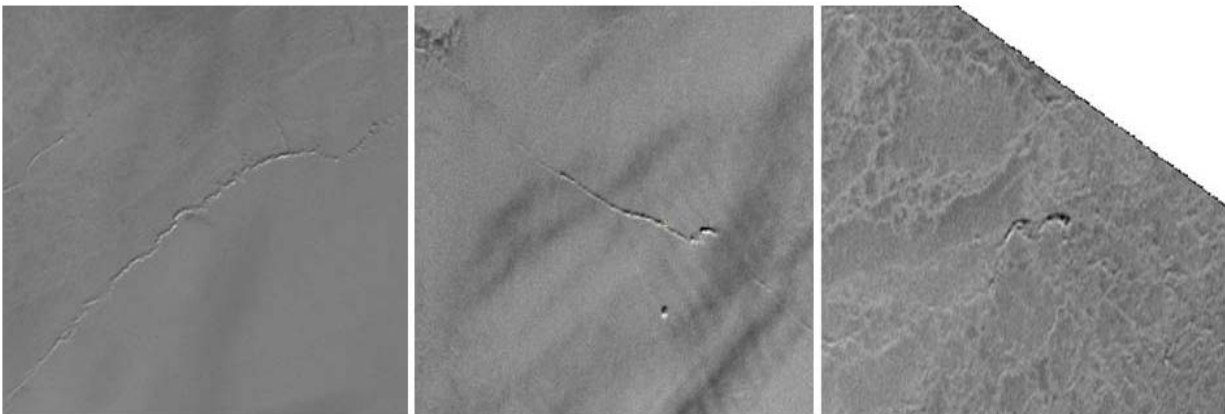


Figure 80. Sample ridges taken from Landsat-7 20110401 (202147)

6.2 PROCEDURE

The algorithmic approach to detecting these ridges as presented here follows a two step process. The first step is to identify edge features in the image. An edges feature algorithm uses drastically changing neighboring pixel intensity values to identify spatial non-homogeneity in the image. There were two edge detection methods evaluated for this work, Sobel and Canny (Canny 1986, Parker 1997). Both the Canny and Sobel edged detection methods work well (Figure 81) but under certain circumstances one can outperform the other. Here the Canny edge detected was found to nominally outperform Sobel for a subset of the ridges identified.

Canny edge detection has a threshold associated with it. Adjusting this threshold helps identify features that are of interest. Here, most of the samples in a 500 by 500 image clip are either due to sea ice or open water. Figure 82 shows a sea ice sample ridge acquired during seasonal break up. It is notable that the fracture lines in the sea ice are most apparent during break up and are considered a hindrance for ridge detection as they are a major source of false alarm

detections. In Figure 82, the Canny edge detector threshold was set such that 20%, 10%, 5%, 2.5% and 1.25% of the total pixel count in the image processing window were identified as edges. It was found that a Canny threshold of 5% for a 500 by 500 processing window produced the best compromise between capturing most true ridge features and to a lesser extent minimizing sea ice and open water false alarm edge features.

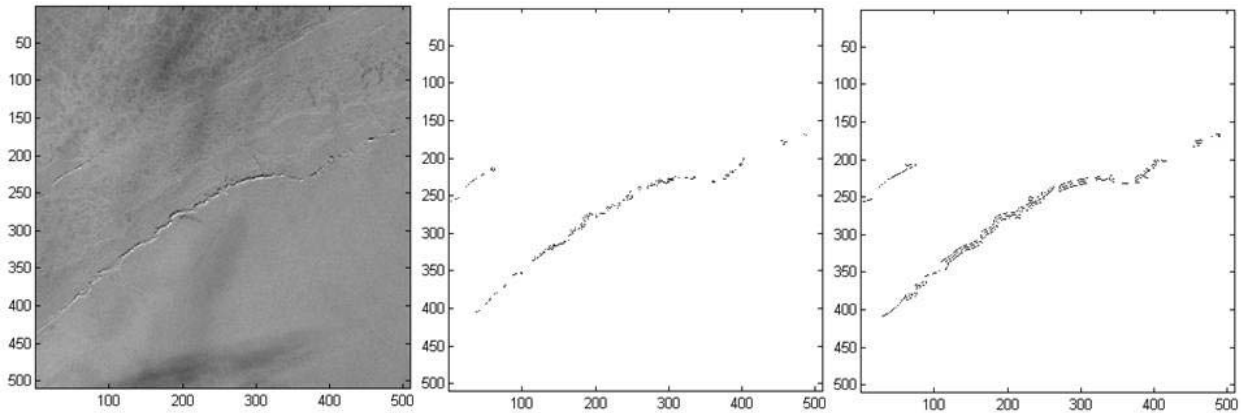


Figure 81. Sample ridge (left), Sobel (middle) and Canny (right) edge detection

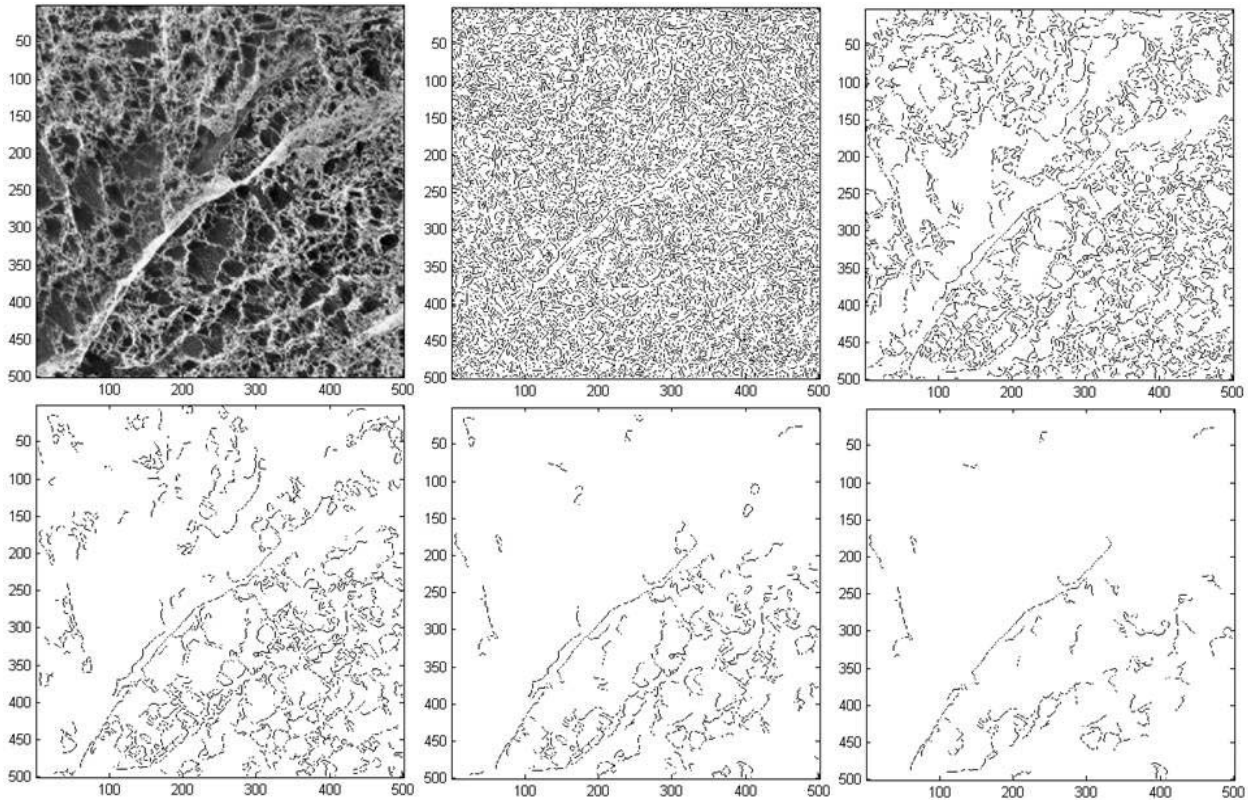


Figure 82. Sea ice sample (top left) and progressive Canny edge detection results

The second step in the algorithmic approach taken is adaptive histogram processing. Here a threshold is set that identifies bright pixel values in the upper tail of the intensity histogram (see Figure 83). It is notable that the intensity histogram has the SLC error (see Section 4.2.3) removed, this is done such that detection is based on separating sea ice intensity signature from ice ridge intensity. SLC error, seen as the black regions that stretch across the image processing window on a diagonal, has a constant intensity value of zero which makes identifying and filtering SLC trivial. Note that the ridge identified in Figure 83 has relatively bright pixel intensity values (i.e. 190) compared to the surrounding sea ice (i.e. mean 163.5).

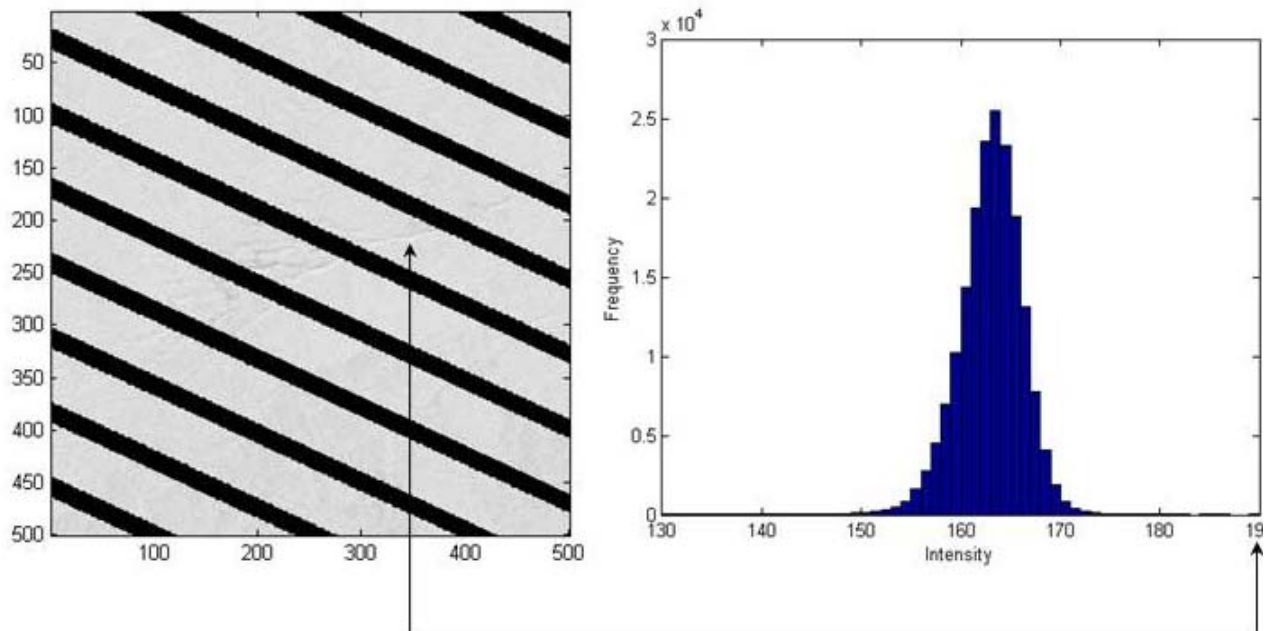


Figure 83. Landsat-7 sample sea ice ridge with SLC error (left) and histogram of sea ice intensity

Traditionally, adaptive histogram processing uses a fixed number of standard deviations plus the background mean as a threshold for each processing window. Any pixel above this threshold is considered a ridge. This method works well when a homogeneous sea ice background exists; however, there are occurrences (see Figure 84) on seasonal sea ice break up when open water leads and sea ice floe create a bimodal distribution. Optimizing an adaptive threshold to be globally applied under all conditions of sea ice partial concentrations and open water is not trivial. Consider a threshold derived from a number of standard deviations plus the mean for both sea ice processing windows presented in Figure 83 and Figure 84. In Figure 83, the mean plus three standard deviations would work well but this threshold would not work well for the mixed sea ice and open water case presented in Figure 84. From this, applying an adaptive threshold via a fixed number of standard deviations from the mean would produce subpar results if a robust global algorithm is to be used on all image types.

Alternatively, a constant percentage threshold rate was applied. This method was chosen as it is not dependant on the ratio of background sea ice or open water signature. From Figure 85, the adaptive threshold via brightest percentage method demonstrates pixel detections for 10%, 5%, and 2.5%, 1.25% and 0.625% of the total pixel count. It was found that an adaptive threshold via percentage of 5% for a 500 by 500 processing window produced the best compromise between capturing true ridge features and minimizing sea ice false alarms.

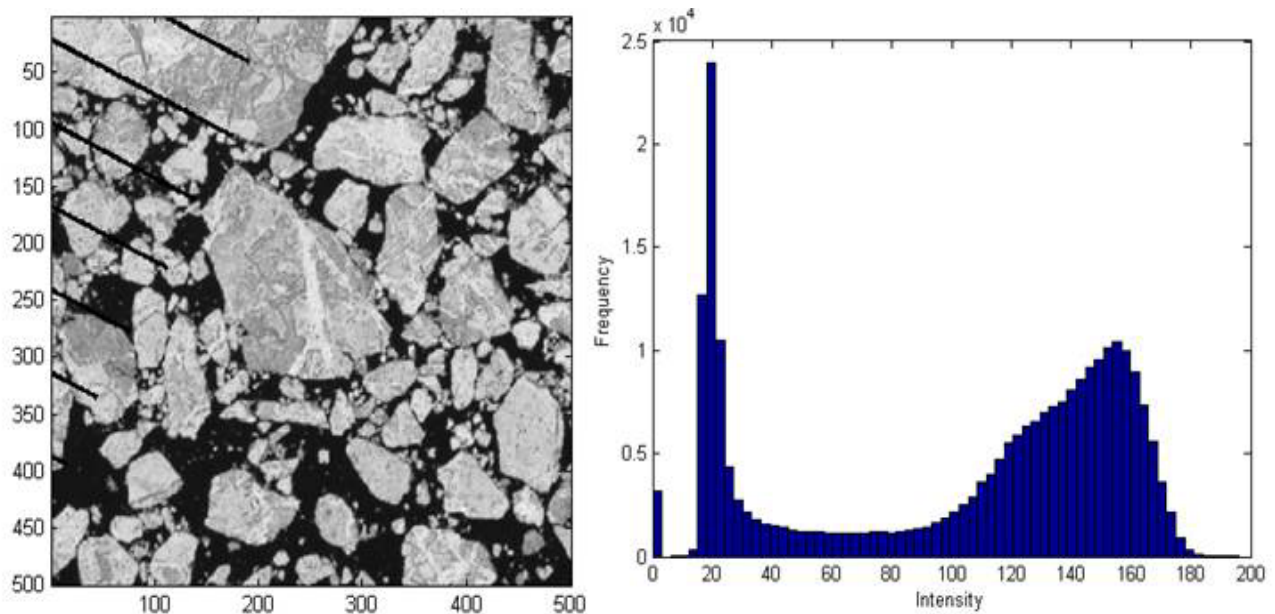


Figure 84. Landsat-7 sample sea ice ridge during seasonal sea ice break up (left) and histogram of sea ice and open water intensity

Post edged and bright pixel intensity detection, the two binary images produced are multiplied together to create a bright edge product. This image is then filtered to remove small and non-elongated targets. This was accomplished using image processing criteria for a linear likeness feature, eccentricity, and physical area. Eccentricity ranges from zero to one, where zero represents a circular shaped target and one a straight line. Here only targets identified with an eccentricity measure of 0.95 or greater and a physical area of 0.05 km^2 or greater were assigned potential ridge status. This step removes a large portion of small false alarm sea ice targets and larger objects that are not elongated.

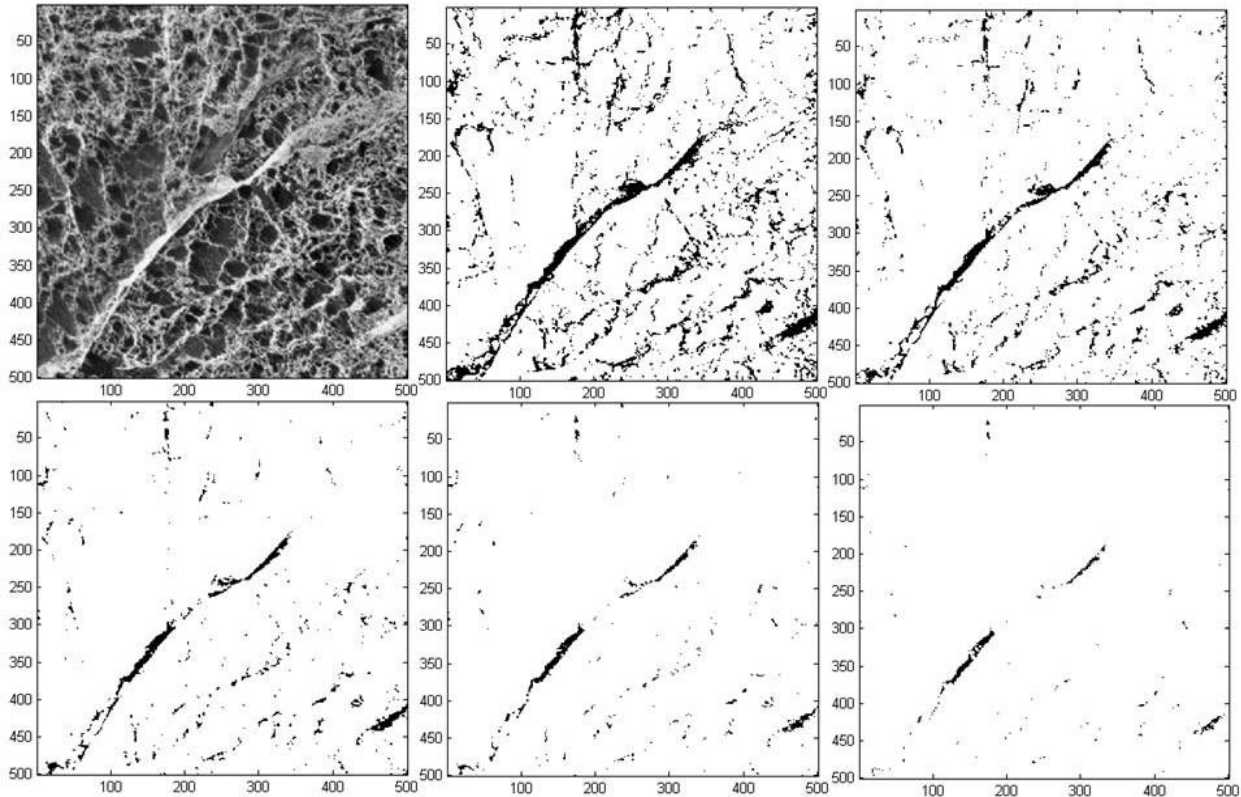


Figure 85. Sea ice sample (top left) and progressive percentage threshold detection results

6.3 RESULTS

Four case studies are presented, ridges identified with ideal homogeneous sea ice backgrounds and are free of SLC error, ridges identified in SLC prone backgrounds, ridges identified during seasonal sea ice break up and ridges identified with cloud and cloud shadow conditions. These conditions were specifically selected as they were observed to significantly affect the probability of ice ridge detection in Landsat-7 imagery.

6.3.1 Ice Ridge Detection Under Ideal Conditions

Sea Ice ridges are readily detectable using Landsat-7 optical or higher resolution imagery under ideal conditions. These include minimal cloud cover and cloud shadow, low intensity homogeneous sea ice signature, SLC free processing window, and do not occur during seasonal sea ice freeze up or break up. Figure 86 presents a typical example of what is considered ideal conditions under which a ridge can be detected in Landsat-7 imagery. Of the 152 sea ice ridge features identified for this work, 109 we considered to be under ideal conditions. For the ridges identified under ideal conditions, 82% (89) were detected using the algorithm as presented here. Additional analyses could include consideration of the number of false alarms.

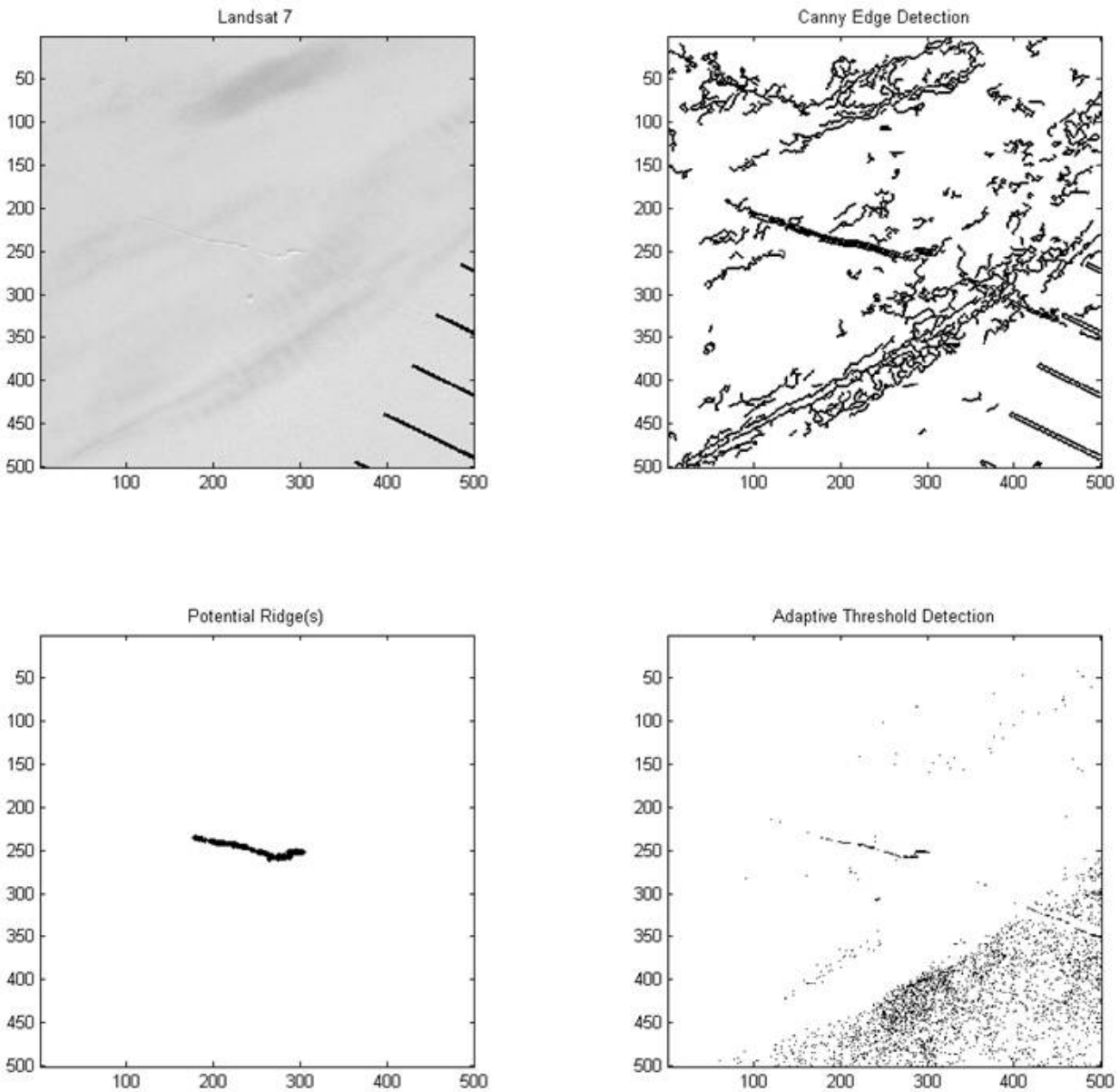


Figure 86. Ridge detection under ideal conditions using Landsat-7

6.3.2 Ice Ridge Detection with SLC Error

Sea ice ridges are readily detectable using Landsat-7 optical even with SLC error. Though ridges cannot be identified wholly due to “dead data” SLC regions, ridges can be detected and through interpretation length and width can be accessed with reasonable accuracy. Figure 87 presents an example of a SLC error prone sea ice ridge in Landsat-7 imagery. Here the segments can be interpreted through a quality control process to belong to one or multiple ridge(s) based on proximity and ridge segment orientation.

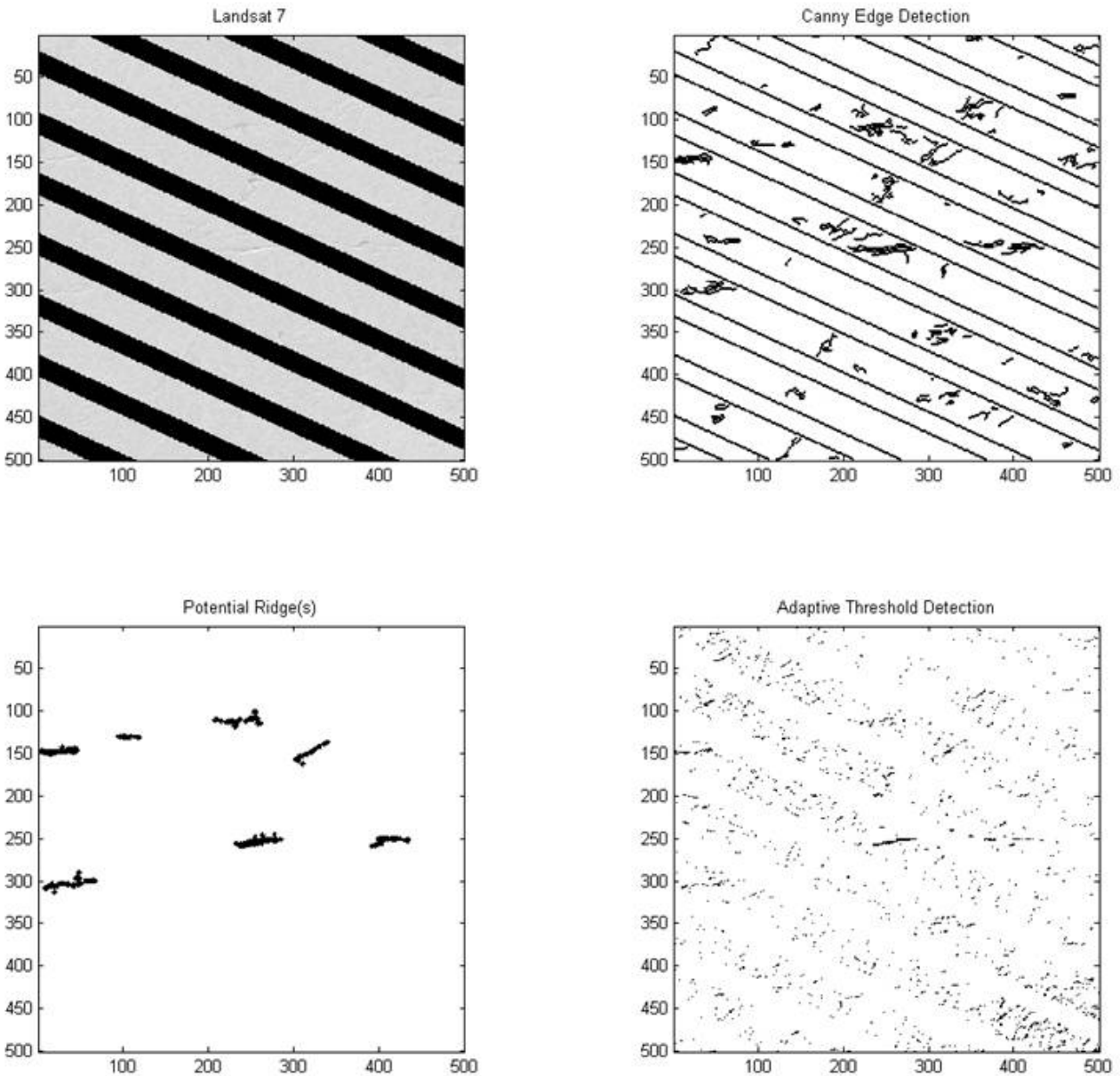


Figure 87. Ridge detection under SLC error conditions using Landsat-7

Of the 152 sea ice ridge features identified for this work, 15 we observed to contain SLC error but otherwise occurred under ideal environmental conditions. For these ridges identified under SLC error, 80% (12) were detected using the algorithm as presented here. Additional analyses could include consideration of the number of false alarms.

6.3.3 Ice Ridge Detection with Cloud or Cloud Shadow

Identifying sea ice ridges with cloud or cloud shadow significantly limits the probability of detection when using Landsat-7 optical. Cloud cover can fully mask an optical image such that sea ice and open water cannot be discernible. Cloud cover can also be opaque allowing partial light reflectance from the sea ice and open water. As seen in Figure 88 cloud opacity significant reduces sea ice features in landsat-7 data.

Under ideal conditions, a ridge reflects sunlight and hence shows up bright in an image and based on the ridge height and angle to the sun, a ridge casts shadow. This creates an elongated feature in an image that is bright on one side and has an adjacent dark shadow making a ridge identifiable. Contrary to this is the occurrence of a ridge in a cloud shadow, firstly the ridge itself will not be as bright and secondly there will be little or no ridge shadow. Figure 88 shows cloud cover opacity and cloud shadow effects on decreasing sea ice feature content useful for determining ridge features.

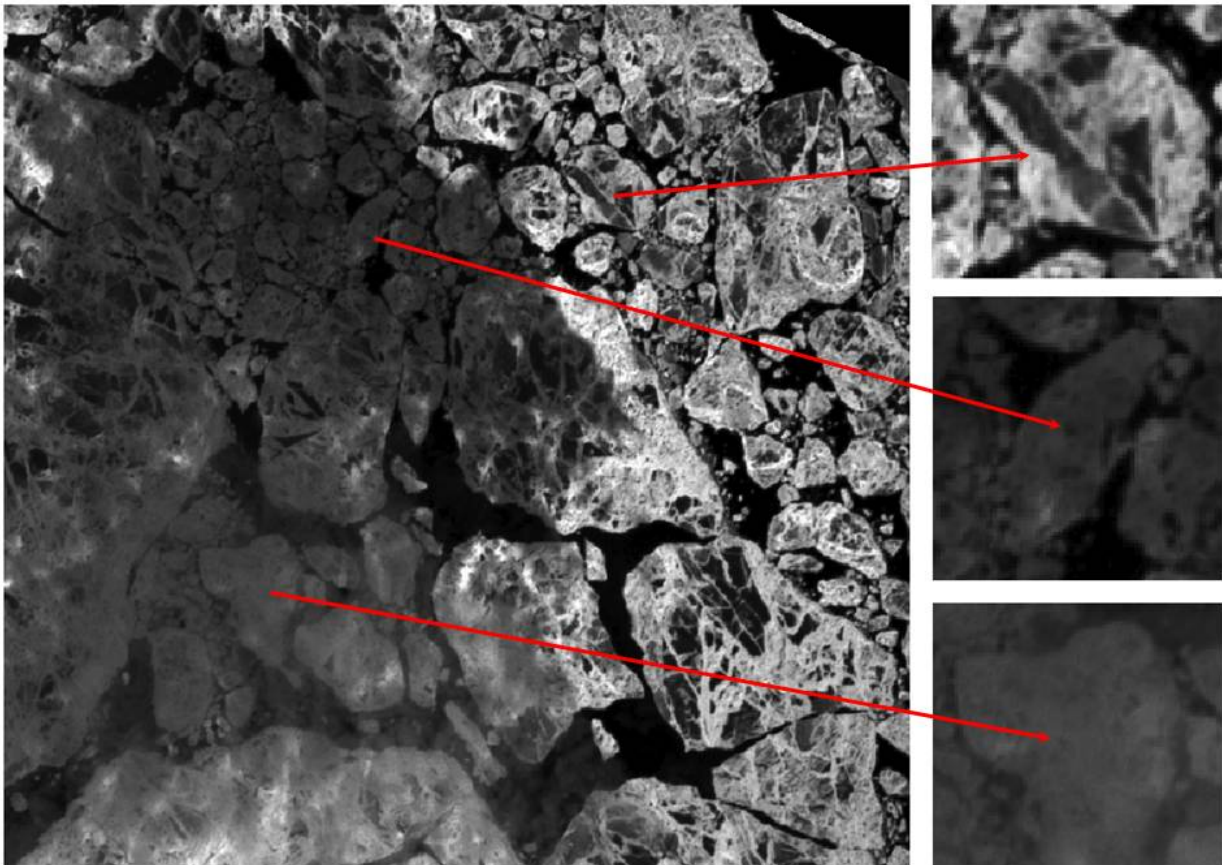


Figure 88. Sea ice features under cloud free (top right), cloud shadow (middle right) and cloud opacity (bottom right) conditions in Landsat-7 data

Figure 89 presents a typical example of missed ridge detection under cloudy conditions. Due to the cloud cover the sea ice ridge feature did not show up distinctly as an edge feature compared to the contrast between the open water and the sea ice. For this particular example the adaptive threshold did produce detection for the ridge but the Canny edge detection failed. Also of interest here is the production of three false alarms ridges caused by bright sea ice adjacent to dark SLC error regions. It is possible to develop an automate method to remove these false alarms based on their shared orientations being parallel with the SLC error bars. This is currently outside the scope of this work but it was thought that it should be noted.

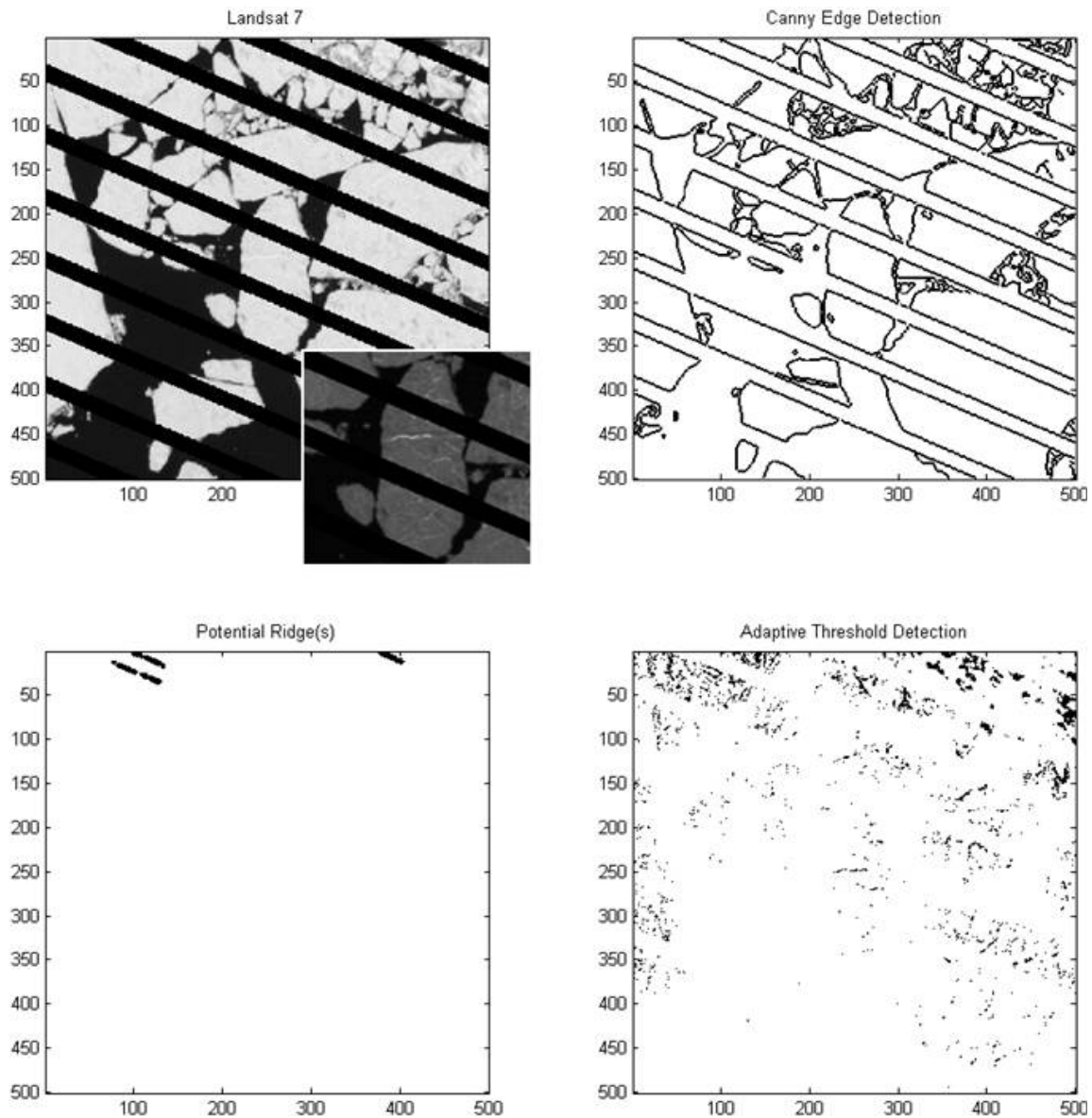


Figure 89. Ridge detection failure under cloud opacity, seasonal sea ice break up and SLC error conditions using Landsat-7

Of the 152 sea ice ridge features identified for this work, 13 we observed to contain some degrading effect from cloud shadow or opacity in the imagery. For the ridges identified under these conditions, 23% (3) were detected using the algorithm as presented here. Further analyses, including the number of false alarms, is recommended.

6.3.4 Ice Ridge Detection During Break-Up

The probability of sea ice ridge detection for Landsat-7 is limited during seasonal sea ice break up. This has been largely attributed to any surface snow being melted and the numerous sea ice fracture lines that are visually apparent during this time. Figure 90 shows a time lapse where a stationary ridge is quite discernible on May 17, 2011 but is considerably more difficult to identify one week later. Here the ridge features are still discernible however they are contained in an elaborate network of sea ice fracture lines making them difficult to visually or automatically decipher. Figure 91 presents an example of positive late season large ridge detection. Of the 152 sea ice ridge features identified for this work, 15 we observed during sea ice break up and interpreted to neighbor sea ice fracture lines which decrease detection and increase false alarm rates. For these ridges identified under these conditions, 67% (10) were detected using the algorithm as presented here.

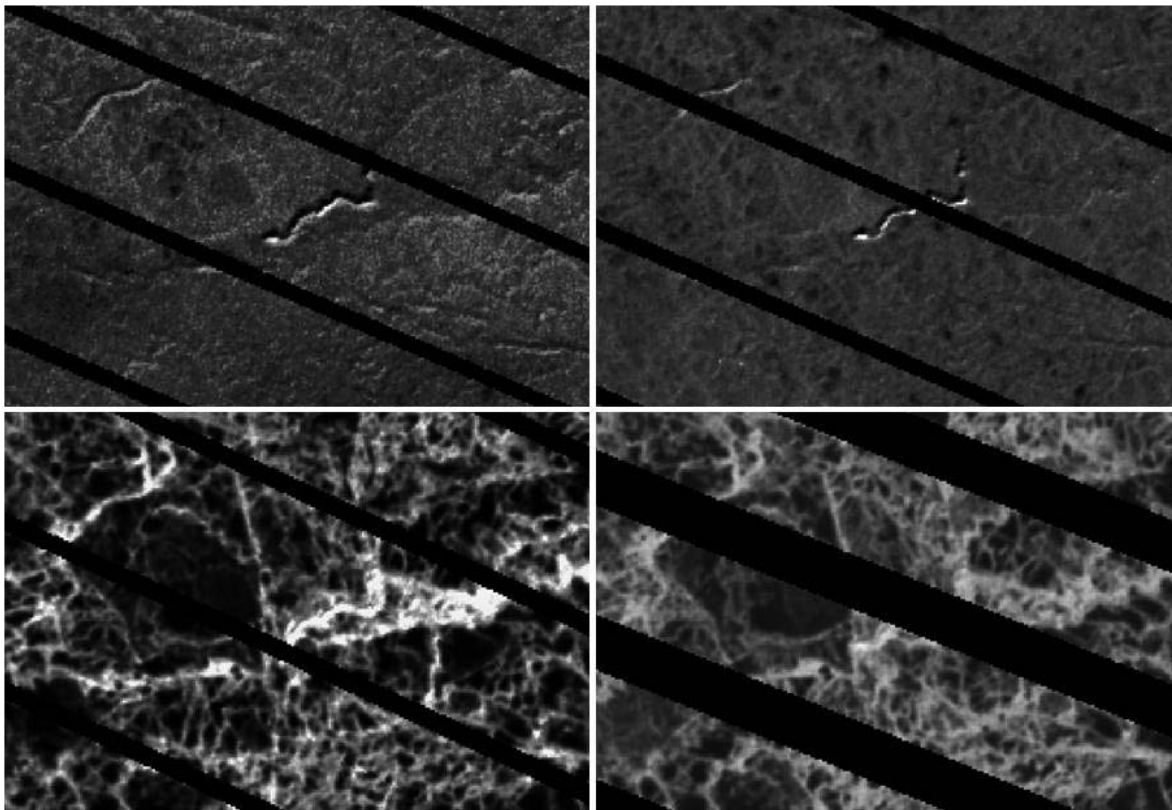


Figure 90. Stationary sea ice ridge in a flow adjacent to landfast sea ice in Landsat-7 2011, April 15 (top left), May 17 (top right), May 24 (bottom left) and May 26 (bottom right)

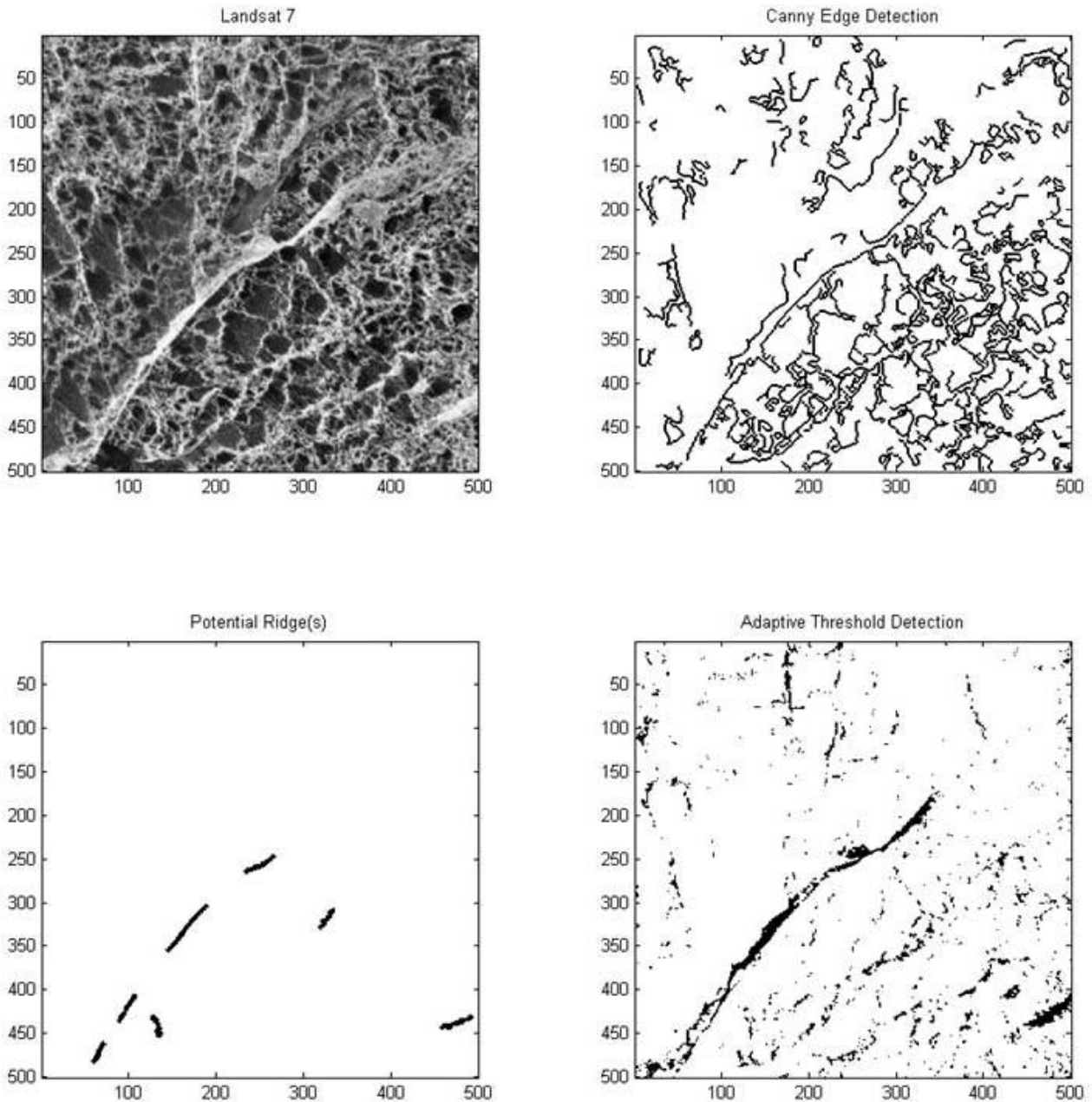


Figure 91. Ridge detection under sea ice break up conditions using Landsat-7

6.3.5 Results Summary

Sea ice ridges are readily identifiable in Landsat-7 imagery under ideal conditions. Though SLC error does truncate ridge features, interpretation of multiple ridge orientation makes identifying a unique ridge possible. Under ideal conditions, the detection rate observed for both the SLC free and SLC prone ridges was 80% or better. The presence of cloud opacity and cloud shadow produces a significant decrease in probability of ridge detection. Here, only a 23% detection rate was noted, as such optical imagery with cloud shadow or cloud opacity

regions are not deemed suitable for operational sea ice ridge detection. Seasonal break up also posed a problem for ridge detection with a 67% detection rate noted. The scarcity of snow and frequency of sea ice fracture lines makes ridge detection more difficult later in the season. The results presented here are based on visually identified ridges in the alandsat-7 imagery. In addition the limiting factors presented here, it is known that the ability to detect a ridge is dependent on the ridge sail height, length and resolution of the sensor. Should future work on ridge detection persist, a field program is recommended where ridge ground validation data be collected and monitored though the sea ice season coinciding with bi-weekly acquisition of high resolution optical and radar imagery.

7 CONCLUSIONS AND RECOMMENDATIONS

7.1 CONCLUSIONS

Correlation of ULS data and various satellite imagery platforms achieved limited success partly due to several factors. Availability of suitable imagery held in the various archives corresponding both spatially and temporally with ULS data collection provided limited options. The degree of confidence in ULS data correlation decreased with increased distance from ULS locations, especially in imagery acquired in late spring and early summer when break-up is underway. Attempting to correlate data with surface features in mixtures of loose floes and open water leads was difficult to perform with any degree of confidence. While surface features were evident in SAR imagery, they were not clearly identifiable compared to features in optical imagery.

A review of some available high resolution imagery, in particular optical Quickbird imagery, indicates that improvements with ULS correlation is possible. Unfortunately, neither the required ULS data is available, nor (for the most part) high-resolution satellite coverage over the ULS site.

7.2 RECOMMENDATIONS

The availability of high-resolution satellite data has increased significantly in the past few years, therefore a comparison when the more recent ULS data (2010 and later) when it becomes available could yield more favorable results. Ideally, high resolution satellite data should be ordered in advance to ensure that data is collected at regular intervals over the ULS site, rather than assuming that high-resolution imagery will be collected at the appropriate place and time. In the ULS data reviewed for this study, 70% of all keels with drafts over 20 m were detected in the period of May to July, therefore a data acquisition program could be implemented in 2012. Combining high-resolution satellite imagery, ULS (or several ULS installations) and a Lidar survey (or surveys) might give a more reasonable basis for comparison. Simultaneous acquisition of satellite based SAR and high resolution imagery would increase confidence in SAR feature identification.

8 REFERENCES

- Barker, A., R. De Abreu and G.W. Timco. (2008). Satellite detection and monitoring of sea ice rubble fields, 19th IAHR International Symposium on Ice, Vancouver, British Columbia, Canada, July 6-11, 2008.
- Canny, J. (1986). A Computational Approach to Edge Detection, *IEEE Transactions on Pattern Analysis and Machine Intelligence*, 8(6), 679-698.
- Canadian Ice Service website (2012). <http://ice-glaces.ec.gc.ca>.
- Dierking, W. and J. Askne. (1998). Polarimetric L- and C-band SAR signatures of Baltic sea ice observed during EMAC-95," in *Future Trends in Remote Sensing*, P. Gudmandsen, Ed. Balkema, Rotterdam, 1998, pp. 329–336
- Dierking, W. and J. Dall. (2007). Sea-ice deformation state from synthetic aperture radar imagery – Part 1: Comparison of C- and L-band and different polarization, *IEEE Transactions on Geoscience and Remote Sensing*, vol 45, no 11, pp 3610-3622.
- Hudier, E. and P. Larouche. (2005). A potential of polarimetric SAR data in mapping first years sea ice pressure ridges from the coherent and non-coherent components of HH and VV channels, *EARSel eProceedings*, pp 130-138.
- Johansson, R. (1989) Detection and characterization of ice ridges in the Baltic Sea using CV-580 imagery, *International Geoscience and Remote Sensing Symposium*, July 10-14 1989, pp 386-389.
- Johnston, M. (2001). Validation of RADARSAT imagery from in situ measurements from ridged first year ice, *POAC'01*, Ottawa, Canada, August 12-17, 2001, pp 1129-1138.
- Lewis, J.E., P. Budkewitsch, G. Newton, M. Sayed and R.M.W. Frederking. (1994). Two-dimensional analysis of ice ridging in the Beaufort Sea using aerial photography, *Annals of Glaciology*, vol 19, pp 25-32.
- Melling, H., Johnston, P.H. and Green, W.R. (1992). *IPS3: Ice Profiling Sonar Model 3*. Unpublished user manual. Institute of Ocean Sciences, P.O. Box 6000, Sidney, B.C. 52 pp + appendices.
- Marko, J.R., D.B. Fissel and K. Borg. (2003). Ice-type characterization in a marginal ice zone using RADARSAT and Ice-Profiling Sonar: Tools for structural design and navigation planning in ice infested waters, *POAC 2003*, June 16-19, 2003, Trondheim, Norway.
- Melling, H., D.R. Topham and D. Riedel. (1993) Topography of the upper and lower surface of deformed sea ice, *Cold Regions Science and Technology*, vol 21, pp 349-369.
- Melling, H., Riedel, D.A., (2004). "Draft and Movement of Pack Ice in the Beaufort Sea: A Time-Series Presentation April 1990 – August 1999". *Can. Tech. Rep. Hydrogr. Oc. Sci.* 238, v + 24 pp.

- Melling, H. (1998). Detection of features in first-year pack ice by synthetic aperture radar (SAR), *International Journal of Remote Sensing*, vol 19, no 6, pp 1223-1249.
- Melling, H., D.A. Riedel and Z. Gedalof (2005). "Trends in the Draft and Extent of Seasonal Pack Ice, Canadian Beaufort Sea", *Geophys. Res. Lett.*, 32, L24501, doi:10.1029/2005GLO24483.
- NSIDC (2011). Submarine Upward Looking Sonar Ice Draft Profile Data and Statistics. http://nsidc.org/data/docs/noaa/g01360_upward_looking_sonar/index.html
- Parker, J. (1997). *Algorithms for Image Processing and Computer Vision*, New York, John Wiley & Sons Inc.
- Pearson, D., C. E. Livingstone, R. K. Hawkins, A. L. Gray, L. D. Arsenault, T. L. Wilkenson, and K. Okamoto. (1980). Radar detection of sea-ice ridges and icebergs in frozen oceans at incidence angles from 0° to 90°, *Proc. 6th Can. Symp. Remote Sens.*, Halifax, NS, Canada, 1980, pp. 231–237
- Timco, G.W., Croasdale, K. and Wright, B. (2000). An Overview of First-Year Sea Ice Ridges. PERD/CHC Report 5-112, August.

LAST PAGE OF DOCUMENT